Microscopic Optical Trapping of Ultracold Neutral Atoms for Applications in Quantum Information

Thesis

Microscopic Optical Trapping of Ultracold Neutral Atoms for Applications in Quantum Information

Michael Copley-May

A thesis submitted in partial fulfilment of
the requirements for the degree of Doctor of Philosophy

December 2018

School of Physical Sciences
Faculty of Science, Technology, Engineering and Mathematics

Supervisors: Dr. Silvia Bergamini
Dr. Jimena Gorfinkiel

Abstract

In this thesis, the development of an experimental system for microscopic dipole trapping of ultracold neutral rubidium atoms is presented. The purpose of this system is to advance towards the experimental realisation of a quantum computational protocol utilising neutral atoms as qubits. It is intended that the quantum gate operations between qubits will be implemented by a scheme using Rydberg blockade, imposing a restriction on the maximum size of the dipole-trapped atom cloud; the spatial extent of the atomic ensemble contained in this trap must be smaller than the blockade radius to ensure that one single collective Rydberg state per qubit can be achieved. Therefore the experiment was designed with the intent of fulfilling these challenging requirements.

This project involved the design and construction of an improved ultra-high vacuum chamber containing the optical setup for the experiment, successfully achieving pressures below 5×10^{-10} mbar. A magneto-optical trap was produced to act as a background reservoir of atoms from which to load the dipole trap. Numerous experimental measurements were done to characterise the physical properties of the trapped atoms, including the number, density and temperature of atoms, as well as the lifetime of the trap. The results of these measurements led to the conclusion that a suitable reservoir for loading the dipole trap had been produced.

Significant work was carried out to set up and obtain the dipole trap in the laboratory. Measurements of the characteristic properties of the trap and the atoms confined in the trap were carried out to investigate the behaviour of the atoms and to validate our design. Ultimately a trap containing tens of atoms was achieved, with an atom cloud diameter of ~ 1.2 μm in two dimensions, being well within the estimated Rydberg blockade radius of ~ 4.4 μm for $n \sim 60$ as intended.

The two-photon excitation laser system for the probing of Rydberg states, for future applications in Rydberg blockade-based quantum gate operations, was also developed during the course of this work. Different Rydberg states were detected experimentally by the observation of Autler-Townes splitting in a three-level atom scheme.

Overall, the work presented in this thesis provides a strong groundwork for the advancement towards neutral atom-based quantum gates, including the development of the experimental system and the production of standard procedures to carry out characterisation measurements of the traps efficiently in the future. The main achievements of this work are the establishment of the experimental apparatus, the achievement of a microscopic dipole trap which conforms to the requirements of an atomic qubit, and the significant growth in the knowledge of atom trapping specific to our system.

Acknowledgements

I would like to thank my supervisor, Dr. Silvia Bergamini, for allowing me the opportunity to work on this PhD project, throughout the course of which I have learnt so much. I would also like to thank Dr. Calum MacCormick, who has been a constant source of invaluable guidance, knowledge and help. I would like to thank my fellow PhD student Katarzyna Krzyzanowska who patiently taught me the ins and outs of the lab, and provided much help throughout my PhD; thanks also to Dr. Rudy Romain for his help during his post-doctoral position in our group. I am grateful for the efforts of Chris Hall and the engineering workshop, who helped to design and build some of our experimental components. Thank you to my parents for their unending support. Last but not least, I would like to give my most heartfelt thanks to my wonderful girlfriend Mona for being there for me every second of the journey.

Contents

Contents v

List of Figures ix

1 Introduction 1

2 Background Theory of Quantum Computing 9

2.1 Qubits . . . 10

2.2 Quantum Gates . . . 13

2.3 DQC1 . . . 16

2.4 Implementation of Quantum Computing . . . 19

2.4.1 The DiVincenzo criteria . . . 19

2.4.2 Platforms for the practical implementation of quantum computing . . . 21

2.4.3 Cold atoms as qubits . . . 23

2.4.4 Rydberg interactions for logic gates . . . 27

2.4.5 Electromagnetically induced transparency . . . 32

2.4.6 A quantum logic gate using Rydberg atoms . . . 35

2.5 Summary . . . 41

3 Cooling and Trapping Atoms 43

3.1 Atom-Light Interaction . . . 44

3.2 Laser Cooling and Trapping . . . 53

3.2.1 Doppler cooling . . . 53
3.2.2 Zeeman degeneracy and optical pumping . . . 58
3.2.3 Magneto-optical trap . . . 58
3.2.4 Sub-Doppler cooling . . . 60
3.3 Dipole Trapping . . . 63
3.4 Summary . . . 66

4 Implementation of Atom Trapping 69
4.1 Cooling and Repump Laser System . . . 70
4.1.1 Laser sources and transitions . . . 71
4.1.2 Frequency locking . . . 73
4.2 Vacuum System . . . 78
4.2.1 Troubleshooting the vacuum chamber . . . 82
4.2.2 Redesign and rebuilding the vacuum chamber . . . 89
4.3 Magneto-Optical Trap . . . 96
4.3.1 Characterisation of the MOT . . . 98
4.4 Summary . . . 116

5 Implementation of a Microscopic Dipole Trap 119
5.1 Dipole Trap Laser and Imaging System . . . 120
5.1.1 High-NA lenses . . . 122
5.1.2 Shape correction . . . 123
5.1.3 Collimation . . . 126
5.1.4 Imaging system . . . 128
5.1.5 ICCD camera focus . . . 131
5.1.6 ICCD trigger timing . . . 134
5.2 Characterisation of the Dipole Trap . . . 137
5.2.1 Size . . . 138
5.2.2 Atom number and Stark shift . . . 145
5.2.3 Temperature . . . 151
5.2.4 Lifetime . . . 157

5.3 Summary 173

6 Rydberg States for Long Range Interactions **177**

6.1 Two-photon excitation laser system 178

6.1.1 Frequency locking by modulation transfer spectroscopy . . 179

6.1.2 Measurement of wavelength 184

6.1.3 Investigation of the EIT feature and calculation of the Rydberg blockade radius 186

6.2 Summary 191

7 Conclusions and Outlook **193**

Appendices **200**

A Sources of noise on the ICCD camera **201**

Bibliography **207**

List of Figures

2.1 Bloch sphere representation of a qubit state 13
2.2 Example of a quantum circuit 15
2.3 Quantum circuit of the DQC1 model 17
2.4 Atomic energy level structure of rubidium 25
2.5 Rydberg blockade diagram 29
2.6 Quantum phase gate using Rydberg blockade 31
2.7 Three-level electromagnetically induced transparency (EIT) scheme 33
2.8 Four-level EIT scheme with Raman beams 36
2.9 Quantum gate to perform DQC1 using EIT and Rydberg blockade 38
2.10 Experimental arrangement of dipole traps containing the control and ensemble qubits 39

3.1 Light shifted energy level diagram 53
3.2 Doppler cooling process 55
3.3 Magneto-optical trap (MOT) diagram 56
3.4 Zeeman splitting energy level diagram 59
3.5 Sisyphus cooling diagram 61
3.6 Dipole trap diagram 66

4.1 Cooling and repump transitions with respect to the energy level structure of rubidium 72
4.2 MOT laser system diagram 74
4.3 Saturated absorption spectrum of rubidium 76
4.4 Photograph of the main body of the original vacuum chamber . . 83
4.5 Infrared camera image of the MOT 84
4.6 Measured loading curves and $N_{eq} - \tau$ plot for the MOT 86
4.7 Vacuum chamber leak detection results and viewport damage . . 89
4.8 Comparison between old and new vacuum chamber designs 91
4.9 Vacuum chamber temperature and pressure during baking 95
4.10 MOT laser system diagram part 2 99
4.11 MOT loading curve for measurement of atom number 102
4.12 2D Gaussian fit to MOT image 103
4.13 MOT release-recapture experiment sequence for temperature measurement 106
4.14 Voltage trace for a single release-recapture process 107
4.15 Release and Recapture measurement for MOT temperature 109
4.16 MOT TOF experiment sequence for temperature measurement . . 112
4.17 Time of flight measurement for MOT temperature 115

5.1 Experimental setup for dipole trap imaging 121
5.2 Custom lens mount for dipole trap 123
5.3 Diagram of shape-correcting prisms 124
5.4 Dipole trap laser beam shape correction 124
5.5 Dipole trap beam collimation setup 127
5.6 Diagram of dipole trap beam and atom cloud size 132

5.7 Dipole trap camera focus position measurement 133
5.8 ICCD trigger timing measurement 136
5.9 Dipole trap profile 140
5.10 Dipole trap Stark shift experiment sequence 148
5.11 Dipole trap atom number and light shift measurement 150
5.12 Dipole trap time-of-flight experiment sequence 153
5.13 Time of flight dipole trap temperature measurement 156
5.14 Dipole trap lifetime experiment sequence 160
5.15 Dipole trap lifetime measurement 162
5.16 Dipole trap lifetime measurement in a larger trap 167
5.17 Dipole trap lifetime measurement data and fit using larger trap . 168

6.1 Experimental setup for the two-photon excitation system 180
6.2 Scan of the modulation transfer spectroscopy (MTS) locking system error signal 182
6.3 Two-photon transition absorption spectrum 183
6.4 Comparison of measured Rydberg level frequencies with literature 186
6.5 Fitting and analysis of measured Autler-Townes transparency peak 187

A.1 ICCD dark and readout noise analysis 204

Chapter 1

Introduction

The computational power of silicon chip-based computers has advanced dramatically over the last few decades. As the number of transistors on a chip increases, there is a need for them to be made increasingly smaller, and if computing power continues evolving at the current rate the required size for these transistors will rapidly approach the atomic level, at which quantum mechanical behaviour becomes dominant. This places a hard limit on the feature size achievable by classical computers, which in turn limits the achievable power.

In order to overcome the limitations of classical computation, attention has turned to the prospect of utilising quantum behaviour for enhanced computational speed. It has been shown that certain 'hard' problems for which there is no efficient classical algorithm for solving, such as finding the prime factors of large integers and finding discrete logarithms, can be processed far more efficiently using quantum algorithms such as Shor's algorithm [1]. In this example, the time taken for the fastest known classical algorithm for prime factorisation

scales exponentially with the number of digits to be factorised, whereas Shor's algorithm can perform the calculation in polynomial time, giving an exponential speedup over the classical case. Another example of an algorithm which can utilise quantum mechanics for enhanced efficiency is Grover's search algorithm [2]. Such algorithms have significant applications in information processing and cyber security, in which they form the basis of secure data transmission, as well as in the simulation of quantum systems.

A classical computer fundamentally stores information in the form of bits, which is a logical value of either '0' or '1'. This information is processed by logic gates, such as the NOT gate, which swaps the value of a single bit. In contrast, a quantum computer would store and process information using quantum bits, or 'qubits'. These qubits, similar to bits, have two states, '0' and '1', but following the laws of quantum mechanics they can also exist in a superposition of these two states, until measured[1]. This property, along with the presence of non-classical correlations known as entanglement and discord [3], give rise to the enhanced computational power of quantum systems.

In the race to implement a stable and reliable quantum computational system in the laboratory, a number of potential platforms for quantum computing are currently undergoing research, each with their own physical realisation of the qubit. These include trapped ions, NMR (nuclear magnetic resonance), photons, superconducting circuits, and solid-state qubits, as well as ultracold neutral atoms, which are the subject of the work presented in this thesis. As outlined by DiVincenzo in 2000 [4], a properly functioning quantum computer should fulfil

[1]Measurement of a system described by a quantum-mechanical wavefunction causes the collapse of the wavefunction and the state of the system falls into an eigenstate.

several criteria: scalability to a larger system, a universal set of quantum logic gates, long coherence times, the ability to initialise the system into a certain state, and the ability to read out the final state of the system. Each proposed platform has its own advantages and disadvantages, and the difficulty in fulfilling more than one or two of the criteria within a single system makes it extremely challenging to implement quantum computation. An advantage to using neutral atoms as qubits is the high degree of control over them that can be achieved using lasers, as a laser system can be used to slow, trap, move, and control the state of the atoms, as well as inducing interactions between the qubits.

Although there are still significant challenges to overcome before full quantum computation is realisable in the laboratory in a form with useful commercial and technological applications, there has been rapid advancement in recent research. Entanglement was first demonstrated between neutral atoms in Rydberg states by photon exchange in 1997 [5]. More recently, entanglement has been shown by the Rydberg blockade effect in 2010 [6], which has been used to experimentally demonstrate a controlled-NOT (CNOT) logic gate [7]. Entanglement fidelities achieved in these experiments after atom-loss correction were 0.75 and 0.73 respectively[2]. In 2015, the spins of trapped caesium atoms were entangled with a post-correction fidelity of ≥ 0.81 [9] and entanglement fidelity by Rydberg blockade had improved to 0.79 [10]. Blockade-based entanglement has also been shown using multi-atom ensemble qubits [11,12]. Achieving high (~ 1) two-qubit gate fidelities remains an outstanding problem for the implementation of atomic

[2]The fidelity of a quantum gate is a measure of how close the resulting state is to the intended target state [8], with a fidelity of 1 being exactly equal to the target state and 0 being as different as physically possible. Environmental factors such as decoherence act to lower fidelity.

qubits. Progress has also been made in the preparation of arrays of atomic qubits; in 2014 a 2D array of traps with arbitrary geometries was demonstrated [13], and in 2015 a 2D 49-qubit array was loaded with an average of 29 single atomic qubits with average single-qubit gate fidelities of > 0.99 [14]. Since then, 3D qubit arrays with individually targeted sites have also been produced using optical lattices [15]. Deterministic single-atom loading using optical tweezers was demonstrated in 2016 to produce defect-free arrays of over 50 atomic qubits [16, 17]. Long coherence times in the range of seconds have been achieved for neutral atoms [18].

Research into the experimental implementation of quantum computation utilising physical platforms other than neutral atoms has also seen substantial progress. The quantum CNOT gate has recently been demonstrated using polarisation-encoded photonic qubits, with fidelities of around 0.76 [19]. The blueprint for the design of a constructable quantum computer based on trapped ions has even been unveiled [20]. The field of quantum computing has drawn interest from large companies in industry such as Google, Microsoft, IBM and Intel, who have claimed to have produced solid-state and superconducting-based quantum processors comprising 49 or more qubits in recent months [21–23].

It is possible to facilitate the application of a neutral atomic platform for quantum computing by settling for a system which does not qualify as a fully universal quantum computer, but can still utilise non-classical correlations to provide speedup over classical algorithms for specific tasks, while relaxing the requirements for coherence and scalability. The quantum algorithm which can be implemented by this system is known as deterministic quantum computation with one qubit, or DQC1. First proposed by Knill and Laflamme [24], DQC1

provides an estimate of the normalised trace of an arbitrary unitary matrix. This model proves easier to implement than full quantum computation with pure states and entanglement, as no complete entanglement exists between the qubits in the system and only a single qubit is required to be in a pure state. In fact, only a small fraction of purity is required in the qubit [25]. DQC1 has since been demonstrated in photonic and NMR-based systems [26–28] but these systems still suffer from poor scalability, allowing the trace of only trivial unitaries to be calculated. It is expected that implementing the DQC1 model with an atomic system containing sizeable ensembles of hundreds of atoms can overcome this weakness in scalability and allow the algorithm to be applied to the calculation of the trace of non-trivial unitaries [29]. A successfully implemented DQC1 protocol would have applications in areas such as quantum metrology [30] and knot theory, where it could be used for estimating the Jones polynomial [31].

The work presented in this thesis is motivated by the potential applications of quantum information processing using neutral atoms as a physical platform. The aim of this research is to study and implement the practical realisation of some of the building blocks of quantum computing using cold rubidium atoms. The manipulation of atoms for applications in quantum information requires a complex experimental set up and procedure. The main body of work concerns this experimental set up, including the design and construction of an ultra high vacuum chamber, and laser system for the cooling and trapping of atoms in a magneto-optical trap and microscopic dipole trap. Experiments were performed to measure the characteristic properties of the trapped atoms, and the development of a two-photon excitation system capable of probing Rydberg

states is also presented. The key achievements of the work in this thesis are the successful production of a microscopic dipole trap containing small numbers of atoms and the development of measurement techniques for the characterisation of physical parameters such as the number of atoms, temperature, lifetime and size of the trapped atom cloud. The trap partially adheres to the physical requirements for an atomic qubit capable of long-range interaction with other qubits by Rydberg blockade, with the final trap size being well within the calculated Rydberg blockade radius in two dimensions.

The originality of this work stems from the overarching goal of implementing DQC1 with neutral atoms which has not been done before as of the time of writing. This requires an original and unique experimental setup to produce atom traps designed specifically for the intended application, allowing one single-atom qubit and one ensemble qubit to be contained in microscopic traps within the Rydberg blockade radius for the desired long-range interactions to occur. While the blockade interaction has been demonstrated between microscopic dipole-trapped atoms to perform gate operations [10], this is still a novel technology which the future work in our laboratory will substantiate and contribute knowledge to. To the author's knowledge this field has not yet been explored experimentally using the combination of single-atom and ensemble qubits which our experiment is aimed towards. My personal contribution has been to develop the groundwork of this novel implementation, by designing and building an experimental system which conforms to our own unique requirements. This includes achieving microscopic dipole trapping with the potential to extend the system to two traps in close proximity in the future, developing a two-photon

excitation system to access Rydberg states and EIT as required by the quantum logic gate we intend to implement, and creating a library of standard experimental procedures for fast and efficient measurement of the trap and atom properties. Due to the early stage at which the project was started, my contribution also includes the redesign and construction of most of the experimental apparatus, including the ultra-high vacuum chamber and laser systems.

In chapter 2, the fundamental principles underlying the theory of quantum computing and its implementation with neutral atoms are introduced, giving insight into the source of enhanced computational efficiency which motivates research in this field. In chapter 3, further details of the experimental implementation with atoms are given, including the theory of atom-light interaction and the powerful atom-trapping and manipulation techniques which can be achieved using lasers. In chapter 4, the experimental set up for the research presented in this work is explained. This includes the laser system used for atom trapping, and the ultra-high vacuum chamber in which the trap is housed in order to prevent collisional losses. This chapter also includes experimental work done to produce and characterise the properties of the magneto-optical trap (MOT), which comprises the first stage of trapping, obtaining a reservoir of cold atoms to supply the dipole trap. In chapter 5, the work done towards the set up of a microscopic optical dipole trap is presented, including experimental measurements and discussion of the trap characteristics. In chapter 6, the set up of a two-photon excitation system used to probe highly excited Rydberg states is introduced, along with measurements of the frequencies of the detected states. The development of this excitation system is motivated by enabling

Rydberg-blockade based interactions within the microscopic trap presented in previous chapters. Finally in chapter 7, the conclusions and findings of the work are summarised, with a final overview of the research presented in this thesis.

Chapter 2

Background Theory of Quantum Computing

In the field of atomic physics, significant attention has turned to the potential for the practical implementation of a quantum computer. It has been shown theoretically that quantum computational systems have the capability to process certain algorithms with exponentially greater efficiency than their best classical counterpart. This has motivated research in many areas of experimental physics to overcome the significant challenges of the experimental implementation of quantum information processing. Neutral atoms represent a strong candidate to provide the basis of such an implementation, using well-developed laser techniques.

In this chapter, the fundamental components which form the foundation of a quantum computer and give rise to its enhanced computational efficiency will be described. This includes the quantum bit of information, or qubit, as well

as quantum logic gates. A quantum computational algorithm known as DQC1 (deterministic quantum computation with 1 qubit) for the calculation of the trace of a unitary matrix will be presented as an example of a protocol which may potentially be implemented experimentally. An introduction to the application of quantum computational processes such as this using neutral atoms as qubits will then be given, the experimental realisation of which forms the main body of work in this thesis.

2.1 Qubits

The base requirement for quantum computation is a register of quantum bits, also known as qubits. A qubit can be encoded in any two-state quantum system, such as a spin-1/2 particle or two-level atom. The two qubit basis states will be denoted as $|0\rangle$ and $|1\rangle$, and form the two-dimensional computational basis in Hilbert space, with vector representations

$$|0\rangle \equiv \begin{pmatrix} 1 \\ 0 \end{pmatrix} \qquad |1\rangle \equiv \begin{pmatrix} 0 \\ 1 \end{pmatrix}. \tag{2.1}$$

The general qubit state can then be written as a superposition of these two states, given by

$$|\psi\rangle = a\,|0\rangle + b\,|1\rangle \tag{2.2}$$

where a and b are complex amplitudes satisfying $|a|^2 + |b|^2 = 1$. Therefore the norm of the total qubit state $\sqrt{\langle\psi|\psi\rangle} = 1$.

A system containing multiple qubits may be described by a single state, known as a many-qubit state. It is useful to describe a system by a many-qubit state if the qubits cannot be individually measured experimentally, or if the system contains entanglement which means the total state of the system cannot be separated into a product of single qubit states. The state of N unentangled qubits can be written as the tensor product of the individual qubit states,

$$|\Psi_{ABC\cdots}\rangle \;=\; |\psi_A\rangle \;\otimes\; |\psi_B\rangle \;\otimes\; |\psi_C\rangle \;\otimes\; \cdots\,, \tag{2.3}$$

and exists in the Hilbert space

$$\mathcal{H}_{ABC\cdots} \;=\; \mathcal{H}_A \;\otimes\; \mathcal{H}_B \;\otimes\; \mathcal{H}_C \;\otimes\; \cdots\,. \tag{2.4}$$

This product state has $2N$ complex coefficients. In contrast, the most general N-qubit state, which may be a product state or entangled state, is given by

$$|\Psi_N\rangle \;=\; c_0\,|0\cdots00\rangle \;+\; c_1\,|0\cdots01\rangle \;+\; c_2\,|0\cdots10\rangle \;+\; \cdots \;+\; c_{2^N}\,|1\cdots11\rangle\,. \tag{2.5}$$

This state has 2^N complex coefficients, allowing far more information to be stored and processed for large N than for a product state. This demonstrates the importance of non-classical correlations such as entanglement for computing power. Notably, a system of N classical bits may store one out of 2^N possible values, whereas the general many-qubit state stores information about all 2^N possible values simultaneously in the form of a superposition, which is the source of the potential computational speedup provided by quantum mechanical systems

over classical ones.

A qubit state is referred to as a 'pure' state if it can be expressed by a single state vector, $|\psi\rangle$, with a probability of 1 of existing in this state. A more general kind of qubit state is a 'mixed' state, which is a statistical mixture of pure states. In a realistic scenario, interactions with the environment cause decoherence of pure states, causing them to decay into mixed states.

The density operator of a state $|\psi\rangle$ is given by the outer product of the state with itself, $\hat{\rho} = |\psi\rangle \langle\psi|$. More generally, the density operator of a mixed state, being a statistical mixture of n pure states $|\psi_n\rangle$, is $\hat{\rho} = \sum_n p_n |\psi_n\rangle \langle\psi_n|$. This provides a useful representation of multi-qubit states, as the diagonal elements of $\hat{\rho}$ in matrix form correspond to the normalised populations of each eigenstate, whereas non-zero off-diagonal elements (known as 'coherences') indicate the presence of non-classical correlations between the single qubits.

The concept of qubit states can be more easily visualised by using a useful representation known as the Bloch sphere, shown in Figure 2.1. Here, the two qubit basis states $|0\rangle$ and $|1\rangle$ are placed at the north and south poles of the sphere. Any possible pure state of a single qubit can be represented by a point on the surface of the sphere, and a mixed state can be represented by a point inside the sphere. Each pair of diametrically opposite points on the surface correspond to mutually orthogonal state vectors. Points on the equator of the sphere in the $z = 0$ plane represent states in an equal superposition of the two qubit basis states. Using this representation, the evolution of the state of a qubit subjected to a unitary operation by a quantum gate can be visualised as a rotation of the state across the surface of the sphere.

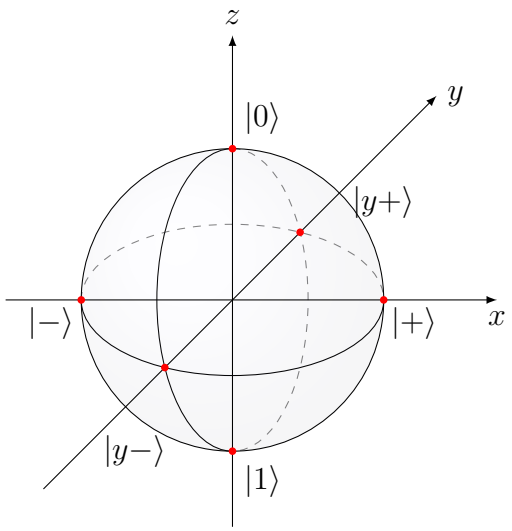

$$|+\rangle = (|0\rangle + |1\rangle)/\sqrt{2}$$

$$|-\rangle = (|0\rangle - |1\rangle)/\sqrt{2}$$

$$|y+\rangle = (|0\rangle + \mathrm{i}\,|1\rangle)/\sqrt{2}$$

$$|y-\rangle = (|0\rangle - \mathrm{i}\,|1\rangle)/\sqrt{2}$$

Figure 2.1: The Bloch sphere representation of a single qubit pure state. Any state can be represented as a superposition of the computational basis states $|0\rangle$ and $|1\rangle$, corresponding to a point on the surface of the sphere. The effect of a quantum gate on the qubit state can be visualised as a rotation of the state across the surface of the sphere.

2.2 Quantum Gates

In order to perform computation, logic gates are required to process the information stored by bits. In classical computing, a gate takes one or more input values of 0 or 1 and produces an output value of 0 or 1 which depends on the input. The quantum analogue of this gate is an interaction involving one or more qubits which can modify the states of these qubits, including the ability to prepare them in superposition states. In this way, an equal number of output values in the form of complex state coefficients are produced at the end as there are input values. A quantum gate can be represented by a unitary matrix which acts on a single-qubit or many-qubit state vector by matrix multiplication to produce the output state vector. In the case of a single pure state, this corresponds to a rotation of the state over the surface of the Bloch sphere.

Two important examples of quantum gates are the Hadamard gate, which is a single-qubit gate, and the controlled-NOT or CNOT gate which is a two-qubit gate. The Hadamard gate is represented by the matrix

$$U_{\mathrm{H}} = \frac{1}{\sqrt{2}} \begin{pmatrix} 1 & 1 \\ 1 & -1 \end{pmatrix} \tag{2.6}$$

and causes a qubit in either state $|0\rangle$ or $|1\rangle$ to be prepared in a 50/50 superposition of these two states. This is useful as the easiest way to initialise a qubit at the beginning of computation is to prepare it in either the $|0\rangle$ or $|1\rangle$ state, and a uniform superposition of these is often desirable for speedup over classical algorithms. For example, initial preparation into uniform superposition states using Hadamard operations is a vital step in both the Shor and Grover algorithms [1, 2].

The CNOT gate is represented by the matrix

$$U_{\mathrm{CNOT}} = \begin{pmatrix} 1 & 0 & 0 & 0 \\ 0 & 1 & 0 & 0 \\ 0 & 0 & 0 & 1 \\ 0 & 0 & 1 & 0 \end{pmatrix}. \tag{2.7}$$

The truth table for the CNOT gate is displayed in Table 2.1. The two qubits involved in the gate operation are known as the control and target qubits. As can be seen from the table, the state of the target is swapped between the two qubit states only when the control qubit is in the $|1\rangle$ state. The CNOT gate together with the Hadamard gate form a universal set of quantum logic gates, which means

In		Out	
C	T	C	T
0	0	0	0
0	1	0	1
1	0	1	1
1	1	1	0

Table 2.1: Truth table for the two-qubit CNOT gate, showing the input and output state values of the control (C) and target (T) qubits.

that it is possible to form a system of only CNOT and Hadamard gates which is capable of arbitrary computation. In other words, any unitary operation can be performed by some sequence involving only these gates. In general, any set of gates capable of applying an arbitrary unitary operation on a series of qubits is capable of forming a universal set. This is achievable using single-qubit and CNOT gates [8].

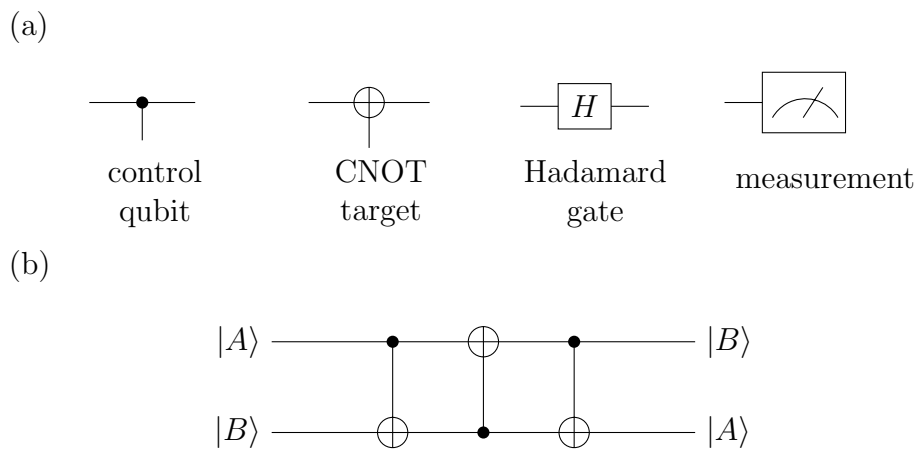

Figure 2.2: Example of a quantum circuit diagram. Some useful circuit elements are shown in (a). Here, the control and target elements represent the control and target qubits involved in the 2-qubit CNOT gate. An example circuit is given in (b), showing two initial qubit states at the far left, undergoing CNOT gates while alternating the roles of the control and target qubits, resulting in the output states at the far right. This circuit represents the SWAP gate, which swaps the two initial qubit states. This figure demonstrates the reversibility of quantum gates.

A quantum computational model describing a process involving qubits and gates is commonly represented by what is known as a 'quantum circuit'. Some of the important circuit elements used in this representation are shown in Figure 2.2 (a). An example of a quantum circuit is displayed in Figure 2.2 (b), showing a two-qubit system undergoing a series of CNOT gates. The result of this circuit is an operation known as the SWAP gate, which swaps the states of these two qubits. This operation works as follows: first a CNOT gate is applied to the two qubit system, switching the state of the target if the control is in $|1\rangle$. Following this an inverted CNOT gate is applied, in which the roles of control and target are reversed; this causes the control qubit to switch state if the target is in $|1\rangle$. The result of these first two CNOT gates is that the control qubit is set to the initial state of the target qubit. Following this, there is a final CNOT gate causing the target to switch states if the control is now in $|1\rangle$, which causes the target state to be set to the initial state of the control qubit, completing the swap process. Although the initial input qubit states may be superpositions of these basis states rather than exactly $|0\rangle$ or $|1\rangle$, the fact that any quantum state can be described by a linear combination of these basis states allows the swap operation to function properly for any input.

2.3 DQC1

Deterministic Quantum Computation with 1 qubit, or DQC1, is a computational model capable of providing speedup over the most efficient classical algorithm for the calculation of the trace of an arbitrary unitary matrix [24]. This model

utilises non-classical correlations known as discord.

Formally, within a system containing both classical and quantum correlations, the term discord indicates the proportion of correlations which are quantum-mechanical in nature as opposed to classical. In other words, it can be used as a measure of the 'quantumness' of correlations within a system [32]. These non-classical correlations include, but are not limited to, entanglement. Historically quantum entanglement, which requires the purity of the system to be maintained, was recognised as the key resource for quantum computation and the source of speedup over classical computers. However, the non-classical correlations present in the DQC1 model have been characterised using discord [3] and it has been shown that entanglement is not present within the system, suggesting that discord is the computational resource used by this model.

DQC1 can be represented by the quantum circuit shown in Figure 2.3. Initially,

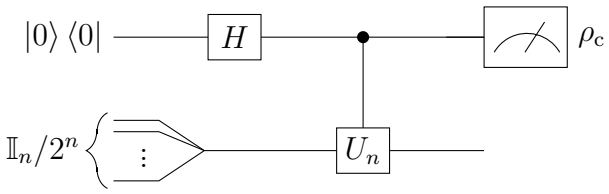

Figure 2.3: Quantum circuit diagram of the DQC1 model of quantum computation. The system begins with a pair of spatially separated qubits, a single control qubit in the $|0\rangle\langle 0|$ state and an ensemble in the maximally mixed state $\mathbb{I}_n/2^n$. The control qubit undergoes a Hadamard gate, then acts as the control for a unitary operation on the ensemble represented by U_n, before being measured at the end of the process.

the system consists of one pure qubit, and an ensemble of n qubits in a random mixed state. In fact, the pure qubit does not necessarily have to be in a completely pure state, it merely needs to contain some small amount of purity [25]. Therefore it will be referred to as the control qubit in this section for convenience. The

control qubit is prepared in the state $|0\rangle$, so it is represented by the density operator

$$\rho_c \;=\; |0\rangle\langle 0| \;\equiv\; \begin{pmatrix} 1 & 0 \\ 0 & 0 \end{pmatrix}. \tag{2.8}$$

The n ensemble qubits are prepared in the maximally mixed state $\mathbb{I}_n/2^n$, where $\mathbb{I}_n$ is the identity matrix for n qubits, with dimension 2^n. The control qubit and ensemble are initially independent, so the total state of the system in density operator representation is given by the product state

$$\rho \;=\; |0\rangle\langle 0| \;\otimes\; \mathbb{I}_n/2^n \;=\; \frac{1}{2^n}\begin{pmatrix} \mathbb{I}_n & 0_n \\ 0_n & 0_n \end{pmatrix}. \tag{2.9}$$

The first operation in the circuit is the action of a Hadamard gate on the control qubit. This prepares the qubit in the state $1/\sqrt{2}\begin{pmatrix} 1 \\ 1 \end{pmatrix}$. The second operation is a controlled unitary operation U_n. This leaves the total system in the state

$$\rho \;=\; \frac{1}{2^{n+1}}\begin{pmatrix} \mathbb{I}_n & U_n^\dagger \\ U_n & \mathbb{I}_n \end{pmatrix}. \tag{2.10}$$

After this operation, a measurement is performed on the control qubit. The state of the ensemble is not detected, so the measured state is given by the reduced density operator of the control qubit [29],

$$\rho_c \;=\; \frac{1}{2}\begin{pmatrix} 1 & \frac{\mathrm{Tr}[U_n^\dagger]}{2^n} \\ \frac{\mathrm{Tr}[U_n]}{2^n} & 1 \end{pmatrix}. \tag{2.11}$$

We see from this equation that the control qubit remains in a superposition of the $|0\rangle$ and $|1\rangle$ states, but the trace of the unitary matrix is encoded within the coherences of the qubit. Measurements of the expectation values of the Pauli X and Y spin operators can be used to extract the real and imaginary parts of this trace respectively, as

$$\langle X \rangle = \mathrm{Re}\left[\mathrm{Tr}\left(U_n\right)\right]/2^n, \tag{2.12}$$

$$\langle Y \rangle = -\mathrm{Im}\left[\mathrm{Tr}\left(U_n\right)\right]/2^n. \tag{2.13}$$

The measurement process can be performed by measuring the populations of the $|0\rangle$ and $|1\rangle$ states after an X or Y rotation. The measurements must be repeated many times in order to statistically evaluate the expectation values, by taking an average of the result. The result of this process is an estimation of the trace of a unitary matrix of arbitrary size, with a computational time which is independent of this size.

2.4 Implementation of Quantum Computing

2.4.1 The DiVincenzo criteria

In order to provide a physical implementation of a qubit, any two-state system capable of exhibiting quantum superposition of states is required[1]. In 2000,

[1]More generally, it is possible to implement quantum computation using base units of information with two or more states, for example the 'qutrit' which represents a three-state quantum system [33]. However the manipulation of these is challenging in comparison to qubits.

David DiVincenzo outlined a series of requirements which a physical system must reasonably fulfil in order to be a potential candidate for a quantum computer [4]. These are:

1. **Scalability**

   The number of well-characterised qubits comprising the system must be able to scale up reliably. This means that it must be possible to extend the system with additional qubits indefinitely without introducing drawbacks such as decoherence.

2. **Initialisation**

   It must be straightforward to prepare the system in a known initial state accurately; that is, the initialisation operation must have high fidelity.

3. **Long coherence times**

   The time taken for decoherence to occur must be much longer than the logic gate operation time.

4. **Universality**

   A universal set of quantum gates must be available.

5. **Measurement**

   It must be possible to measure the state of a given qubit in the system at the end of the computational process.

Two further requirements are provided under the assumption that qubits must be physically transferred to different locations for the purpose of communication;

these include the ability to convert between stationary and moving qubits, and to reliably transfer qubits between locations without significant loss of information. Overall, these criteria have provided a useful system to benchmark the ability of a proposed system to operate as a quantum computer.

2.4.2 Platforms for the practical implementation of quantum computing

Two-state quantum systems are found commonly in nature, so there are a number of potential physical platforms for the production of qubits. The following is an overview of the commonly known platforms which have been the subject of research in the field, including their comparative advantages and disadvantages. This is by no means a comprehensive list of all such platforms that have been considered in research.

- **Neutral atoms**

  Neutral atoms can be implemented as qubits by using the well-defined discrete energy levels of the outer valence electron(s) as the qubit states. A high degree of control over the atomic state can be obtained using lasers, and trapped atoms can be scaled up to large arrays using optical lattices. Unlike ions, atoms are relatively weakly interacting with their environment which aids in the achievement of long coherence times [34].

- **Ions**

  Ions interact strongly with electromagnetic fields, which can therefore

be used for the trapping and control of the qubits. They perturb each other strongly over short distances, so inter-qubit interactions for logic gates can be induced by physically bringing the ions close together. As qubits, ions benefit from very long coherence times [35] and have access to a set of universal gates [36]. The main weakness of the implementation of ions as qubits is their poor scalability.

- **Superconducting circuits**

  Superconducting circuits may be utilised to provide different kinds of qubits, in which the quantisation of charge, flux and energy in a circuit gives rise to the qubit states [37]. Superconductor qubits are scalable and can implement universal logic gates [38], but suffer from short coherence times.

- **Nuclear magnetic resonance**

  Nuclear magnetic resonance (NMR) can be used for quantum information processing by encoding the qubit states on the spins of nuclei in a liquid [39]. NMR can exhibit universality of quantum logic gates and long coherence times. However it suffers from poor scalability due to the exponentially inefficient use of pseudo-pure states [37].

- **Photons**

  Single photons can be employed as qubits, using opposite polarisations to provide the states of the qubit. Photons are robust against decoherence, and can demonstrate universal logic operations [40]. The scalability and potential for photon-based quantum computation is reliant on the

development of high efficiency photon sources and detectors.

Other potential implementations of qubits which have been given interest include quantum dots and dopant impurities in semiconductors. Due to each physical platform displaying both advantages and disadvantages, there is no particular platform considered overwhelmingly advantageous over the others in terms of research potential. The platform of interest in this work is neutral atoms. There are several advantages to using cold neutral atoms as qubits:

1) They are weakly interacting with the environment, which helps to preserve coherence within the system over time.

2) They have well-defined, long-lived and easily controllable energy levels which are ideal to be used as discrete qubit states.

3) There are well-developed experimental techniques for the trapping and manipulation of atoms.

2.4.3 Cold atoms as qubits

The ideal atomic species to be used as qubits are alkali metal atoms. This is because they have one single outer valence electron, making them relatively simple and approximately hydrogen-like, and therefore their properties and behaviour are well understood in current theory. The hyperfine splitting of the ground state provides a two-level system appropriate for application as qubit states. Their electronic transitions can also be driven by laser light with wavelengths produced by common commercial semiconductor laser diodes. Heavier alkali metal elements have an advantage over lighter species in the form of greater hyperfine splitting,

which makes qubit measurement by photonic scattering easier [41]. The species considered and experimented with in this work is rubidium, which is widely used for experiments in atomic and laser physics, and has laser cooling transitions that correspond to near-infrared wavelengths at around 780 nm. Rubidium has a natural isotopic abundance of 72.17% ^{85}Rb and 27.83% ^{87}Rb [42–44].

The atomic structure of rubidium is shown in Figure 2.4. The ground state of the single outer electron is the 5^2S state with $J = 1/2$, and the first excited state is 5^2P which undergoes fine structure splitting into a pair of states with $J = 1/2$ and $J = 3/2$. The ground and excited states undergo hyperfine splitting into F-sublevels. Transitions from $5^2S_{1/2} \rightarrow 5^2P_{1/2}$ are called D_1 transitions, and those from $5^2S_{1/2} \rightarrow 5^2P_{3/2}$ are known as D_2 transitions. To obtain a two-level system as is required for qubit operation, the ground state hyperfine split energy levels of ^{87}Rb, $5^2S_{1/2}$ $F = 1, 2$, are used. There is no spontaneous emission causing population to decay from the upper hyperfine level to the lower, as this transition is forbidden by the electric dipole transition selection rule $\Delta l = \pm 1$[2]. Therefore these two states have an effectively infinite decay lifetime and stable populations.

Quantum computational processes generally require the ability to manipulate and measure the states of individual qubits. In order for atomic qubits to be individually distinguished and addressed in this way, single or small numbers of atoms comprising each qubit must be confined in a precise location, spatially separated from the other qubits. This allows the control and probing of specific qubit states using lasers, which are also used for the cooling and trapping of the

[2]The electric dipole transition selection rule $\Delta l = \pm 1$ arises from the fact that an emitted photon must carry some angular momentum away from the atom.

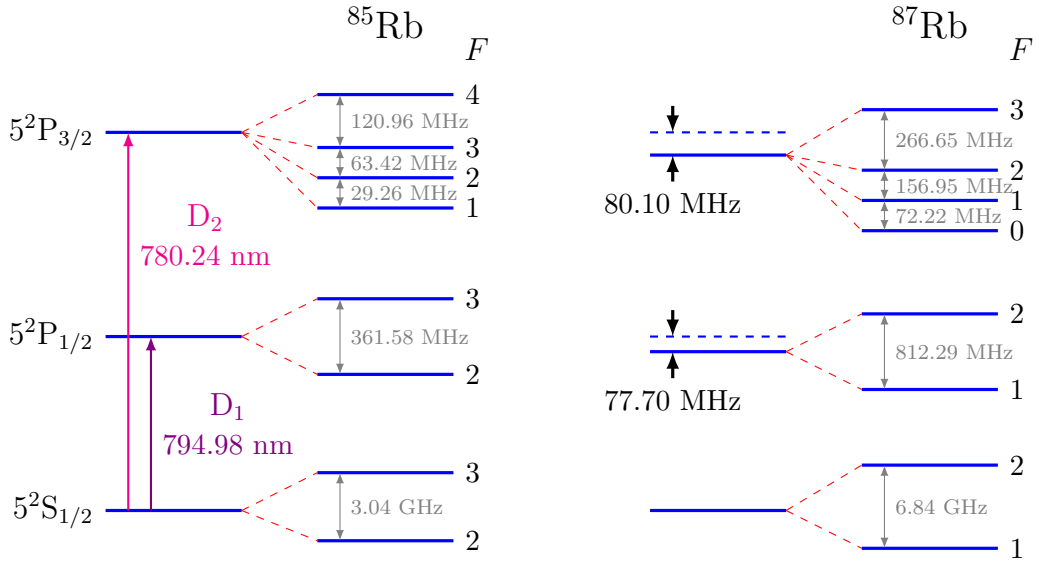

Figure 2.4: The atomic energy level structure of rubidium. The ground S-state of the valence electron undergoes hyperfine splitting into a pair of states with different F-quantum numbers. The first excited P-state undergoes fine structure splitting into two levels with $J = 1/2$ and $J = 3/2$, which are further split into hyperfine sublevels. The discrepancy of the F-values between ^{85}Rb and ^{87}Rb where $F = I + J$ is due to the different nuclear spin quantum number: $I = 5/2$ for ^{85}Rb and $I = 3/2$ for ^{87}Rb. The frequency separation between adjacent levels is shown.

atoms, with well developed and widely used techniques based on the atom-light interaction as described in chapter 3. The dipole trapping technique in particular is ideal for the preparation of atoms as qubits, due to the ability to hold tiny numbers of atoms at precise locations and move them around. For this reason a dipole trap is also known as an optical tweezer. This method involves focussing a laser beam to a tight focus with high intensity towards which atoms are pushed by the dipole force, which is explained in greater detail in section 3.3. Arrays of atomic qubits can be created using multiple dipole traps, either with more than one input trapping beam or by creating arbitrary patterns of traps using a spatial light modulator (SLM) [45]. Arrays of traps can also be produced by creating a standing wave potential formed from counter-propagating beams, known as an optical lattice [46–48].

The practical implementation of qubits fulfils one of the major requirements for quantum computation, allowing the storage of quantum information. The other major requirement is the application of quantum gates, enabling the processing of this information and the computation itself. This requires some form of perturbation or interaction between qubits over the length scale of qubit separation. Some of the physical platforms for quantum computation have readily available mechanisms for this perturbation, for example the electromagnetic interaction between trapped ions. However, neutral atoms are normally weakly interacting over long distances. In this case, interactions may be conveniently produced in the form of the strong van der Waals and dipole-dipole interactions induced by the excitation of the atoms to highly excited states, known as Rydberg states. The properties of these states are unusual, leading to a range of useful

applications. The key features of Rydberg states will be discussed in the following section.

2.4.4 Rydberg interactions for logic gates

Rydberg states are atomic states in which the outer valence electron is excited to a very high principal quantum number $n \gtrsim 20$. At these high values a monovalent Rydberg atom can be accurately described by equations relating to the properties of hydrogen atoms, as the single valence electron is far from the atomic nucleus and core of inner electrons which shield the nucleus. However, it is appropriate to apply a correction factor known as the quantum defect which accounts for highly elliptical orbits of the valence electron, as a result of electronic wavefunctions with certain angular momentum quantum numbers. In these cases, the position of the valence electron may enter the inner core of electrons and experience the attractive Coulomb interaction with the entire unshielded nucleus. The valence electron may also cause polarisation of the inner core of electrons. This modifies the potential and increases the binding energy of the outer electron for a given n compared to the hydrogen atom. Because of this, the energy levels of the atom are modified and it is convenient to apply a correction factor to the principal quantum number in the form of the quantum defect to allow the equations used for hydrogen to be applied to alkali metal atoms. Therefore the atom is described by the effective principal quantum number, given by $n^* = n - \delta_{lj}(n)$ where $\delta_{lj}(n)$ is the quantum defect [49].

The very high effective principal quantum number of Rydberg atoms gives them many remarkable properties. The orbital radius R scales as $R \propto n^2$, approaching

the μm-scale for Rydberg atoms, and therefore the dipole moment $d = er$ can easily increase by three to four orders of magnitude. The polarisability of these atoms quickly becomes comparatively enormous, scaling with n^7. The radiative lifetime of these atoms is also very large, scaling with n^3, meaning that Rydberg states are radiatively stable and long-lived. However, at high principal quantum numbers the atomic energy levels become very closely spaced, as the energy level spacing scales with n^{-3}. Transitions between these close energy levels may be induced by interaction with blackbody radiation [50], limiting the effective lifetime of Rydberg states to approximately a few μs for rubidium [51]. The orbital radius R may be described by analogy to the Bohr model of the atom, given by

$$R = \frac{4\pi\epsilon_0 n^2 \hbar^2}{Ze^2 m_e}, \tag{2.14}$$

where ϵ_0 is the vacuum permittivity, Z is the atomic number, e is the electron charge and m_e is the electron mass.

Due to their high polarisability, permanent dipole moments may be very easily induced in Rydberg atoms with an applied electric field. With no electric field applied, Rydberg atoms have time-varying non-permanent dipole moments and can interact strongly with each other by the van der Waals [52] or resonant dipole-dipole interaction [53, 54], the strength of which increases the closer the atoms are to each other [41, 55]. These strong interactions allow Rydberg atoms to demonstrate a phenomenon known as the Rydberg or dipole blockade [56, 57]. The Rydberg blockade occurs when a Rydberg atom is in close proximity with other atoms, within the blockade radius R_b which can extend up to tens of μm for highly excited Rydberg states. The interaction causes the energy levels of

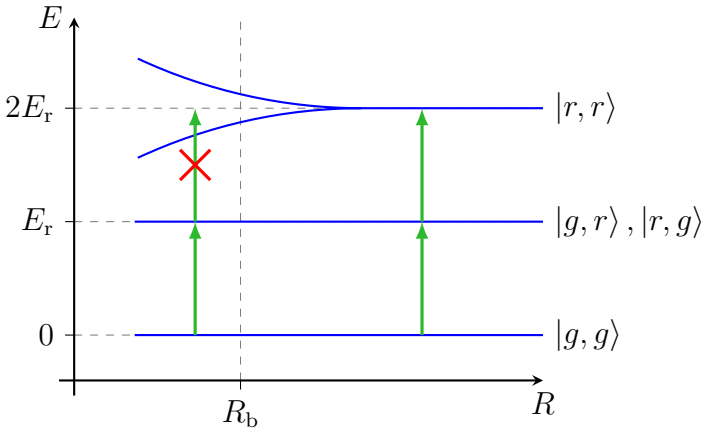

Figure 2.5: Diagram demonstrating the Rydberg blockade for two atoms separated by a distance R. The energy of the two-atom system, E, is shown as a function of R. When the atoms are far apart, so that $R > R_\mathrm{b}$ where R_b is the blockade radius, both atoms can be excited from their ground state $|g\rangle$ to the Rydberg state $|r\rangle$ by laser light. When the atoms are close to each other, so that $R < R_\mathrm{b}$, the strong dipole-dipole interaction induced by one of the Rydberg excitations shifts the doubly-excited state energy level out of resonance so that double excitation is no longer possible.

nearby atoms to be shifted significantly. This leads to the laser radiation coupling the transition to the Rydberg state no longer being resonant with the shifted transition frequency, so that atoms within the blockade radius are not excited to a Rydberg state, leading to a single Rydberg excitation within the blockade radius. This phenomenon is demonstrated schematically in Figure 2.5. The Rydberg blockade can be used to excite an ensemble of atoms into a single collective excitation state [56, 58], and can also allow one atom to act as a control to switch on or off the Rydberg excitation in nearby atoms, depending on whether the control atom is in a Rydberg state or not.

For a pair of atoms in highly excited states separated by a distance R, the interaction is governed by two different mechanisms depending on the separation of the atoms. The atom pair primarily experiences a van der Waals interaction

energy at long distances for $R > R_{\mathrm{vdW}}$ where R_{vdW} is known as the van der Waals radius, and at short distances with $R < R_{\mathrm{vdW}}$ the interaction is dominated by the resonant dipole-dipole interaction [59]. The corresponding shift induced in the energy levels is given by C_6/R^6 for the van der Waals interaction and C_3/R^3 for the resonant dipole-dipole interaction, where C_6 and C_3 are known as C-dispersion coefficients from the expansion of the interaction potential in terms of R [57,60]. The dispersion coefficients for the long-range interaction have been calculated in [61] and in [60] by second order perturbation theory[3]. The coefficient C_6 scales as n^{11}, demonstrating a large increase with highly excited Rydberg states. The Rydberg blockade radius R_{b}, being the characteristic length scale within which there cannot be more than one excitation to Rydberg state, can be calculated by [62–64]

$$R_{\mathrm{b}} = (C_6/\Omega)^{\frac{1}{6}} \tag{2.15}$$

where Ω is the Rabi frequency, equivalent to the power-broadened linewidth of the transition. The Rabi frequency is an important physical parameter which will be discussed in more detail during the treatment of the atom-light interaction in section 3.1. Examples of calculated blockade radii include $R_{\mathrm{b}} \sim 8$ µm for the $58\mathrm{D}_{5/2}$ pair state [59], $R_{\mathrm{b}} \sim 7$ µm for the $60\mathrm{S}_{1/2}$ pair state [63] and $R_{\mathrm{b}} \sim 4$ µm and ~ 3 µm for the $48\mathrm{S}_{1/2}$ and $42\mathrm{S}_{1/2}$ pair states respectively [65].

An example of how the Rydberg blockade can be used as a resource for the implementation of quantum logic gates between qubits is displayed in Figure 2.6.

[3]The calculated interaction potential depends on numerous terms with different C-coefficients depending on different orders of R, however as the expansion is dominated by the C_6 term it is appropriate to ignore the others.

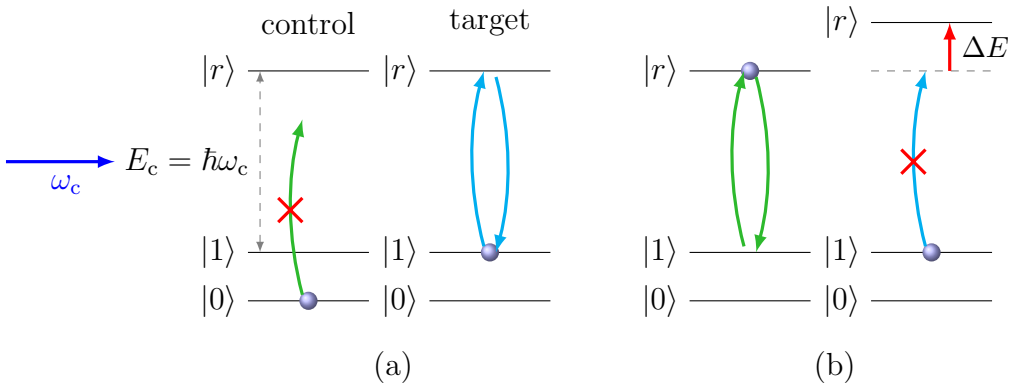

Figure 2.6: Example of a quantum logic gate employing a controlled phase shift of a target atom using the Rydberg blockade, based on [7]. In the case where the control atom is in the $|0\rangle$ state, as shown on the left, it cannot be excited to a Rydberg state by laser light coupling $|1\rangle$ to $|r\rangle$ and the target atom is free to undergo excitation and de-excitation from $|r\rangle$, resulting in a change of phase. In the case shown on the right, a control atom prepared in $|1\rangle$ is excited to $|r\rangle$ creating a Rydberg blockade and preventing the target atom from undergoing the phase rotation.

This example is based on the phase gate presented in [7]. Here, two qubits in the form of atoms are trapped in close proximity to each other. One atom, known as the control qubit, can be initially prepared in one of the two qubit states $|0\rangle$ or $|1\rangle$. If the control qubit is in $|0\rangle$, then incident resonant laser light coupling the $|1\rangle$ and Rydberg $|r\rangle$ states is unable to excite the control atom into the Rydberg state and the Rydberg energy level of the target atom remains unchanged. The target atom can then undergo an excitation to the Rydberg state and subsequent de-excitation back to $|1\rangle$, resulting in a π-phase shift of the atomic wavefunction. If, on the other hand, the control atom is initially in $|1\rangle$, it can be excited to $|r\rangle$ by the resonant laser radiation, causing the Rydberg blockade to occur. The target atom can no longer be excited to the shifted Rydberg energy level and does not acquire a phase shift.

It is possible to form a quantum logic gate based on the phenomenon of Rydberg

blockade which can be used to implement a unitary operation on the state of a qubit. This gate has potential applications in quantum computational protocols such as DQC1 [66, 67]. The implementation of this gate using cold atoms exploits the phenomenon of electromagnetically induced transparency (EIT) to control transitions to the intermediate excited state of a two-photon Rydberg transition, and requires the use of stimulated Raman transitions for the transfer of population between qubit states. A description of electromagnetically-induced transparency and details of the proposal for the quantum logic gate described above are given in the following sections.

2.4.5 Electromagnetically induced transparency

Electromagnetically induced transparency (EIT) is a phenomenon which arises in the presence of three or more atomic levels coupled by electromagnetic radiation. In this situation, interference between excitation pathways in the energy level structure of the atom can cause an atomic transition to become transparent to the radiation coupling the transition. This phenomenon can allow a quantum gate to be implemented by making use of the Rydberg blockade for the controlled unitary interaction in DQC1 [55, 67]. The experimental signature of EIT is the presence of a narrow transmission peak at the centre of a Doppler-broadened absorption feature, where a transition has become transparent to incoming laser light. This narrow transmission peak can be utilised in a frequency locking system for the blue coupling laser in our experiment.

We denote the energy levels of a simplified three-level atom model as the ground state $|1\rangle$, intermediate state $|2\rangle$ and excited (Rydberg) state $|3\rangle$, as displayed

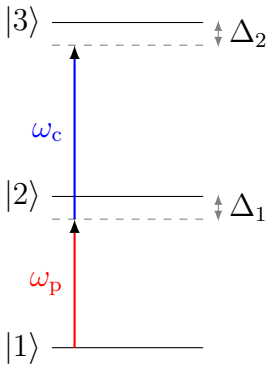

Figure 2.7: The three-level electromagnetically induced transparency (EIT) scheme. The ground state $|1\rangle$ is coupled to an intermediate state $|2\rangle$ by the probe beam with frequency ω_{p}. The intermediate state is coupled to the excited state $|3\rangle$ by the coupling beam with frequency ω_{c}. When the coupling beam is much stronger than the probe beam and the two-photon resonance condition $\delta = \Delta_1 - \Delta_2 = 0$ is fulfilled, the system can enter a 'dark' state in which there is no absorption into or emission from the intermediate state.

schematically in Figure 2.7. The transition from $|1\rangle$ to $|2\rangle$ and from $|2\rangle$ to $|3\rangle$ are driven by near-resonant lasers known as the probe and coupling beams respectively. The probe beam has frequency ω_{p} and couples the transition shown by the red arrow in the Figure, and the coupling beam has frequency ω_{c} and is represented by the blue arrow. The levels $|1\rangle$ and $|3\rangle$ are not coupled to each other by radiation. There are a few different interpretations as to what the physical process is which leads to a zero population in the intermediate state. One interpretation outlined in [68] is based on the formation of a 'dark state' in the three-level atom model. Here, the atom-light interaction may be described by the interaction Hamiltonian

$$H_{\mathrm{int}} = -\frac{\hbar}{2}\begin{pmatrix} 0 & 0 & \Omega_{\mathrm{p}} \\ 0 & -2\left(\Delta_1 - \Delta_2\right) & \Omega_{\mathrm{c}} \\ \Omega_{\mathrm{p}} & \Omega_{\mathrm{c}} & -2\Delta_1 \end{pmatrix}, \tag{2.16}$$

where Ω_p and Ω_c are the Rabi frequencies describing the interaction of the atom with the probe beam and coupling beam respectively, and Δ_1 and Δ_2 are the frequency detunings from resonance of the respective probe and coupling beams, as displayed in Figure 2.7.

Under the two-photon resonance condition, $\delta = \Delta_1 - \Delta_2 = 0$, the eigenstates of this hamiltonian are

$$|a_0\rangle = \cos\theta\,|1\rangle - \sin\theta\,|3\rangle\,, \tag{2.17}$$

$$|a_+\rangle = \sin\theta\sin\phi\,|1\rangle + \cos\phi\,|2\rangle + \cos\theta\sin\phi\,|3\rangle\,, \tag{2.18}$$

$$|a_-\rangle = \sin\theta\cos\phi\,|1\rangle - \sin\phi\,|2\rangle + \cos\theta\cos\phi\,|3\rangle\,, \tag{2.19}$$

where θ and ϕ are known as mixing angles and are related to Ω_p, Ω_c and Δ_1. When the coupling beam has high power and the probe beam remains weak, fulfilling the condition $\Omega_p \ll \Omega_c$, the states $|a_+\rangle$ and $|a_-\rangle$ are shifted in energy and become a pair of dressed states known as an Autler-Townes doublet. The eigenstate $|a_0\rangle$ is known as a dark state because it has no component of the intermediate level $|2\rangle$, so that when the system is prepared in this state there is no absorption into or emission from $|2\rangle$. Therefore the probe beam is not absorbed by the medium, causing the transparency phenomenon to occur.

An alternative interpretation of the physical mechanism driving EIT, also described in [68], is based on the quantum interference of excitation pathways within the three-level system. Here, absorption from the ground state into the intermediate state can occur through two different excitation pathways, namely $|1\rangle \to |2\rangle$ and $|1\rangle \to |2\rangle \to |3\rangle \to |2\rangle$. Under the conditions for EIT, being

$\delta = 0$ and $\Omega_p \ll \Omega_c$, the probability amplitudes for the transitions along the two pathways are approximately equal in amplitude and opposite in sign, effectively cancelling out the transition into the intermediate state.

2.4.6 A quantum logic gate using Rydberg atoms

For the application of neutral atoms as qubits, both hyperfine-split energy levels of the ground state of the atoms are utilised to obtain the two-state system required for qubit operation. In the case of ^{87}Rb these are the $5^2S_{1/2}$ $F = 1$ and $F = 2$ states. The separation between these two levels is $6.835 \times 2\pi$ GHz [69], which corresponds to a 43.86 mm wavelength of electromagnetic radiation, in the microwave range. While population transfer between the two qubit states can be driven by coupling with resonant microwave radiation [70–72], it is useful for the transfer to be driven by a two-photon transition via an intermediate excited state, as this enables the transfer to be controlled by utilising the EIT effect, as discussed in this section. This also conveniently allows the transition to be driven using the cheaply produced near-infrared lasers used for the cooling transition of rubidium, operating at 780 nm for the $5^2P_{3/2}$ excited state. In the following, a possible implementation of a quantum logic gate for neutral atoms using such a two-photon transfer between ground hyperfine levels while exploiting the properties of Rydberg atoms and EIT, proposed by [67], is presented. This scheme is capable of implementing a logical CNOT operation.

To represent the energy levels used in this implementation, the description of the EIT scheme in the previous section must be modified to include both ground state levels. The intermediate excited state is the $5^2P_{3/2}$ state of rubidium, and

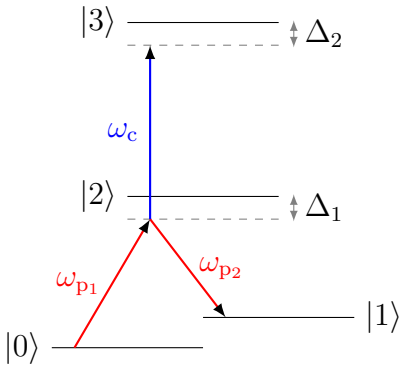

Figure 2.8: The four-level EIT scheme featuring a pair of ground states corresponding to the qubit states $|0\rangle$ and $|1\rangle$. These two states are coupled to the intermediate state by a pair of lasers in Raman configuration, at slightly different frequencies ω_{p_1} and ω_{p_2}. When the EIT condition is fulfilled, the transparency of the intermediate state prevents Raman transitions from occurring between the two ground states.

the highest excited level is a Rydberg state with high n. The system of a single atom is now a four-level system, consisting of the two qubit states $|0\rangle$ and $|1\rangle$, the Rydberg state $|3\rangle$, and the intermediate state, $|2\rangle$. This system is demonstrated in Figure 2.8. The probe beam transition may now be implemented by a pair of lasers in Raman configuration. This configuration consists of phase-locked beams coupling each ground state to an energy at a detuning of Δ_1 away from the intermediate level so that the two-photon resonance condition for the Raman beams is fulfilled, that is, the frequency difference between the two Raman beams must equal the difference between the two qubit states[4]. Raman beams are generally detuned from the intermediate state to minimise the population and spontaneous emission from this state. The two-photon resonance condition for EIT is still fulfilled, $\delta = \Delta_1 - \Delta_2$, and the Raman beams are kept at a low

[4]There are a few ways to obtain beams with this frequency difference, including producing sidebands in a single beam using an electro-optic modulator (EOM), or by simply using two different lasers, provided they are phase-locked.

intensity in comparison to the coupling beam, so that EIT may occur.

A qubit state can be rotated around the Bloch sphere by Raman transitions, which mathematically corresponds to a unitary operation being applied to the qubit state [73]. Therefore, considering the DQC1 protocol setup described in section 2.3 and illustrated in Figure 2.3, consisting of a spatially separated control qubit and ensemble of qubits, a logic gate using the control qubit and involving Raman transitions of the ensemble would fulfill the unitary operation in this circuit, enabling the implementation of quantum computational processes such as DQC1 [55]. Such a quantum gate has been described in [67], and the operation of this gate is shown schematically in Figure 2.9. The scheme relies on long range Rydberg interactions between the control and ensemble qubits to set up a logic gate using the Rydberg blockade, as well as the four-level EIT scheme described above.

The operation of the gate is as follows. The control qubit and ensemble are held in traps near each other. The system is irradiated with laser light at three different frequencies: ω_c for the coupling beam in the four-level EIT scheme in the ensemble qubits, and a pair of Raman beams at ω_{p_1} and ω_{p_2} which constitute the probe beams for EIT in the ensemble. The ensemble atoms are all prepared in the same initial state, either $|0\rangle$ or $|1\rangle$. The control qubit can be prepared in either the $|0\rangle$ or $|1\rangle$ state. If it is in the $|0\rangle$ state, it is not excited to the Rydberg state and does not exert a strong long range dipole-dipole interaction with the ensemble atoms. Therefore, the two-photon resonance condition for EIT is fulfilled for the ensemble atoms, and the intermediate state $|2\rangle$ becomes 'transparent', with no absorption into or emission from this state. This allows

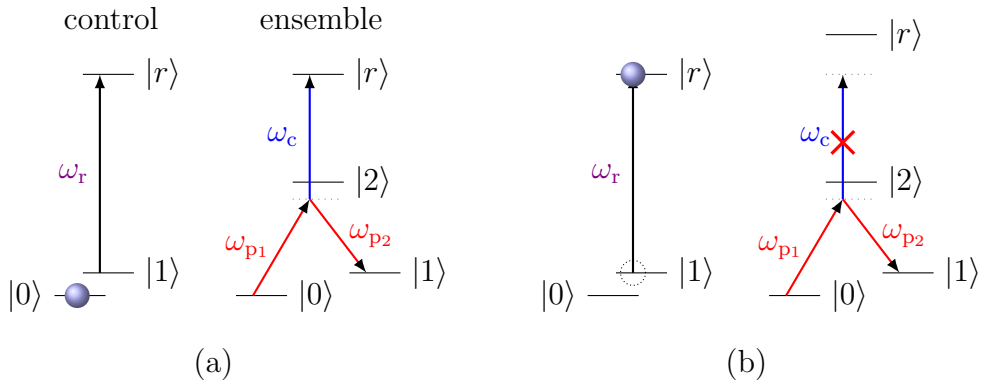

Figure 2.9: Design of a quantum logic gate using cold atoms as described in [67]. A single atom acts as the control qubit, and is excited by a two-photon transition of frequency ω_r coupling the $|1\rangle$ and $|r\rangle$ (Rydberg) states. The target qubit is a spatially separated trapped ensemble of atoms in the four-level EIT scheme shown in Figure 2.8. See text for a description of the operation of this gate.

no Raman transfer to occur between the ground hyperfine states of the ensemble atoms, so they must remain in their initial state.

If the control qubit is instead initially prepared in the $|1\rangle$ state, upon the application of the blue coupling beam and red probe beam at ω_{p_2} it is excited into the Rydberg state, $|3\rangle$, by a two-photon transition. Now, assuming the ensemble atoms are within the Rydberg blockade radius of the control qubit, the blockade occurs with the Rydberg state being shifted out of resonance with the coupling beam. Now the EIT condition is broken for the ensemble atoms, allowing off-resonant Raman transitions to occur and population can be swapped between the $|0\rangle$ and $|1\rangle$ states[5]. This represents a quantum CNOT gate, as the NOT operation is applied to the qubit states of the ensemble atoms conditionally, depending on the state of the control qubit.

[5]The efficiency of both the two-photon control atom excitation and the Raman transition for the ensemble atoms can be maximised using a technique called Stimulated Raman Adiabatic Passage (STIRAP), which involves the application of the two excitation frequencies as overlapping pulses [74–77].

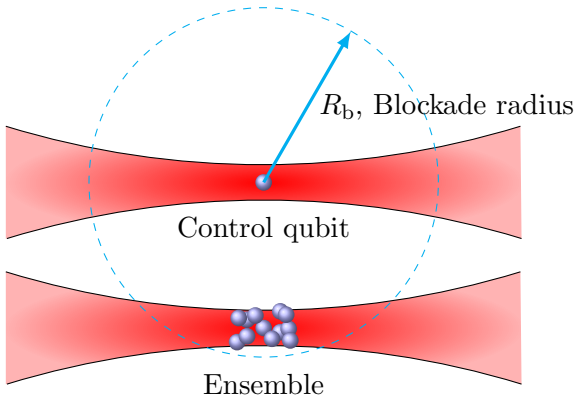

Figure 2.10: Initial setup of the experimental implementation of the DQC1 model. The control and ensemble qubits are trapped in separate dipole traps a very small distance from each other ($\sim$ a few µm). One or more of the ensemble atoms lie within the Rydberg blockade radius of the control qubit, allowing the Rydberg-controlled quantum gate shown in Figure 2.9 to be implemented.

The dipole trapping technique is used to hold the control and ensemble qubits in place within the Rydberg blockade radius of each other, as shown in Figure 2.10. Arbitrary trap geometries such as this can be produced using a device known as a spatial light modulator (SLM), which can divide a single incident laser beam into multiple outgoing beam paths after reflection from a liquid crystal surface [13,45]. A pair of traps may also be produced by passing two beams from a beam splitter at slightly different incident angles through the same high numerical aperture lens [78].

An important process in many quantum computational protocols is the initialisation of the control qubit into an equal superposition of $|0\rangle$ and $|1\rangle$ states. This is normally done before performing a two- or more qubit gate to benefit from the quantum speedup provided by the degree of entanglement between the two states. In the example of the DQC1 protocol, this initialisation is implemented before the unitary operation, and is represented by the Hadamard gate in the

DQC1 quantum circuit in Figure 2.3. The $|0\rangle$ and $|1\rangle$ states are implemented by the ground state hyperfine levels of rubidium, $|5^2S_{1/2}\ F = 1\rangle$ and $|5^2S_{1/2}\ F = 2\rangle$ respectively. The physical realisation of this single-qubit gate is described in [55] where it was inspired by [79]. Here, the control qubit is optically pumped into the $|1\rangle$ state by applying a circularly-polarised beam. A Raman transition can then be used to produce the superposition of states, given by $|+\rangle = (|0\rangle + |1\rangle)/\sqrt{2}$. This kind of process can be performed reliably with low fidelity errors of $\approx 10^{-3}$ [80]. A similar process can be used to prepare the ensemble of atoms in a maximally mixed state, which is required for DQC1. In this case, another step is required after the preparation into superposition states with Raman beams, at which point the ensemble atoms are still in pure states and have phase coherence. Optical pumping into the $|5^2P_{3/2}\ F = 3\rangle$ state causes these atoms to spontaneously decay back into the $|+\rangle$ state, but with the coherence destroyed, leaving a maximally mixed many-qubit state.

The final step of the implementation of quantum computation is the readout stage at the end of the experiment. As described in section 2.3, this can be done by measuring the populations of the $|0\rangle$ and $|1\rangle$ states of the control qubit after applying X or Y rotations to obtain expectation values of the Pauli X and Y spin operators. The population measurement can be done by fluorescence imaging of the control qubit, as resonant laser light at $\approx$ 780 nm coupling the $|0\rangle$ or $|1\rangle$ states to some state in the D_2 line of ^{87}Rb will spontaneously decay, emitting an amount of detectable fluorescent light proportional to the number of atoms initially in the ground state.

2.5 Summary

In this chapter, a basic introduction to the key concepts of quantum computation has been given, including the core components of quantum bits (qubits) and quantum logic gates. There is great research interest and motivation in the real-world application of quantum information processing, as it has been shown to provide significant advantages in efficiency over corresponding classical algorithms for the solution of certain problems. The computational model of DQC1 has been outlined as an example of a protocol which could be implemented experimentally, which would demonstrate a potentially classically intractable calculation in the case where non-trivial unitary operations are considered. Possible physical platforms for the practical implementation of qubits have been discussed, with a focus on neutral atoms which are the subject of the experimental work in this thesis. To fulfil the requirements of a quantum bit of information, atoms must be trapped in a precise, controllable location in order to be individually addressed. The trapping and measurement of atoms can be conveniently carried out using lasers by exploiting the atom-light interaction. Once an array of atomic qubits is produced using these trapping techniques, a method is required for the interaction between separate qubits in order to implement quantum gates, which can be done using the long range dipole interactions induced by Rydberg states.

The trapping of atoms using lasers is a predominant and vital component of the implementation of atoms as qubits. The interaction between atoms and light upon which laser trapping techniques are based contains a wealth of interesting physics, and is described in the following chapter, along with an explanation of the trapping techniques themselves.

Chapter 3

Cooling and Trapping Atoms

Experiments for studying the properties and behaviour of atoms rely heavily on the ability to trap the atoms in a precise location for appreciable experimental timescales, as well as the ability to manipulate the transitions between electronic states. The invention of the laser was instrumental in enabling this high degree of control over atoms, providing monochromatic narrow-linewidth light capable of addressing specific transition frequencies, as well as providing an intense and strongly localised radiation source which could effectively trap and move small numbers of atoms. To provide a theoretical basis for understanding the laser cooling and trapping techniques used for the preparation of ultracold neutral atoms, a review of atom-light interaction will be given in the following section, culminating in the derivation of the photon scattering rate of an atom. Following this, the cooling and trapping techniques required for the operation of the magneto-optical trap will be described in section 3.2, and the physical principles behind the operation of the dipole trap which is capable of preparing small

ensembles of atoms fit for implementation as atomic qubits will be presented in section 3.3.

3.1 Atom-Light Interaction

This section contains a review of the theory of atom-light interaction. The control and measurement of atoms for applications such as quantum information processing rely almost entirely on the interaction between atoms and light, as the excitation to different energy levels in the atom is driven by the absorption of photons of specific frequencies. The detection and measurement of the atoms relies on the detection of spontaneously emitted photons during the decay of the atom back to the ground state. Also, the most commonly used and powerful trapping techniques for neutral atoms rely on their interaction with light. The atom-light interaction can lead to phenomena which are useful for the implementation of quantum processing using atoms, such as electromagnetically-induced transparency. Atom-light interaction is a well-studied and in-depth academic field; this section will contain only the necessary basic concepts required for the understanding of the trapping techniques described in this chapter.

For much of the work done in atom trapping and manipulation, the physical processes of interest usually involve high intensity light sources such as lasers, leading to the interaction between small numbers of atoms with large numbers of photons. It is therefore appropriate to treat the physical picture using a semiclassical approach, in which the atoms are treated with quantum formalism

whereas the electromagnetic field is assumed to behave classically. It will be shown in the following that using this approach, rate equations describing the populations of the atomic energy levels can be derived, as well as the decay rate for the excited state of a two-level atom, which is fundamental to the radiation force on which laser cooling techniques are based [49].

The system of an atom with wavefunction Ψ interacting with an external electromagnetic field is described by the time-dependent Schrödinger equation

$$\mathrm{i}\hbar\frac{\partial\Psi}{\partial t} \;=\; \hat{H}\Psi \tag{3.1}$$

in which the Hamiltonian of the system is given by

$$\hat{H} \;=\; \hat{H}_0 \;+\; \hat{H}'(t) \tag{3.2}$$

where $\hat{H}_0$ is the Hamiltonian of the unperturbed atom and $\hat{H}'(t)$ is the Hamiltonian due to the perturbation caused by the electromagnetic field. The stationary eigenstates of the unperturbed atom are the energy levels $|0\rangle, |1\rangle, \ldots, |n\rangle$ for an n-level atom, with energies $E_0, E_1, \ldots, E_n$. The system described by the full Hamiltonian including the perturbation can be expressed in terms of these unperturbed stationary states as

$$\Psi \;=\; \sum_{k=1}^{n}\Psi_k, \qquad \Psi_k \;=\; c_k\,|k\rangle\,e^{-\mathrm{i}\omega_k t} \tag{3.3}$$

where c_k are time-dependent coefficients, the square magnitude of which, $|c_k|^2$, is the probability amplitude of the system being in the state Ψ_k. The angular

frequency in the complex phase term $\omega_k = E_k/\hbar$. The coefficients are normalised such that

$$\sum_{k=1}^{n} |c_k|^2 = 1. \tag{3.4}$$

The interaction between an atom and an external electric field $\boldsymbol{\mathcal{E}} = \boldsymbol{\mathcal{E}}_0 \cos(\omega t)$ arises due to the electric dipole moment of the atom $\mu_e = -e\boldsymbol{r}$, where $\boldsymbol{r}$ is the displacement of the electron from the centre of the atom. The Hamiltonian of the perturbation is given by the scalar product of the dipole moment with the electric field,

$$\hat{H}'(t) = e\boldsymbol{r} \cdot \boldsymbol{\mathcal{E}}_0 \cos(\omega t), \tag{3.5}$$

where ω is the angular frequency of the electromagnetic radiation. Solving the time-dependent Schrödinger equation in equation 3.1 using the full Hamiltonian including the perturbation term, and using the wavefunction in terms of the time-dependent energy level coefficients as in equation 3.3, the time evolution of the probability amplitude for each state k can be found,

$$\mathrm{i}\hbar \frac{\partial c_k}{\partial t} = \sum_{l=1}^{n-1} c_l \hat{H}'_{kl}(t)\, e^{-\mathrm{i}\omega_{kl} t}, \tag{3.6}$$

being a sum over all other states l as the energy levels of the atom are coupled from the electric field interaction. The frequency ω_{kl} comes from the difference in energy between the two states, $\omega_{kl} = (E_k - E_l)/\hbar$. The Hamiltonian matrix element $\hat{H}'_{kl}(t) = \langle \Psi_k | \hat{H}'(t) | \Psi_l \rangle$. In order to solve this set of equations, the problem must be simplified, which can be done by considering the most basic

scenario of a two-level atom. In this case, the wavefunction of the system is

$$\Psi \;=\; c_1 \left|1\right\rangle e^{-\mathrm{i}\omega_1 t} \;+\; c_2 \left|2\right\rangle e^{-\mathrm{i}\omega_2 t}. \tag{3.7}$$

For the simplified model of the two-level atom, using the interaction Hamiltonian given in equation 3.5, the solutions to equation 3.6 are given by

$$\mathrm{i}\frac{\partial c_1}{\partial t} \;=\; \Omega \cos\left(\omega t\right) e^{-\mathrm{i}\omega_{21} t} c_2, \tag{3.8}$$

$$\mathrm{i}\frac{\partial c_2}{\partial t} \;=\; \Omega^* \cos\left(\omega t\right) e^{\mathrm{i}\omega_{21} t} c_1, \tag{3.9}$$

where Ω is the Rabi frequency, which depends on the dipole interaction matrix elements as

$$\Omega \;=\; \frac{1}{\hbar} \left\langle 1 | e\boldsymbol{r} \cdot \boldsymbol{\mathcal{E}}_0 | 2 \right\rangle. \tag{3.10}$$

The Rabi frequency represents the frequency of the cyclic transition of atomic population between the two energy levels of the atom, by absorption and subsequent stimulated emission, in the presence of an oscillating electric field at resonant frequency[1]. Equations 3.8 and 3.9 can be rewritten in terms of the frequency detuning of the incident radiation from resonance $\Delta = \omega - \omega_{21}$. In order to simplify the resulting equations, the rotating wave approximation is used, which relies on the assumption that the detuning Δ is very small compared to the electric field frequency ω. This means that exponential terms in the form of $e^{\mathrm{i}\omega t}$ oscillate rapidly and average to zero compared to the more slowly evolving

[1]This cyclic behaviour is known as Rabi flopping, named after 1944 Nobel laureate for Physics Isidor Isaac Rabi, awarded for the discovery of Nuclear Magnetic Resonance (NMR). With knowledge of the Rabi frequency, which depends on the coupling strength and amplitude of the driving electric field, the duration of an incident pulse of electromagnetic radiation can be manipulated to prepare the atomic population in one of the states.

$e^{\mathrm{i}\Delta t}$ terms, and can be ignored. Therefore these equations can be rewritten as

$$\mathrm{i}\frac{\partial c_1}{\partial t} = \frac{\Omega}{2}e^{-\mathrm{i}\Delta t}c_2, \tag{3.11}$$

$$\mathrm{i}\frac{\partial c_2}{\partial t} = \frac{\Omega}{2}e^{\mathrm{i}\Delta t}c_1. \tag{3.12}$$

From here, a further approximation is made in order to simplify the calculation, known as the dipole approximation. The dipole approximation assumes the wavelength of the incident radiation is much greater than the size of the atom, which in the case of rubidium (being the atomic species of interest in this work) is a reasonable approximation as the wavelength of radiation for excitation to the first excited state is 780 nm whereas the atomic radius is $<$ 1 nm. This assumption allows the electric field amplitude $\mathcal{E}_0$ to be treated as constant over the spatial extent of the atom and brought outside the scalar product in equation 3.10. Taking the dipole approximation into account, and starting with initial conditions $c_1(t=0) = 1$ and $c_2(t=0) = 0$ corresponding to the entire atomic population being in the ground state at $t = 0$, the solutions to equations 3.11 and 3.12 are given by[2]

$$c_1(t) = \left[\cos\left(\frac{Wt}{2}\right) + \mathrm{i}\frac{\Delta}{W}\sin\left(\frac{Wt}{2}\right)\right]e^{-\mathrm{i}\Delta t/2}, \tag{3.13}$$

$$c_2(t) = -\mathrm{i}\frac{\Omega}{W}\sin\left(\frac{Wt}{2}\right)e^{\mathrm{i}\Delta t/2} \tag{3.14}$$

where $W = \sqrt{\Omega^2 + \Delta^2}$ is known as the generalised Rabi frequency. While driven

[2] If the driving radiation is weak, most of the population remains in the ground state, $c_1(t) = 1$, and the excited state population is instead described by a sinc function $((\sin x)/x)$ dependent on t and the detuning $\omega_{21} - \omega$. Treatment of this solution in the presence of broadband radiation described by an energy density $\rho(\omega)$ for frequencies between ω and $\omega + \mathrm{d}\omega$ leads to the derivation of the Einstein B-coefficients [49].

continuously by a detuned electric field, the excited state population evolves as

$$|c_2(t)|^2 = \frac{\Omega^2}{W^2}\sin^2\left(\frac{Wt}{2}\right) \tag{3.15}$$

and the population oscillates between the two levels at the generalised Rabi frequency. For a system in which the entire population begins in one of the two levels, when driven for a duration $Wt = \pi$, known as a π-pulse, all of the population is transferred from this initial state into the other. A $\pi/2$ pulse, in which the radiation is applied for a duration $Wt = \pi/2$, results in the two-level atomic wavefunction beginning in one state being prepared in an equal superposition of the two states. This is an important process in quantum computational algorithms based on atoms, as it can be used to achieve entanglement in an initially prepared atom for the computational speedup obtained in quantum computing, as described in section 2.2.

In the above treatment of atom-light interaction, spontaneous emission of photons by the atom has been neglected, so far considering only absorption and stimulated emission. To include spontaneous emission, it is useful to first describe the wavefunction Ψ of the atom in the presence of driving radiation using density operator formalism, as introduced in section 2.1. The wavefunction is given by $\Psi = \begin{pmatrix} c_1 \\ c_2 \end{pmatrix}$ in the basis of the two atomic levels, $\psi_1 \equiv |1\rangle = \begin{pmatrix} 1 \\ 0 \end{pmatrix}$ and

$\psi_2 \equiv |2\rangle = \begin{pmatrix} 0 \\ 1 \end{pmatrix}$. Now, the density matrix of the system

$$\rho = \begin{pmatrix} \rho_{11} & \rho_{12} \\ \rho_{21} & \rho_{22} \end{pmatrix} = |\Psi\rangle \langle\Psi| = \begin{pmatrix} |c_1|^2 & c_1 c_2^* \\ c_1^* c_2 & |c_2|^2 \end{pmatrix}, \tag{3.16}$$

where the diagonal elements represent the populations of the two states and the off-diagonal elements represent the coherences. Utilising the state coefficient rate equations 3.11 and 3.12, the rate of change of the state populations can be written in terms of the coherences as

$$\frac{\partial \rho_{22}}{\partial t} = -\frac{\partial \rho_{11}}{\partial t} = \frac{\mathrm{i}\Omega}{2} \left(\widetilde{\rho}_{21} - \widetilde{\rho}_{12} \right). \tag{3.17}$$

where substitutions $\widetilde{\rho}_{12} = \rho_{12} e^{\mathrm{i}\Delta t}$ and $\widetilde{\rho}_{21} = \rho_{21} e^{-\mathrm{i}\Delta t}$ have been made. The spontaneous decay can now be included in the form of a radiative damping term proportional to the excited state population, given by $-\Gamma\rho_{22}$ where Γ is the radiative lifetime of the excited state[3]. The rate equations for the populations and coherences including spontaneous emission can now be expressed in the form of the well-known optical Bloch equations (OBE):

$$\frac{\partial \rho_{22}}{\partial t} = -\frac{\partial \rho_{11}}{\partial t} = \frac{\mathrm{i}\Omega}{2} \left(\widetilde{\rho}_{21} - \widetilde{\rho}_{12} \right) - \Gamma\rho_{22} \tag{3.18}$$

$$\frac{\partial \widetilde{\rho}_{12}}{\partial t} = \frac{\mathrm{i}\Omega}{2} \left(\rho_{22} - \rho_{11} \right) - \left(\Gamma/2 - \mathrm{i}\Delta \right) \widetilde{\rho}_{12} \tag{3.19}$$

[3]The damping term is only included for the excited state as in the simple model of a two-level atom, the excited state is the only level capable of undergoing spontaneous emission. For a more realistic many-level atom, every level above the ground state has a radiative lifetime.

$$\frac{\partial \widetilde{\rho}_{21}}{\partial t} = \frac{\mathrm{i}\Omega}{2}\left(\rho_{22} - \rho_{11}\right) - \left(\Gamma/2 + \mathrm{i}\Delta\right)\widetilde{\rho}_{21}. \tag{3.20}$$

In the steady-state case for atom-light interaction durations much longer than the radiative lifetime, the time derivatives of the populations and coherences are set equal to zero. The steady-state solution for the excited state population is given by

$$\rho_{22} = \frac{\Omega^2/4}{\Delta^2 + \Omega^2/2 + \Gamma^2/4}. \tag{3.21}$$

Defining the saturation intensity I_{sat} by

$$\frac{I}{I_{\mathrm{sat}}} = \frac{2\Omega^2}{\Gamma^2}, \tag{3.22}$$

the scattering rate of photons by an atom in the presence of incident radiation can be expressed as

$$R_{\mathrm{scatt}} = \Gamma\rho_{22} = \frac{\Gamma}{2}\frac{I/I_{\mathrm{sat}}}{1 + I/I_{\mathrm{sat}} + 4\Delta^2/\Gamma^2}. \tag{3.23}$$

This result is of high importance for the laser cooling techniques widely used for the experimental realisation of trapping ultracold atoms. It is applied in many calculations throughout this work, for example it provides the basis of the calculation of the number of trapped atoms detected in the laboratory by fluorescence imaging.

Light shift

As the atomic wavefunction is perturbed by the interaction with light in the form of the interaction Hamiltonian, the total wavefunction describing the system is

altered due to the perturbation, and therefore the eigenstates of the total system are changed. For the non-interacting two-level atom, the eigenstates represent the energy levels E_1, E_2. The interaction with light introduces a shift in these eigenstates by $\pm\delta E$, where δE is known as the light shift or Stark shift. To calculate the light shift, equations 3.11 and 3.12 can be expressed in matrix form as

$$\mathrm{i}\frac{\partial}{\partial t}\begin{pmatrix}\widetilde{c}_1\\ \widetilde{c}_2\end{pmatrix} = \frac{1}{2}\begin{pmatrix}-\Delta & \Omega\\ \Omega & \Delta\end{pmatrix}\begin{pmatrix}\widetilde{c}_1\\ \widetilde{c}_2\end{pmatrix} \tag{3.24}$$

where the substitutions $\widetilde{c}_1 = c_1 e^{\mathrm{i}\Delta t/2}$ and $\widetilde{c}_2 = c_2 e^{-\mathrm{i}\Delta t/2}$ have been made. The resulting eigenvalues are given by

$$\lambda \;=\; \pm\frac{1}{2}\left(\Delta^2+\Omega^2\right)^{\frac{1}{2}} \;\approx\; \pm\frac{1}{2}\left(\Delta+\frac{\Omega^2}{2\Delta}\right), \tag{3.25}$$

where the approximation is valid for far detuning, $|\Delta| \gg \Omega$, which is applicable in the case of dipole trapping for example. The solutions in the absence of perturbation have $\Omega = 0$, reducing to a pair of levels separated in energy by $\hbar\Delta$, with the light shift $\delta E = \hbar\Omega^2/2\Delta$ introduced for $\Omega > 0$. This effect is shown in Figure 3.1.

During dipole trapping experiments, there is a significant light shift induced by the high intensity laser used for trapping. This causes a change in the resonant frequency required for driving the cooling transition, effectively detuning the cooling laser from this transition, changing the scattering rate. Therefore, when using the cooling beams to acquire fluorescence for measurements such as the number of atoms, knowledge of the induced light shift is important as it affects the fluorescence signal acquired. The light shift induced by the dipole trapping

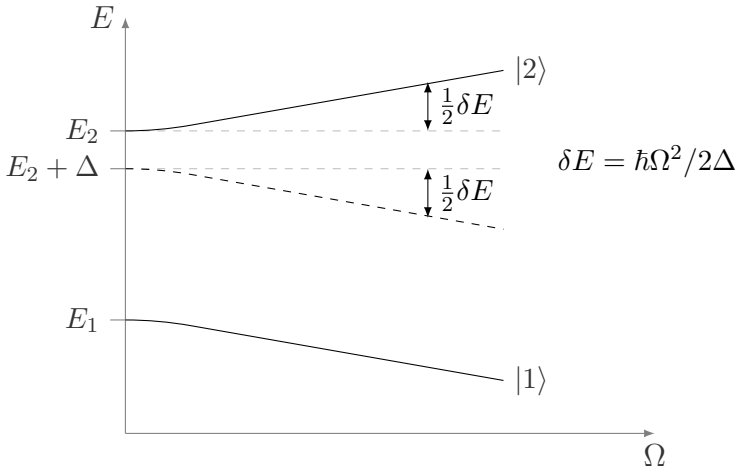

Figure 3.1: The a.c. Stark effect resulting in the light shift δE of energy levels in a two-level atom, for an incident oscillating electric field with frequency ω, detuning Δ and Rabi frequency Ω.

beam was characterised during measurements in the laboratory, discussed in section 5.2.2. In the following section, the laser cooling technique which relies on the atom-light interaction will be described, as well as its application for trapping atoms in the form of the magneto-optical trap (MOT).

3.2 Laser Cooling and Trapping

3.2.1 Doppler cooling

The first step to obtaining stationary, controllable atoms to be used as qubits is to slow them down by cooling and contain them in a trap. To cool the atoms, a highly successful and powerful technique is laser cooling [49]. This technique relies on the Doppler effect, so it is also known as Doppler cooling. The principle behind the technique is illustrated in Figure 3.2. At room temperature, atoms

have a large velocity on the order of magnitude of 100 $\mathrm{m\,s^{-1}}$ in a random direction. A laser providing resonant electromagnetic radiation can excite the atom into a higher energy level. The absorption of a photon causes the atom to recoil and gain momentum equal to the photon momentum, $\hbar k$ where $k = 2\pi/\lambda$ is the wavenumber, in the propagation direction of the photon. When the atom then spontaneously emits a photon and decays back to the lower energy level, the photon will be emitted in a random direction, leading to a loss of momentum for the atom. For continuous incident radiation, the photon scattering rate of the atom is given by equation 3.23. After many cycles of this process, the momentum change due to spontaneous emission averages to zero due to the isotropy of the emission, whereas the momentum gained by absorption increasingly builds in one direction. This is the mechanism behind radiation pressure, in which a beam of photons can apply an effective force on an atom as a result of the overall momentum change in the direction of incidence. This scattering force is given by the photon momentum $\hbar k$ multiplied by the scattering rate,

$$F_{\mathrm{scatt}} = \hbar k R_{\mathrm{scatt}} = \frac{\hbar k \Gamma}{2} \frac{I/I_{\mathrm{sat}}}{1 + I/I_{\mathrm{sat}} + 4\Delta^2/\Gamma^2}. \tag{3.26}$$

Due to the Doppler effect, which is the change in frequency experienced by an atom due to the motion of the atom relative to the frequency source, an atom moving in the same direction as the laser experiences a lower frequency than the actual laser frequency and an atom moving opposite to the laser direction experiences a higher frequency. The detuning of the cooling laser can therefore be tuned to slow only those atoms which are moving opposite to the photon propagation direction. If the laser frequency is red-detuned, then by the Doppler

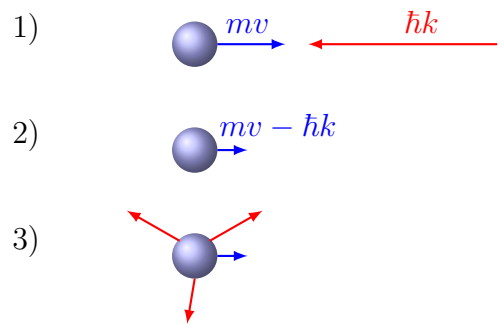

Figure 3.2: Doppler cooling with red-detuned lasers. In step (1), a photon with momentum $\hbar k$ is travelling in the opposite direction to an atom with momentum mv. In step (2), the atom absorbs the photon as it is Doppler shifted into resonance by the atomic motion, exciting the atom and decreasing the momentum of the atom to $mv - \hbar k$. Finally, in step (3), the atom decays back to the ground state, spontaneously emitting a photon in a random direction. Over many cycles of this process, the momentum loss caused by the cooling laser builds up, whereas the momentum change from the photon emission averages to zero.

effect the frequency 'seen' by the atom is higher than the actual frequency, and is shifted towards the resonant frequency of the cooling transition. This allows the cooling cycle described previously to occur, and the atom is affected by radiation pressure in the opposite direction to its motion. The radiation pressure acts as a force causing the atom to slow down, until the laser frequency observed by the atom is no longer within its naturally-broadened absorption linewidth.

Optical molasses

Using a pair of counter-propagating red-detuned lasers will push atoms travelling either way in the opposite direction to their motion. This is because atoms travelling towards one of the lasers will experience a frequency which is Doppler-shifted into resonance with the cooling transition and be pushed in the opposite direction by that laser, whereas they remain unaffected by the

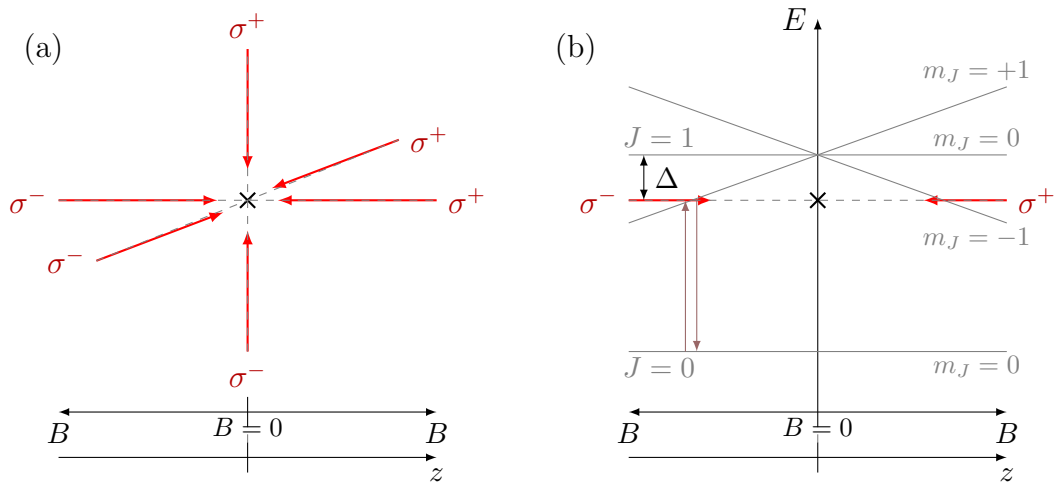

Figure 3.3: The magneto-optical trap (MOT). In (a), a diagram of the MOT is shown. Three orthogonal pairs of counter propagating, oppositely circularly-polarised red-detuned lasers are passed through the trap centre. Atoms in the beam path are cooled by the Doppler cooling technique. A non-uniform magnetic field is produced by external anti-Helmholtz coils, causing the atomic energy levels to be Zeeman shifted into resonance with the beams, red-detuned by Δ, in such a way as to produce a trapping force towards the trap centre. In (b), the Zeeman shift induced in the excited state ($J = 1$) sublevels in one dimension is shown.

counter-propagating laser as it is out of resonance with the cooling transition. This provides a frictional force acting against the motion of the atoms in one dimension, known as optical molasses. Extending this setup to three pairs of counter-propagating beams orthogonal to each other as demonstrated in Figure 3.3 applies a viscous force in all three dimensions, which pushes atoms towards the point at which the beams cross. This technique is capable of cooling atoms down to the Doppler temperature limit, which arises from the non-zero minimum momentum gained from absorbing photons. The Doppler limit for rubidium is 146 μK [42, 43].

A large assumption in the laser cooling method is that the atoms can be described as a two-level system. This is not true in practice for rubidium atoms, which have many energy levels above the ground state of the valence electron including fine and hyperfine splitting, as shown in Figure 2.4. In our experiment, a cooling transition is selected for which selection rules confine the system to be almost two-level. This transition is in the D_2 line, $5^2S_{1/2}\ F = 2 \rightarrow 5^2P_{3/2}\ F = 3$, which is excited by the resonant laser wavelength 780.24 nm [43]. The selection rule $\Delta F = 0, \pm 1$ ensures that the upper level can only spontaneously decay to the $5^2S_{1/2}\ F = 2$ state. There is a chance that the ground state will be excited into the $5^2P_{3/2}\ F = 2$ state, at which point it could decay into the $5^2S_{1/2}\ F = 1$ state, causing atoms to escape from the cooling cycle. In order to restore the atoms back into the cooling process a second laser is required, called the 'repump' laser, which drives the $5^2S_{1/2}\ F = 1 \rightarrow 5^2P_{3/2}\ F = 2$ transition with resonant light of 780.24 nm. The energy level structure with the cooling and repump transitions highlighted is shown in Figure 4.1.

3.2.2 Zeeman degeneracy and optical pumping

The theoretical treatment of the atom in this thesis has so far been described in terms of separate energy levels of differing total angular momentum quantum number F. These energy levels are each composed of $2F + 1$ magnetic sublevels denoted by m_F, which are degenerate in the absence of an applied magnetic field. Transitions from the ground to excited state may change m_F depending on the circular polarisation of the driving radiation. In this case, σ_+ transitions with $\Delta m_F = +1$ are excited by left-circularly polarised light and σ_- transitions with $\Delta m_F = -1$ are excited by right-circularly polarised light. A schematic showing the effect of Zeeman degeneracy on transitions from the ground to first excited state in the D_2 line of ^{87}Rb is displayed in Figure 3.4. When populating the excited state, spontaneous emission may occur allowing any transition with $\Delta m_F = 0, \pm 1$ to the ground state. If driven with one particular circular polarisation, over many cycles of excitation and spontaneous decay the atomic population will eventually gather in one of the two ground states; $m_F = +1/2$ for left-circularly polarised light and $m_F = -1/2$ for right-circularly polarised light. This is a technique known as optical pumping which can be used to prepare an ensemble of atoms, initially randomly distributed among states, in a certain m_F state.

3.2.3 Magneto-optical trap

Laser cooling by itself is enough to cool atoms down to the ultracold temperatures required, but it does not actively trap the atoms at one particular position. The

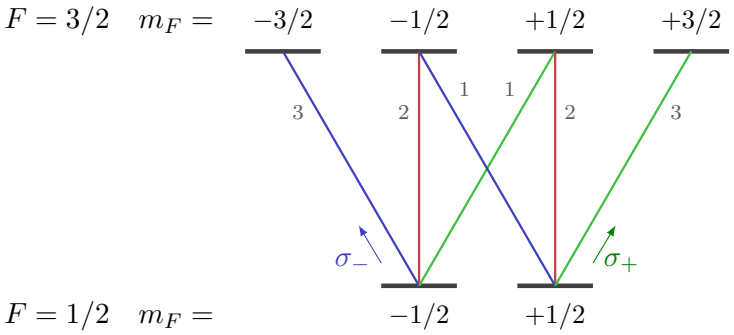

Figure 3.4: The effect of Zeeman degeneracy on transitions from the ground to first excited state in the D_2 line of Rubidium-87. The numbers next to the transition lines show their relative transition strengths. The σ_+ transitions to the excited state with $\Delta m_F = +1$ are driven by left-circularly polarised light and the σ_- transitions with $\Delta m_F = -1$ with right-circularly polarised light, allowing optical pumping into specific m_F states.

three pairs of counter propagating beams can be extended to a trap by exploiting Zeeman splitting, in which the normally degenerate m_F magnetic sublevels are separated in energy to become non-degenerate states when an external magnetic field is applied.

The Zeeman splitting of energy levels can be used in combination with the three-dimensional optical molasses consisting of three pairs of counter-propagating beams to implement the trapping of atoms. This is done by using oppositely circularly polarised beams and applying a non-uniform magnetic field which is zero at the trap centre, where the beams cross, and increases linearly in magnitude radially outwards. The effect of this is that the atomic energy levels undergo splitting into non-degenerate m_F levels, and the magnitude of the splitting increases with distance from the trap centre. This causes the counter-propagating radiation pressure forces to become position-dependent as the Zeeman splitting increases with distance from the trap centre, as

shown in Figure 3.3 (b). Due to the red-detuning of the cooling beams and position-dependent shift in excited state sublevels, atoms are predominantly excited by either σ_+ or σ_- transitions depending on their position. Using the correct orientation of circularly polarised beams, this can be utilised for the trapping of atoms. This can be seen in Figure 3.3 (b), in which transitions to the excited state are only driven by beams directed towards the trap centre. As an atom travels away from the trap centre in one direction, only the laser cooling transition that acts against the motion of the atom becomes shifted closer to resonance, so that there is now a restoring force trapping the atoms at the trap centre, at the point at which the magnetic field is zero. This is known as a magneto-optical trap, or MOT, and is displayed schematically in Figure 3.3 (a). The beam power required for the cooling lasers is roughly a few mW, and the typical detuning of these lasers from resonance during operation of the MOT is on the order of MHz.

3.2.4 Sub-Doppler cooling

An additional effect of the degeneracy of magnetic sublevels in the presence of circularly polarised light is that sub-Doppler cooling occurs, which allows the atoms to be cooled below the theoretical limit achievable when considering only Doppler cooling. The generally accepted explanation for this is by a mechanism known as Sisyphus cooling [81, 82], which is demonstrated schematically in Figure 3.5. To understand this process, a pair of orthogonally linearly polarised overlapping counter-propagating beams is considered, which produces a standing wave with a position-dependent total polarisation. Due to this polarisation

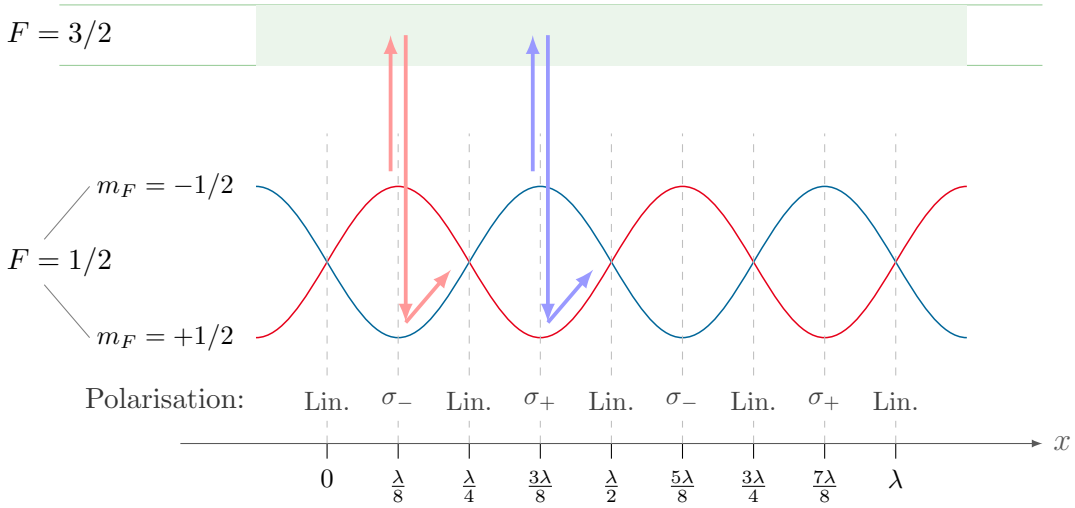

Figure 3.5: Diagram demonstrating the physical mechanism responsible for sub-Doppler cooling, known as Sisyphus cooling. In this situation, a pair of counter-propagating lasers with orthogonal linear polarisations cause a standing wave to arise with a position-dependent polarisation and light shift of the magnetic m_F ground state sublevels. The preferred excitation pathway is from the higher energy sublevel followed by spontaneous decay to the lower energy level, resulting in cooling by loss of kinetic energy.

gradient, there is a spatial variation in the light shift of the two ground-state magnetic sublevels. As an atom in one of these levels moves along the axis of the standing wave, it climbs to the top of the potential hill created by the spatially-dependent light shift, losing kinetic energy in the process. At this point it is possible for the atom to be excited by the circularly-polarised light at this position, corresponding to an excitation from $F = 1/2, m_F = +1/2 \rightarrow F = 3/2, m_F = -1/2$ by a σ_- transition, or from $F = 1/2, m_F = -1/2 \rightarrow F = 3/2, m_F = +1/2$ by a σ_+ transition. It is then more likely for the atom to decay back to the lower energy ground state by spontaneous emission with $\Delta m_F = 0$ due to the greater transition strength, as seen in Figure 3.4, resulting in a loss of energy from climbing the potential hill. This process is cyclic, repeating until the atom has lost enough kinetic energy to prevent it from climbing the potential hill again. This energy loss provides an additional source of cooling for the atoms below the Doppler limit.

Despite the explanation for Sisyphus cooling originating from a scenario with two linearly polarised counter-propagating beams, in contrast to the magneto-optical trap which utilises oppositely circularly polarised counter-propagating beams, a form of the mechanism still occurs at the trap position where the three pairs of beams overlap. This is due to the resulting complex standing wave pattern formed when the three beam pairs are overlapping, which allows Sisyphus cooling to occur [83]. The temperature achievable in the molasses as a result of sub-Doppler cooling is below the sub-Doppler limit, and may be as low as tens of μK.

3.3 Dipole Trapping

In order to implement models for quantum computation using atoms as qubits, we need to be able to trap and manipulate individual atoms and small dense ensembles up to hundreds of atoms in size, as well as controlling their position to a high precision on the μm scale. To achieve this, a powerful method known as dipole trapping is used. A dipole trap is only capable of trapping atoms which are already at sub-Doppler temperatures due to typically having a much shallower trap depth compared to the MOT, so the MOT is used as a preliminary stage to prepare atoms to be loaded into dipole traps.

When exposed to an electric field produced by a laser, a dipole moment is induced in an atom, which oscillates at the laser frequency, ω. The atom then experiences an interaction potential known as the dipole potential, which is given by [84]

$$U_{\text{dip}}(\mathbf{r}) = -\frac{1}{2\epsilon_0 c}\text{Re}(\alpha) I(\mathbf{r}), \tag{3.27}$$

where $I(\mathbf{r})$ is the position-dependent electric field intensity, ϵ_0 is the vacuum permittivity and $\alpha \equiv \alpha(\omega)$ is the complex polarisability of the system. The real part of this polarisability corresponds to the dispersive properties of the light field, whereas the imaginary part corresponds to the absorptive properties, in the form of the absorption and spontaneous emission of photons by the atom, otherwise known as scattering. The dipole force and scattering force are therefore fundamentally linked processes. The scattering rate is related to the imaginary

part of the complex polarisability by

$$R_{\text{scatt}}(\mathbf{r}) = \frac{1}{\hbar\epsilon_0 c}\text{Im}(\alpha) I(\mathbf{r}). \tag{3.28}$$

This is equivalent to the scattering rate derived via the optical Bloch equations, given by equation 3.23.

The dipole force exerted on the atom is given by the gradient of the interaction potential,

$$\mathbf{F}_{\text{dip}}(\mathbf{r}) = -\nabla U_{\text{dip}}(\mathbf{r}) = \frac{1}{2\epsilon_0 c}\text{Re}(\alpha)\nabla I(\mathbf{r}). \tag{3.29}$$

We can see from this equation that the force experienced by an atom within the beam is dependent on the intensity gradient of the light field. The complex polarisability α can be calculated using a semiclassical approach by treating the atom as a quantum two-level system which interacts with a classically-treated electromagnetic radiation field, as done in section 3.1. Following the method outlined in [84], the dipole potential U_{dip} can then be expressed as

$$U_{\text{dip}}(\mathbf{r}) = \frac{3\pi c^2}{2\omega_{21}^3}\frac{\Gamma}{\Delta}I(\mathbf{r}) \tag{3.30}$$

and the scattering rate as

$$R_{\text{scatt}}(\mathbf{r}) = \frac{3\pi c^2}{2\hbar\omega_{21}^3}\left(\frac{\Gamma}{\Delta}\right)^2 I(\mathbf{r}) \tag{3.31}$$

where Γ is the spontaneous decay rate of the excited atomic level and $\Delta = \omega - \omega_{21}$ is the detuning of the driving laser frequency ω from the resonant transition frequency ω_{21}.

A laser beam normally has a Gaussian intensity profile in the xy plane perpendicular to the propagation axis z, with maximum intensity along this axis. By focussing a laser beam to a narrow waist, using a lens for example, the intensity of the beam can be made to vary along the propagation axis as well. The resulting intensity distribution of the beam is given by [84]

$$I(r,z) = \frac{2P}{\pi w^2(z)} \exp\left(-\frac{2r^2}{w^2(z)}\right), \tag{3.32}$$

where r is the radial coordinate in the xy plane, P is the power propagating along z and $w(z)$ is the beam radius extending to $1/e^2$ of the intensity at $r = 0$.

For a red-detuned laser, the frequency detuning $\Delta = \omega - \omega_{21}$ is negative, and the resulting dipole potential U is therefore also negative as can be seen from equation 3.30 and has a minimum at the point of maximum intensity I as $U \propto I/\Delta$ [49]. In this case the dipole force acts to push atoms towards the point of maximum intensity in all three dimensions, providing a restoring force towards the centre of the beam waist, as demonstrated schematically in Figure 3.6. In order to maximise the effectiveness of the trap, a high intensity is needed to increase the trap depth and produce a stronger dipole force, as the dipole potential U scales with I. A large detuning Δ from the resonant frequency is also preferable in order to minimise absorption and spontaneous emission from the excited state [84], reducing heating of the atoms by incident radiation which may eject them from the trap. This is because the scattering rate corresponding to the rate of spontaneous emission scales with Δ^{-2}, as can be seen in equation 3.31, whereas the dipole potential only scales with Δ^{-1} as shown in equation 3.30, so there is a greater decrease in scattering rate with

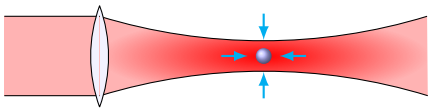

Figure 3.6: Simple diagram of the dipole trapping technique. A far red-detuned laser is focussed to a tight waist by a lens. There is an intensity maximum at the centre of the beam waist. The dipole force acts to push atoms from all directions towards the point of maximum intensity, trapping them at the centre of the waist.

increased detuning compared to the decrease in dipole potential. A dipole trap normally has a much greater detuning from resonance than that used in laser cooling, being around a million times larger, in the range of THz. Because of this, the dipole trap is also known as a Far-Off Resonance Trap (FORT). The dipole trap has been successfully implemented in the laboratory to confine small numbers of atoms and measurements were taken to characterise their physical properties, as discussed in chapter 5.

3.4 Summary

In this chapter, the theoretical background of atom trapping techniques using lasers has been presented. Lasers are capable of interacting strongly with atoms, giving rise to absorptive and dispersive effects. A derivation of the optical Bloch equations was given in section 3.1, leading to an expression describing the rate of photon scattering by atoms.

The cyclic absorption and re-emission of radiation by atoms allows lasers to 'push' atoms in a specific direction. Combined with the Doppler effect, this leads to the powerful Doppler cooling technique, described in section 3.2.1. As a result of Doppler cooling, counter-propagating beams provide a frictional

force which cools atoms, known as optical molasses. Utilising oppositely circularly-polarised counter-propagating beams in three orthogonal axes within a non-uniform magnetic field allows atoms to be trapped at a crossing point of the beams, known as the magneto-optical trap. An additional process known as sub-Doppler cooling occurs as a result of the polarisation gradient formed by the counter-propagating beams, allowing the optical molasses to cool atoms below the Doppler cooling limit of 146 μK.

The dipole potential created by a powerful far-detuned laser is capable of trapping atoms by the dipole force, with a relatively low scattering rate due to the detuning. In the case of a red-detuned beam focussed by a lens, atoms are pushed towards the position of maximum intensity, allowing small numbers of atoms to be tightly confined in a very specific position. This is known as a dipole trap, described in section 3.3. The dipole trap must be loaded from a background MOT reservoir of atoms, as it is only capable of trapping atoms which have already been cooled.

In the following chapter, the practical implementation of the magneto-optical trap in the laboratory will be described. This includes the setup of the laser system, which involves frequency stabilisation and locking of the cooling laser in a master-slave configuration and the repump laser; as well as the construction of the ultra-high vacuum chamber required for the operation of the MOT, to minimise collisional losses with the background gas. Experimental measurements taken to characterise the physical properties of the trap including the number and density of atoms and temperature will also be presented and discussed.

Chapter 4

Implementation of Atom Trapping

This chapter contains a description of the experimental setup employed in the laboratory for cooling and confining atoms in a magneto-optical trap (MOT), described in section 3.2.3. This requires a complex laser system to provide the cooling and repump beams for the MOT, including frequency stabilisation of the lasers by saturated absorption spectroscopy, and externally controlled frequency and intensity modulation using acousto-optic modulators. The trap is housed inside an ultra-high vacuum chamber, which is necessary to reduce collisions between the trapped atoms and the surrounding background vapour. A vacuum chamber was initially set up in the laboratory, but due to the presence of a leak which would have caused severe problems with the atom trapping experiments, it had to be dismantled and rebuilt, incorporating improvements to the design in the process. Therefore part of this chapter will be dedicated to describing the

work undertaken to detect the leak and to reconstruct the chamber.

It is useful to characterise the properties of the trap experimentally, as knowledge of characteristics such as density and temperature of the atoms is important for the study of the trap behaviour and for the design and choice of parameters used for the dipole trap. In the following section the laser system for the MOT is outlined, including a description of the frequency stabilisation method. In section 4.2, details of the testing, redesign and construction of the vacuum chamber are presented. Finally in section 4.3, experimental measurements for the characterisation of the MOT properties including the atom number, lifetime, size, density and temperature are described, along with a discussion of the results.

4.1 Cooling and Repump Laser System

In this section, the experimental setup employed for the atom trapping techniques outlined in section 3.2 is described. As discussed previously, the atomic species used for experiments in this work is rubidium, due to the fact that alkali metals contain only a single outer valence electron, so their behaviour is relatively simple and well understood in theory. In addition to this, the atomic transitions can be driven by cheaply-produced commercial laser diode wavelengths in the near-infrared (NIR). The isotope rubidium-87 is primarily used in this work instead of rubidium-85, due to the greater spacing between transition frequencies to the D_2 hyperfine levels [42, 43] as shown in Figure 2.4, allowing transitions to be more easily resolvable in the saturated absorption spectrum for frequency locking. However, it is straightforward to adjust the setup for the trapping of

rubidium-85 as well.

4.1.1 Laser sources and transitions

Commercially available free-running laser diodes have typical output powers of up to 100 mW. These laser diodes have a broad frequency linewidth operating at many different frequency modes, so they do not meet the requirement of a single frequency source for the excitation of atomic transitions. It is necessary to achieve a laser linewidth narrower than the natural linewidth $\Gamma \sim 6 \times 2\pi$ MHz of the cooling transitions in rubidium, so that a specific transition can be driven without interference with different transitions nearby in frequency; in other words, the transition probability to other levels must be small. The linewidth is narrowed by the use of an external cavity with a diffraction grating at one end, with a tuneable cavity length and grating angle by the use of piezo-electric transducers (PZTs). The grating ensures that only the zero-order undiffracted beam is reflected as an output for the laser, and the first-order diffracted beam is reflected back inside the diode, forcing it to oscillate only at the frequency of this mode, thus reducing the linewidth. Tuning the cavity length allows the output wavelength to be changed. This system of a laser diode with a linewidth-narrowing cavity is known as an extended-cavity diode laser (ECDL) and is widely used in atomic physics experiments.

The ^{87}Rb atomic transition used for the laser cooling cycle is $5^2S_{1/2}\ F = 2 \rightarrow 5^2P_{3/2}\ F = 3$, and the ECDL used for driving this transition is known as the cooling laser. As explained briefly in section 3.2.1, in practice rubidium atoms do not behave as a simple closed two-level system as assumed for much of the

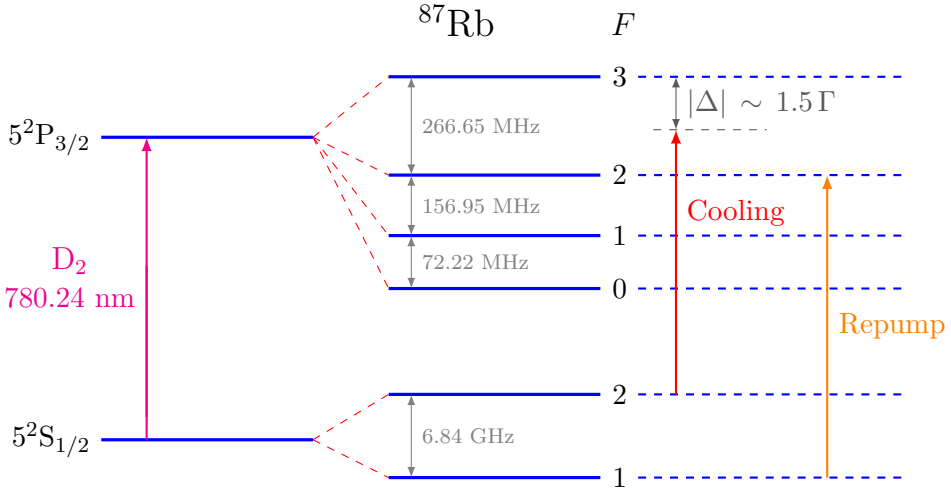

Figure 4.1: Representation of the energy level structure of the D_2 line of ^{87}Rb, with the magneto-optical trap (MOT) cooling and repump atomic transitions highlighted. The repump excitation is used to return atoms which spontaneously decay to the ground $F = 1$ state back into the cooling cycle. For general operation of the MOT, the cooling beams are detuned from the $5^2S_{1/2}$ $F = 2 \rightarrow 5^2P_{3/2}$ $F = 3$ transition by roughly 1.5 times the decay rate $\Gamma = 6.0666 \times 2\pi$ MHz [43].

theoretical treatment of atom-light interaction and laser cooling, and it is possible for the atoms to be excited to the $5^2P_{3/2}$ $F = 2$ state and subsequently decay to $5^2S_{1/2}$ $F = 1$. Therefore a second laser known as the repump laser is required to drive the $5^2S_{1/2}$ $F = 1 \rightarrow 5^2P_{3/2}$ $F = 2$ transition and return the atoms to the cooling cycle. The cooling and repump transitions are displayed schematically in Figure 4.1 with reference to the energy level structure of ^{87}Rb. The cooling and repump lasers are provided by ECDLs using a Sanyo DL-7140-201 commercial diode with the extended cavity designed and built by the Open University workshop. These lasers produce a wavelength between 775 and 800 nm [85] and an output power of up to a few tens of mW. The reduced linewidth of these lasers is typically a few hundreds of kHz [83].

4.1.2 Frequency locking

The laser frequency tends to be unstable and drifts due to small changes in the environment of the cavity, such as temperature and acoustic vibrations, so a frequency locking system is required. The locking technique used for these lasers is frequency locking by saturated absorption spectroscopy (SAS). To provide sufficient power for the cooling, we use a master-slave configuration. The light from the master laser is injected into a slave laser to obtain greater beam power while forcing this laser to oscillate at the same single frequency. This is known as injection locking. As can be seen from equation 3.26, the scattering force used to trap atoms in the MOT is greater for higher beam intensities I at the trap position, so it is beneficial to use as much cooling beam power as is available. In the system described here, an intensity of approximately 0.2 $\mathrm{mW\,mm^{-2}}$ per beam at the trap position is suitable, and is achieved using the master-slave configuration. The laser system and layout of the optics used for the MOT cooling and repump lasers is displayed in Figure 4.2.

The saturated absorption spectroscopy technique used to create the locking signal involves sending the laser through a glass cell of rubidium vapour and detecting the output light on a photodiode. The frequency of the laser can be scanned over a range of GHz by external electronics controlling the PZTs in order to see the frequency-dependent absorption peaks, in the form of a decrease in laser intensity due to the light being absorbed by resonant transitions in the rubidium atoms. Normally, the absorption peaks are Doppler-broadened by the Maxwell-Boltzmann velocity distribution of the Rb atoms, giving a Gaussian linewidth of a few hundred MHz. This broadening arises from the fact that

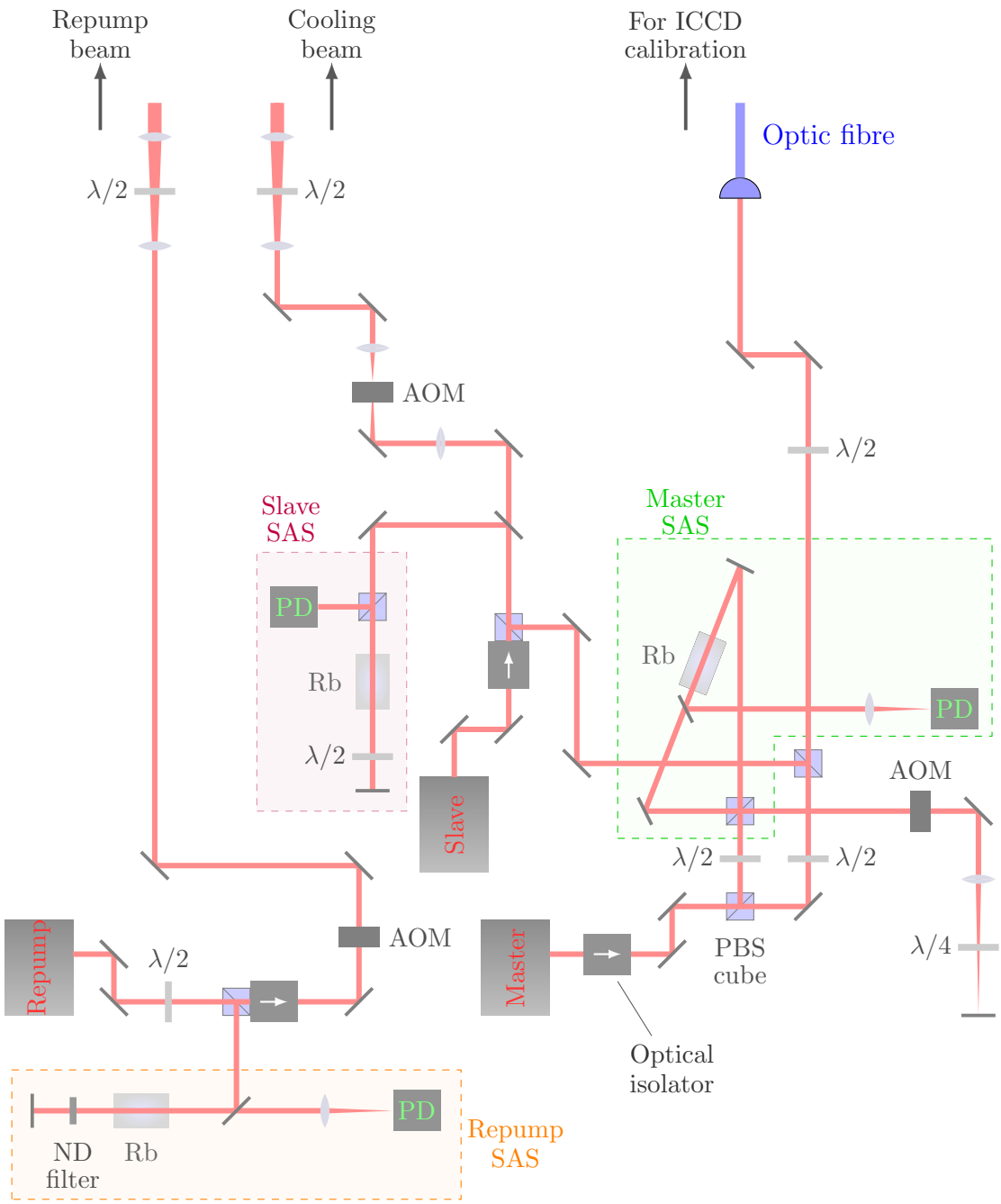

Figure 4.2: Schematic showing the MOT cooling and repump laser system, including frequency locking by saturated absorption spectroscopy (SAS). For the master and repump lasers, the saturated absorption signal is collected by a photodiode (PD) and used to produce an error signal for locking electronically. The SAS system for the slave laser is used only to monitor the spectrum. The master laser is passed through a double-pass AOM to control the cooling beam detuning, and the slave and repump lasers are passed through single-pass AOMs for controllable switching of the beams.

atoms travelling at a range of velocities experience a Doppler-shifted frequency when irradiated with laser light. This causes some absorption of the beam even if it is off resonance for stationary atoms, as the beam is shifted into resonance for atoms moving at a certain velocity. Doppler-broadening makes the hyperfine transitions indistinguishable, as they are typically separated by up to a hundred MHz. Therefore sub-Doppler features are produced by first sending a high power beam known as the pump beam through the Rb cell, exciting Rb atoms away from the ground state. A weaker counter-propagating beam called the probe beam is then sent through the cell and detected by the photodiode, and as the ground state population of Rb has been decreased, greater transmission can be seen at the resonant hyperfine transition frequencies in the probe beam absorption profile [86]. As the pump and probe photons are travelling in opposite directions, the only velocity group of atoms which interact with both beams simultaneously to allow transmission of the probe beam are the stationary atoms. By reducing the velocity distribution in this way, Doppler-broadening can be eliminated and narrow absorption features can be resolved. The resulting absorption spectrum can be seen in Figure 4.3, showing narrow naturally broadened transition peaks. An error signal is produced by the external electronics, in the form of the derivative of this signal, giving zero-crossing dispersion features at the transition frequencies. A negative feedback loop can then be used to lock the laser to the correct transition frequency. The cooling laser system is locked to the $5^2S_{1/2}\ F = 2 \rightarrow 5^2P_{3/2}\ F = 1, 3$ crossover peak and the repump laser is locked to the $5^2S_{1/2}\ F = 1 \rightarrow 5^2P_{3/2}\ F = 1, 2$ crossover peak of ^{87}Rb.

In addition to frequency locking, the beams are passed through acousto-optic

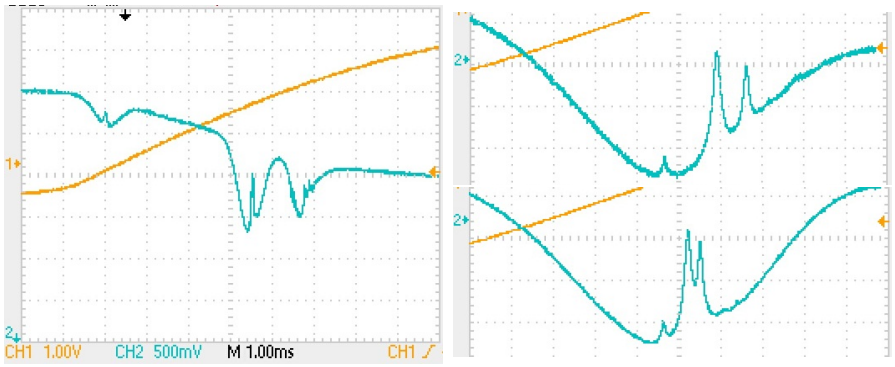

(a) (b)

Figure 4.3: Saturated absorption spectrum of rubidium. The general absorption structure can be seen in (a), showing Doppler-broadened absorption features. The two large peaks on the right correspond to the D_2 line transitions from the ^{85}Rb $F = 3$ ground hyperfine level (middle peak) and from the ^{87}Rb $F = 2$ ground hyperfine level (right peak). In (b), sub-Doppler features are seen in the ^{87}Rb (top) and ^{85}Rb (bottom) absorption peaks, showing individually resolved transition frequencies.

modulators (AOMs) which can be used to alter the laser frequency and attenuation[1]. The AOMs are controlled externally by Labview software and can be used to control the intensity and detuning of the beams from the Rb cooling and repump transitions. The master laser is passed through an AOM in double-pass configuration, in which the output beam is reflected back through the AOM, gaining twice the original shift in frequency. The benefit of this configuration is that it prevents tuning of the frequency from altering the alignment of the beam, at the cost of some power as the beam undergoes twice the optical losses associated with transmission through the AOM. This AOM is used to shift the frequency of the pump beam in the SAS frequency locking system for the master laser, which effectively allows the laser to be locked at a

[1]An AOM operates by applying a vibration to a crystal medium using a driven PZT. This diffracts the transmitted light into several orders at different frequencies, which can be tuned by the voltage applied to the PZT, so the desired output frequency beam can be selected.

controllable frequency offset from the cooling transition. The unshifted beam is used for injection locking of the slave laser, the output of which is used as the cooling beams for the MOT. This double-pass AOM system is used to control the detuning of the cooling beams from resonance. The repump laser is frequency locked by saturated absorption, and the slave laser also has a saturated absorption setup for the sole purpose of checking the fidelity of the spectrum induced by the injected master, as frequency stabilisation of this laser is done by locking the master laser. The slave and repump lasers each pass through a single-pass AOM which is used for the externally controlled switching of the beams during experimental sequences. The layout of the saturated absorption locking systems and AOMs can be seen in Figure 4.2.

Following this, the cooling and repump beams are then combined and divided into three pairs of counter propagating beams for the MOT by optical elements. Finally, a pair of anti-Helmholtz coils attached to the outside of the main chamber are driven by a current to produce the non-uniform magnetic field required for the MOT to operate. Three pairs of Helmholtz coils are also used to produce a static uniform field to correct for any stray background fields which may interfere with the trap. The magnetic field strengths produced by these coils can be tuned depending on the current applied to the coils, which is controlled externally by Labview software. Typical magnetic field gradients produced by the anti-Helmholtz coils for our experiments are in the range of $10 \rightarrow 15\ \mathrm{G\,cm^{-1}}$ near the centre of the MOT position. The Labview program is capable of running experimental sequences controlling experimental parameters such as the frequency shift and attenuation of each of the AOMs and the trapping field coil

current for switching on and off the magneto-optical trap, as well as triggering cameras used for the acquisition of fluorescence emitted from the trap to obtain experimental data. The timing of the steps in the experimental sequence may be controlled down to the 10 μs timescale.

4.2 Vacuum System

A vital component of the apparatus for the experimental implementation of atom trapping techniques is the vacuum chamber in which the trapped atoms are housed. As will be discussed further in this section, a vacuum is required to reduce collisions between the trapped atoms and the surrounding vapour. At the beginning of the work undertaken in this project, there was an existing vacuum chamber in the laboratory in which a magneto-optical trap was successfully achieved. However, a leak in the chamber was detected which introduced difficulties in the effective operation of the trap. Therefore the chamber was dismantled and subsequently rebuilt to remove the problem. This was a lengthy process which involved a cleaning and baking procedure, during which improvements to the design of the chamber were implemented. This section includes a basic explanation for why a vacuum chamber is essential for atom trapping experiments, followed by an investigation of the original vacuum chamber and subsequent redesign and building of the new chamber.

As described in section 3.2.3, the magneto-optical trap cools and traps atoms that enter the trapping volume, being the volume at which the six counter-propagating trapping beams overlap, down to temperatures on the order of 1 mK. In a realistic

situation, there is a background atomic vapour surrounding the MOT which remains at room temperature, $\sim$ 300 K[2]. Collisions between these background atoms and those in the MOT can easily transfer enough energy to eject atoms from the MOT. For this reason the loading dynamics of the MOT depend heavily on the background vapour pressure.

The number of atoms in the trap N at time t can be described by the rate equation

$$\frac{dN(t)}{dt} = R - \gamma N(t), \tag{4.1}$$

where R is the loading rate of atoms into the MOT from background rubidium vapour and γ is the loss rate of atoms from the trap due to collisions with the background vapour, in units of s^{-1}. The loss rate γ can be separated into a sum of two loss rates; the loss rate from collisions with background rubidium, γ_{Rb}, and from collisions with background non-rubidium, γ_{bg}. Therefore equation 4.1 can be expressed as [87–90]

$$\frac{dN(t)}{dt} = R - (\gamma_{\mathrm{Rb}} + \gamma_{\mathrm{bg}})\, N(t). \tag{4.2}$$

The loading rate R and loss rate γ_{Rb} are each directly proportional to the partial pressure of rubidium in the chamber, P_{Rb}, and the loss rate γ_{bg} is proportional to the partial pressure of non-rubidium, P_{bg}. This equation contains both loading and loss terms, which may lead to an equilibrium number of atoms being reached

[2]The atoms contained within the trap are able to remain at such a low temperature compared to the surrounding vapour without reaching thermal equilibrium because their temperature is a result of atom-light interaction with the lasers (within a highly localised volume at the point where the beams overlap), rather than from collisional interactions with other atoms.

in the trap, N_{eq}. The $1/e$ loading time τ is the time taken for $(1 - 1/e)N_{\text{eq}}$ atoms to be trapped when switching on the trap and initiating loading from the background vapour. The solution to equation 4.2 can be expressed in terms of N_{eq} and τ as

$$N(t) \;=\; N_{\text{eq}} \left(1 - e^{t/\tau}\right). \tag{4.3}$$

It can be seen from equation 4.3 that the loading dynamics of the MOT can be characterised entirely using the two measurable parameters N_{eq} and τ. These can be expressed in terms of the loading and loss rate parameters R, γ_{Rb} and γ_{bg} as

$$N_{\text{eq}}(\tau) = \frac{R}{\gamma_{\text{Rb}}} (1 - \gamma_{\text{bg}}\tau) \tag{4.4}$$

and

$$\tau = \frac{1}{\gamma} \;=\; \frac{1}{\gamma_{\text{Rb}} + \gamma_{\text{bg}}}. \tag{4.5}$$

Due to the losses as a result of collisions with background vapour, a very low background pressure of $\lesssim 10^{-9}$ mbar is required in order to effectively load appropriate numbers of atoms into the trap [91]. This can be seen from equations 4.4 and 4.5, as the greater the loss rates γ_{Rb} and γ_{bg} due to collisions with background vapour, the shorter the lifetime of atoms in the trap τ and the smaller the equilibrium number of atoms reached, N_{eq}. In [91] it is shown that the trap lifetime is inversely proportional to the total background vapour pressure, while being relatively insensitive to the trap depth. It is also calculated that pressures of $\lesssim 10^{-9}$ mbar are required to produce trap lifetimes on the order of seconds or longer, allowing useful numbers of atoms to be trapped for a wide range of experimental applications. Therefore atom trapping experiments are

universally carried out in ultra-high vacuum (UHV) chambers. The background vapour pressure also has a significant effect on the loading dynamics of the optical dipole trap, which is discussed further in section 5.2.4. This is important in the wider context of this work, in which the goal is to produce a dipole trap with appropriate physical characteristics for application as a qubit. In order to produce a lifetime on the order of seconds for dipole-trapped atoms, allowing negligible collisional losses during the timescales of quantum information processes, we aimed to produce a final background pressure in the chamber of below 10^{-9} mbar.

An UHV chamber typically requires several stages of pumping to achieve the intended final pressure. The first stage is the use of a backing pump, such as a piston, rotary or scroll pump, the purpose of which is to initially reduce the pressure in the chamber from atmospheric pressure of $\sim 10^{3}$ mbar down to roughly $\sim 10^{-1} - 10^{-3}$ mbar, at which point a turbo pump can be operated. A turbo pump can then be used in conjunction with 'baking' of the chamber, in which the chamber is heated uniformly using either an oven or heating tapes to speed up the outgassing and removal of water vapour and hydrogen from the chamber, to achieve the intended final pressure of $\sim 10^{-9} - 10^{-10}$ mbar. Finally an ion or diffusion pump can be used to maintain this final pressure long-term during the day-to-day experimental work or achieve even lower pressures.

To ensure that a low enough final pressure is reached, the chamber must be made of low outgassing materials such as stainless steel [92]. All metals and alloys are outgassing to some extent, which means they continually release gases embedded in the material such as hydrogen. Higher outgassing materials like aluminium and zinc outgas at too high a rate, making UHV unachievable. It is also beneficial

to minimise the volume and surface area inside the chamber, so that a smaller volume of gas needs to be initially pumped out and there is less surface to outgas from. One of the frequent problems which can prevent the vacuum reaching an appropriately low pressure is the presence of oil, which is extremely difficult to remove from inside the chamber, even with baking, and may enter the chamber by backstreaming from an oil-lubricated backing pump such as a rotary or piston pump. For this work, this problem was solved by using only dry (oil-free) backing pumps. Any dust or fingerprints on the vacuum chamber components during assembly can also be highly detrimental to the vacuum pressure, so an extensive cleaning process is carried out on every component during construction, described in section 4.2.2. The following section details experiments carried out to test the original vacuum chamber. It was ultimately concluded that a redesign and reconstruction of the chamber was required, due to the discovery of a leak in the chamber resulting in a poor quality vacuum.

4.2.1 Troubleshooting the vacuum chamber

The original vacuum chamber containing the MOT was made of stainless steel with anti-reflection coated fused silica viewports to allow the lasers to enter. The anti-Helmholtz and Helmholtz coils used to produce and control the trapping magnetic field for the MOT were mounted on the outside of the chamber. The main chamber body can be seen in Figure 4.4. The chamber was connected to a Varian VacIon Plus 20 StarCell ion pump which is capable of maintaining UHV pressure in the system. The MOT could be imaged in real-time by infrared cameras outside the system, allowing alignment of the MOT beams and

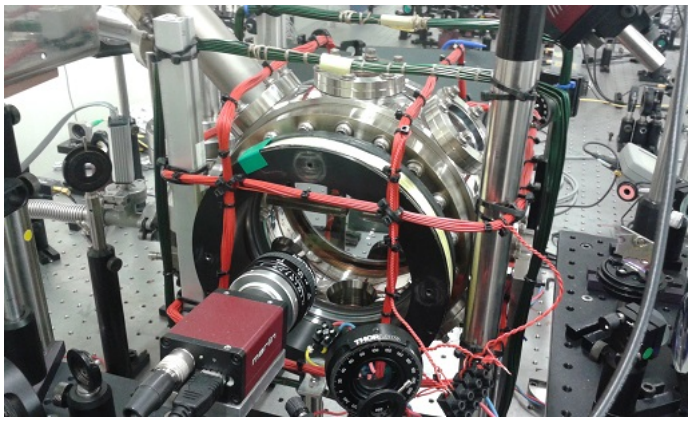

Figure 4.4: Photograph of the main body of the original vacuum chamber. The Marlin F033B camera used for imaging of the MOT fluorescence can be seen in front of one of the anti-reflection coated viewports. The yellow wire coils wrapped around the large black mounts are the anti-Helmholtz coils used for trapping the MOT, and the red and green coils are the Helmholtz coils used for fine-tuning the centre position of the non-uniform AH field. A connection leading to the ion pump can be seen on the upper-left.

adjustment of the magnetic field to be made. An image of the MOT captured by an infrared camera is shown in Figure 4.5. The source of rubidium in the chamber was provided by solid rubidium metal in a glass cell attached to the main chamber with a valve allowing the passage of vapour between the Rb source and main chamber to be opened or closed. Applying a current to a coil of wire wrapped around the cell caused the Rb to be heated, greatly increasing the rate of evaporation and thus injecting rubidium vapour into the chamber.

It was observed qualitatively that the fluorescence from the MOT was becoming weaker and would diminish greatly in a short amount of time (minutes) after closing the valve to the rubidium source. This suggested that either the rubidium was quickly becoming stuck to the walls of the chamber, leading to a rapidly decreasing amount of rubidium in the centre of the chamber from which fluorescence could be observed, or that rubidium atoms were rapidly being ejected

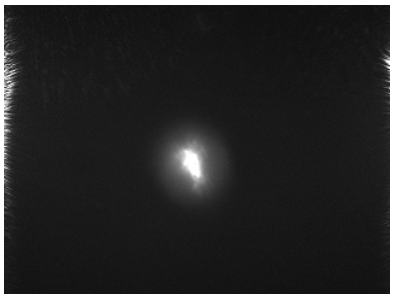

Figure 4.5: Infrared camera image of the MOT from our vacuum chamber. Fluorescence detected from the cloud of atoms trapped at the MOT centre can be seen.

from the MOT by collisions with foreign gaseous species inside the chamber. This can happen if the background (non-Rb) pressure inside the chamber is too high, which occurs for pressures around 10^{-9} mbar or higher.

The background non-Rb pressure inside the chamber can be measured by characterising the MOT by taking pressure rise measurements [88, 89], following the method from [88]. This involves measuring MOT loading curves, which refers to the measurement of the number of atoms in the MOT with loading time while the magnetic field of the trap is switched on, allowing atoms to gather in the trap. By comparing this data with equation 4.3, the equilibrium number of atoms N_{eq} and loading time τ can be deduced for that particular loading curve. The trapping and loss rate parameters R/γ_{Rb} and γ_{bg} can also be obtained by measuring the dependence of N_{eq} on τ and comparing this relation with equation 4.4. This can be done by obtaining a range of loading curves with a different N_{eq}, for example by changing the amount of background rubidium, causing P_{Rb} to vary between loading curves. The partial pressure of rubidium P_{Rb} can then be calculated using equation 4.5 and the relation $\gamma_{\text{Rb}}/P_{\text{Rb}} = 4.4 \times 10^7\ \text{Torr}^{-1}\,\text{s}^{-1}$ from [88,89] to obtain R/P_{Rb}. The partial pressure of non-rubidium P_{bg} can be calculated

using our obtained value of γ_{bg} and the relation $\gamma_{\text{bg}}/P_{\text{bg}} = 4.9 \times 10^7$ Torr^{-1} s^{-1} from [88, 89], assuming the background non-Rb gas is primarily hydrogen[3]. Too high a partial pressure of non-Rb would indicate a leak in the chamber, and too low a partial pressure of Rb would suggest that the Rb is becoming stuck somewhere on the chamber walls and not making it to the trap.

The number of atoms in the MOT can be measured by detecting the fluorescence emitted by the Rb atoms in the MOT using some imaging apparatus such as a photodiode. Due to the limited optical access of our system, it was difficult to position a photodiode or focussing lens close enough to the MOT to acquire an appreciable fraction of the fluorescence, or to distinguish the low level of MOT fluorescence from other sources of stray light such as from slight reflections of the lasers from inside the chamber or from the room lights. Instead, an infrared-sensitive camera from Allied Vision Technologies, as used to capture the image in Figure 4.5, was used. This camera did not have to be placed so close to the chamber to obtain a suitable amount of fluorescence, and was instead positioned roughly $15 - 20$ cm from one of the large glass viewports of the main chamber body, in between the two incoming horizontal MOT beams. This camera records a series of images to the computer at a rate of 12.3 s^{-1}. A measure of the fluorescence is obtained from each image by summing all the pixel counts in the image, returning the integrated camera signal. We denote this quantity as S, and assume that $S = kN$, where k is a constant. This allowed us to carry out the method described above, in which the MOT lifetime τ is obtained for a range of

[3]The assumption that the background non-rubidium vapour is mostly comprised of hydrogen is justified, as following the baking and pump down of the chamber, the contained gas is dominated by the hydrogen molecules which are gradually outgassed from the stainless steel comprising the vast majority of the surfaces inside the chamber.

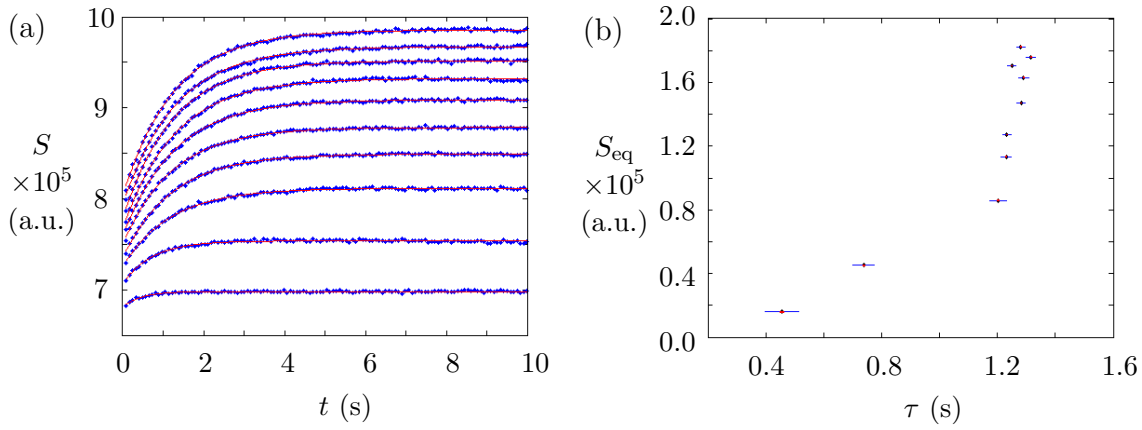

Figure 4.6: Experimental data for the MOT loading curves taken for characterisation of the MOT. In (a), non-background corrected loading curves of integrated camera signal S are given against time t at ten different time intervals after closing off the Rb source (0, 10, 20, 30, 40, 55, 70, 100, 130 and 190 minutes). In (b) the background-corrected equilibrium integrated signal S_{eq} is plotted against the MOT lifetime τ, with horizontal error bars.

different equilibrium numbers of atoms N_{eq} by measuring loading curves, leading to a measurement of the partial pressure of the background vapour. Following this method, loading curves were measured at a number of time intervals after injecting rubidium vapour into the chamber and closing the valve to the rubidium source, allowing the amount of rubidium inside the chamber to fall over time. Each curve was averaged from roughly six trials taken within the space of one minute. The results are displayed in Figure 4.6 (a), showing a steadily decreasing equilibrium number of atoms reached N_{eq} between loading curves.

Following the loading curve measurements, the data was background-corrected by subtracting an averaged integrated signal value acquired for a few seconds before the start of loading. The equilibrium integrated camera signal S_{eq} and MOT lifetime τ for each loading curve were then extracted from the data by

fitting equation 4.3 to each background-corrected curve. The results are plotted in Figure 4.6 (b) in the form of an $N_{\text{eq}} - \tau$ plot, showing a decrease in MOT lifetime as the rubidium level falls. These results are in contrast to those obtained by [88] using the same method with no significant leaks in the chamber, which show the opposite relation, a linear increase in lifetime as the rubidium level falls. This is shown in Figure 2 in [88]. This figure displays the expected behaviour of the trap lifetime with respect to the equilibrium number of atoms, as shown in equation 4.4, which suggests a negative linear relationship between N_{eq} and τ with a gradient given by $-R\gamma_{\text{bg}}/\gamma_{\text{Rb}}$ and y-axis intercept given by R/γ_{Rb}. Instead, the results presented in this work display a similar relationship to those obtained in a slightly different experiment, shown in Figure 3 in [88], in which background non-rubidium had been allowed to build up inside the chamber by switching off the vacuum ion pump at the start of the experiment, to simulate a leak in the chamber. In this case, the background non-rubidium partial pressure P_{bg} increases with time throughout the duration of the experiment, which for both this work and [88] is $3 - 4$ hours. Therefore it can be seen from equation 4.5 that the lifetime τ decreases with time, as N_{eq} is also decreasing with time. This leads to the opposite relationship with a positive gradient between N_{eq} and τ being observed when non-Rb is allowed to increase in the chamber. As this relationship was observed in the results from our experiment even while the ion pump was running, this suggested that the level of background non-Rb vapour was increasing in our chamber, leading to the conclusion that there was a source of non-Rb in our chamber such as a leak. Due to a lack of knowledge of the translation factor k between the integrated pixel counts on the camera and the number of atoms in the MOT, the exact values of the number of atoms in the

MOT as well as the loss rate γ and partial pressure of non-rubidium P_{Rb} are not presented here; however, the observed relationship between N_{eq} and τ is the real information of value obtained from this experiment and provides enough evidence to support the conclusion.

In order to check the system for leaks, a residual gas analyser (RGA) was attached to the system. This is a quadrupole mass spectrometer capable of measuring the partial pressures of different atomic and molecular species inside the chamber. This was utilised for leak-checking with helium in order to locate any leaks in the system. A needle connected to a helium supply was used to spray helium at various points around the chamber, and the results from the RGA were observed to check for an increase in helium partial pressure. One leak was found, around the edge of one of the vacuum chamber viewports used for the entry of the cooling lasers for the MOT. The leak was detected at four equally spaced points around the edge of the viewport, by measuring first the background partial pressure of helium followed by the maximum partial pressure reached after spraying. Three trials were taken for each position, and the averaged results are displayed in Figure 4.7 (a), showing a clear increase in partial pressure. Upon dismantling the chamber, damage was found around the edge of this viewport as shown in Figure 4.7 (b). From these observations it was concluded that non-rubidium background gas was capable of entering the chamber through the leak in the viewport, causing the deterioration of our vacuum and therefore a repaired or replacement viewport was necessary.

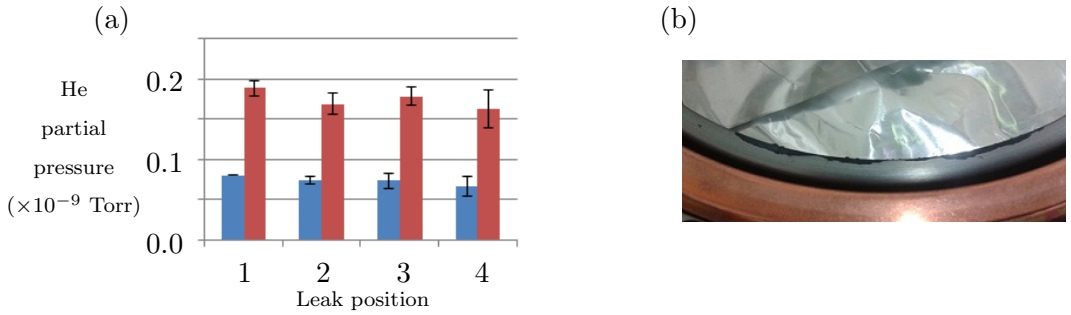

Figure 4.7: (a): Average partial pressure of helium inside the chamber detected by the residual gas analyser (RGA) before (blue) and after (red) spraying helium at four positions around the viewport edge. The error bars show the standard deviation. (b): Photograph of the viewport removed from the vacuum chamber, showing the damage caused to the glass-metal interface by the sealant residue where the leak was detected.

4.2.2 Redesign and rebuilding the vacuum chamber

Redesign of the chamber components

As a result of the discovery of a leak in the original vacuum chamber, replacement viewports were ordered. Aside from the viewports, it was planned for several other features to be updated upon reassembly. The original source of rubidium housed in a glass cell attached to the chamber was replaced by commercial rubidium dispensers inside the main chamber, which release rubidium vapour by a chemical reaction when a current is applied through an electrical feedthrough into the chamber. This would increase control over the amount of rubidium supplied to the trap, and also allow the rubidium to be dispensed from a location much closer to the trap than before, to help prevent the atoms from becoming stuck to the chamber walls along the route to the trap position. The support for the high-NA lenses for the dipole trap was also changed, with the new design offering greater stability and more precise trapping. This coincided with replacing

the high-NA lenses used for focussing the dipole trapping beam for those with a slightly larger diameter and focal length, and an indium tin oxide (ITO) coating to avoid the build up of stray charges on the lenses which could interfere with the energy level structure of highly sensitive Rydberg atoms.

I produced the new design of the lens support structure in collaboration with the engineering workshop at the Open University, for which I contributed my own requirements relating to the aim of this project. The new design of the support for the lenses is described in more detail in section 5.1.1, and was developed to achieve my goal of microscopic dipole trapping a sample of atoms within a single Rydberg blockade radius, as the lenses would allow focussing an input trapping beam to a waist of a few μm, with a trapping position precise and stable enough to establish a reliable imaging system. This imaging system is described in section 5.1.4, and involves acquiring fluorescence from the trap and focussing it onto an intensified CCD camera, from which measurements of the trapped atoms such as the number of atoms can be made. I also designed and placed a series of electrodes inside the chamber to give control over the electric field in the vicinity of the trapped atoms, for application in potential future experiments, for example including Rydberg atoms which are sensitive to electric fields. This was done with the planned eventual implementation of a Rydberg-based quantum gate in mind, as is required for the overarching goal of demonstrating quantum information processes between atomic qubits. A comparison of the basic design of the original vacuum chamber with the new design, including the changes to the rubidium source and the dipole trap lens holder structure, is shown in Figure 4.8.

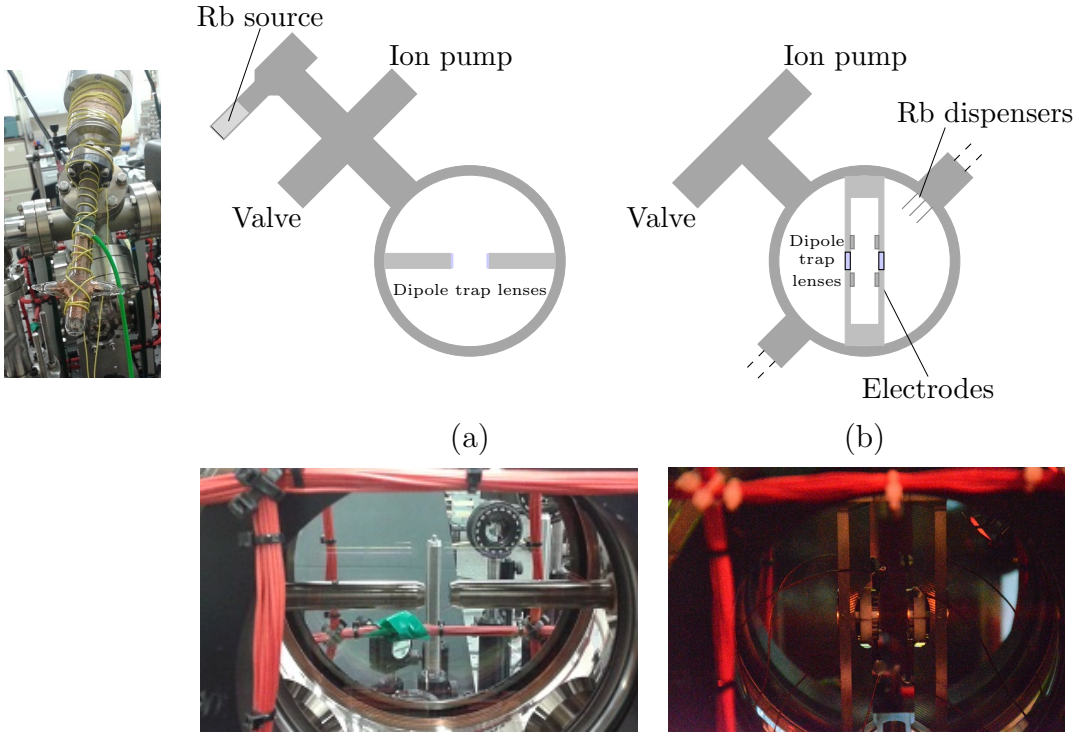

Figure 4.8: Comparison of the original vacuum chamber design (a) with the new improved design (b) featuring improvements to the rubidium source and dipole trap lens holders. The old solid rubidium source was replaced by commercial dispensers located closer to the MOT, and a more stable structure to house the dipole trap lenses was employed. Electrodes were also included in the new design, to compensate for stray electric fields which may disturb the energy levels of trapped rubidium atoms. A photograph of the old rubidium source is provided, as well as photographs of both the old and new dipole trap lens support structures.

Construction of the chamber

The rebuilding of the vacuum chamber required the chamber components to be cleaned to UHV standard and reassembled. The cleaning process was adapted from [50, 93]. All chamber components were handled with powder-free nitrile gloves to ensure they were not contaminated with fingerprints. The process involves cleaning each stainless steel chamber component in an ultrasonic bath, first using Decon90 detergent, followed by distilled water and finally methanol. After being cleaned and left to dry each component was wrapped in foil until the assembly of the chamber to prevent dust or other contamination from entering. During assembly, components were connected by flanges with ConFlat knife-edge seals using copper gaskets. Annealed copper gaskets were used to connect the glass viewports. Flanges were connected using silver bolts, which do not seize during baking, and a torque wrench was used to ensure a consistent torque was applied to the bolts around each flange. The electrodes mounted on the high-NA lens holding structure were connected to electrical feedthroughs using Kapton-insulated wires which are UHV-compatible and are not damaged by baking. The rubidium dispensers used were from SAES Getters and were spot-welded to electrical feedthroughs, allowing a set current sent from outside the chamber to dispense a controllable amount of rubidium inside.

After initially pumping the chamber down to high vacuum with the backing and turbo pumps, the chamber was baked to speed up the outgassing of the materials in the chamber and achieve the intended ultra-high vacuum pressure of $P \sim 10^{-10}$ mbar. During the process the pressure inside the chamber could be measured using an Ionivac ITR90 ion gauge from Oerlikon Leybold Vacuum

GmbH connected near the entrance to the turbo pump. As the pressure at this position is not fully representative of the pressure at the centre of the main chamber, and also due to the general inaccuracy of pressure gauges at very low pressures, this measurement was taken as a rough indication of the order of magnitude of the pressure in the main chamber. The final pressure reached after baking was expected to be below the lowest measurable value for this gauge, 5×10^{-10} mbar. For the heating, the chamber was wrapped with heating tapes in between several layers of conductive foil, to ensure that the heating was uniform and consistent over the surface of the chamber; it is important to do this in order to avoid damage to the chamber caused by uneven thermal expansion of the components. Numerous thermocouples were placed at various positions around the chamber to measure the temperature. A temperature regulation unit, designed and constructed with assistance from the Open University electronics workshop, was used to control the heating tapes by a feedback loop using the output from the thermocouples. The positions used for the temperature measurements were on the main chamber body, denoted as (T_1), on one of the large viewports (T_2), the 5-way cross above the chamber (T_3) and the bellows leading to the turbo pump (T_4). In addition to this the temperature of one of the heating tapes was controlled and measured using a Eurotherm temperature controller (T_5).

The heating was gradually increased in stages over the course of a week, allowing time for the outgassed material to be pumped out of the chamber before increasing the temperature. A limit of $T = 150^{\circ}$C was set on the maximum temperature of the chamber, to prevent damage to the high-NA lenses and viewports. Following

this the temperature was reduced to room temperature gradually over two days, and the turbo and backing pumps were valved off along with the ion gauge, allowing the ion pump to take over. The evolution of the temperature and pressure of the chamber can be seen in Figure 4.9. In the absence of the ion gauge, the vacuum pressure can be measured roughly using the operating current of the ion pump, which has a strong dependence on the pressure. Before baking, this current-pressure dependence was characterised using the ion gauge to measure the pressure at varying ion pump current. Finally, after the baking process and allowing the ion pump to continue pumping over the course of two weeks, the final pressure achieved in the chamber was measured from the ion pump current of 1.1 μA, corresponding to a pressure below 5×10^{-10} mbar.

As explained earlier in this section, we were aiming to obtain a final background vapour pressure of below 10^{-9} mbar in order to achieve a MOT lifetime on the order of seconds, following the calculation of the dependence of lifetime on background pressure in [91]. This was done to ensure an appreciable number and density of atoms could be confined in the MOT, being the optimal environment to provide a reservoir of atoms for loading the optical dipole trap. Obtaining this low a background pressure would also reduce collisional losses in the dipole trap and ensure a dipole trap lifetime on the order of seconds, preventing losses during quantum information processing timescales and helping to enable the application of the dipole trap as a qubit. Therefore the vacuum chamber developed in this section was successful and the final pressure achieved of $< 5 \times 10^{-10}$ mbar was deemed suitable for our atom trapping experiments.

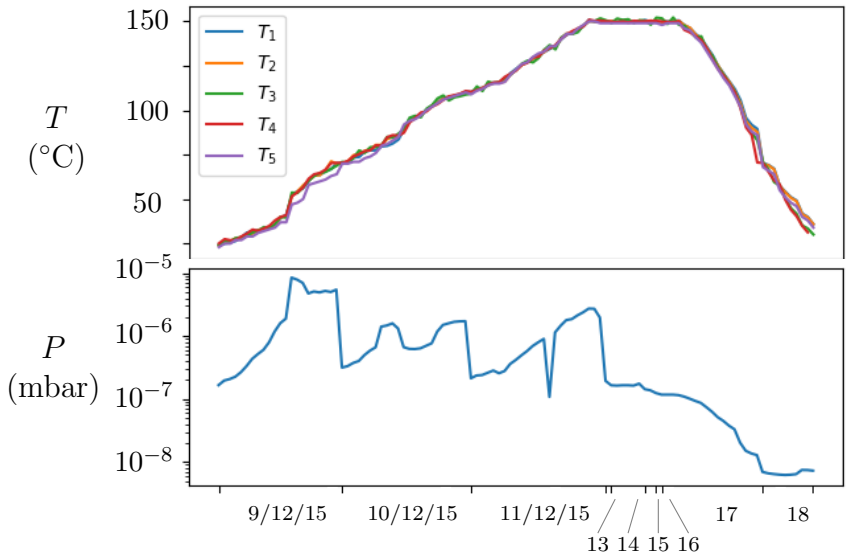

Figure 4.9: Evolution of the temperature at various positions around the vacuum chamber and the pressure inside the chamber during the 9-day baking process. Near the end of the process the valve to the turbo pump and ion gauge was closed, preventing further pressure measurements. The temperature was measured using separate thermocouples at five different positions, being the main chamber (T_1), one of the large viewports (T_2), the 5-way cross above the chamber (T_3), the bellows leading to the turbo pump (T_4) and the Eurotherm heating tape controller (T_5).

4.3 Magneto-Optical Trap

In order to load a magneto-optical trap with rubidium atoms inside the vacuum chamber, three pairs of orthogonal counter-propagating cooling beams combined with a non-uniform magnetic field produced by anti-Helmholtz coils is required, as explained in section 3.2.3. The cooling and repump beams, frequency locked to the laser cooling and repump transitions for ^{87}Rb respectively as described in section 4.1, are each passed through an acousto-optic modulator (AOM) in the single-pass configuration, using the first-order deflected beam as the output. This is used as a way to quickly switch the frequency or intensity of the beam, and can be remote-controlled as part of an experimental sequence. Due to the single-pass set up, changing the frequency with the AOM causes the deflection angle to change, misaligning the beam and effectively switching it off very quickly. Using this method we can achieve beam switching times on the order of nanoseconds.

Each beam then passes through a half-wave plate, and is then telescopically expanded to 2.5 mm in size using a pair of lenses. They are then overlapped and divided into two beams by sending each onto adjacent faces of a polarisation beam splitting (PBS) cube. The half-wave plates are used to adjust the polarisation of the beams before the cube such that 1/3 of the output power is output in one direction to be used as the vertical MOT beam, and 2/3 is output in the other direction, where it is further split equally by another PBS cube to create the two horizontal MOT beams. By the time these beams have reached the chamber after travelling $\sim$ 1 m from the expanding lenses, the typical power of each cooling beam is 2 mW and the beam diameter is 3.6 mm due to divergence following the lenses. This divergence was measured by imaging the cooling beams on an

infrared camera at four different positions along the beam path, and extracting the beam diameter by fitting a 2D Gaussian profile to the images. These were located between the second lens of the telescope used for expansion of the beam and after exiting the vacuum chamber. From these measurements it was deduced that, despite the beams effectively maintaining the same cross-sectional area over the length scale of the trap itself, after being retro-reflected back into the chamber to provide the counter-propagating beams this cross-sectional area had increased due to the divergence, resulting in a decrease in intensity by a factor of 1.3 ± 0.1 for one beam and 1.4 ± 0.1 for the other. This divergence of the beams is far from ideal as a balance in intensity between the incoming and retro-reflected beams is required for the MOT to function properly. However, as a MOT was obtained with this setup which was suitable for the work carried out in this thesis, the adjustment of the system for the correction of the divergence was not deemed to be a high priority at the time. The repump beams do not need to be as powerful, or perfectly balanced in all three directions, so their power is limited by the intensity modulation input of the AOM and kept at 0.86 mW for the vertical beam and 0.19 mW for the two horizontal beams.

The three MOT beams are aligned to pass through the middle of the dipole trap lenses in the centre of the vacuum chamber. Before entering the chamber they are passed through quarter-wave plates to become circularly polarised, as is required for the operation of the MOT. The angle between the two horizontal beams is confined to 49° by both the dipole trap lens holders and the vacuum chamber viewports, so they are not orthogonal as in the ideal case. In order to obtain the counter-propagating oppositely circularly-polarised beams, the MOT beams

are passed through another quarter wave plate on the other side of the chamber and retro-reflected by mirrors along the opposite path. It is assumed that the optical losses of the beams passing through the chamber viewport and quarter wave plate twice are negligible, so that all six MOT cooling beams have equal power. In reality the total loss in power for each beam induced by these elements is likely to be $\sim 5\%$.

The non-uniform magnetic field for the MOT is produced by a pair of coils in the anti-Helmholtz configuration mounted on the outside of the chamber. Each of these coils is formed of 100 turns of wire and has an inner diameter of 6 cm. The centre of each coil is approximately 6 cm from the MOT position. A typical current of 3.5 A is passed through the coils for standard continuous operation of the MOT, producing a magnetic field gradient of approximately $10 \rightarrow 15\,\mathrm{G\,cm^{-1}}$ near the centre of the trap position. The layout of the experimental apparatus for the production of the MOT, including the laser beam paths and optical elements, is displayed in Figure 4.10.

4.3.1 Characterisation of the MOT

To study the behaviour of the magneto-optical trap, measurements of physical properties including the number, density, and temperature of the trapped atoms were taken.

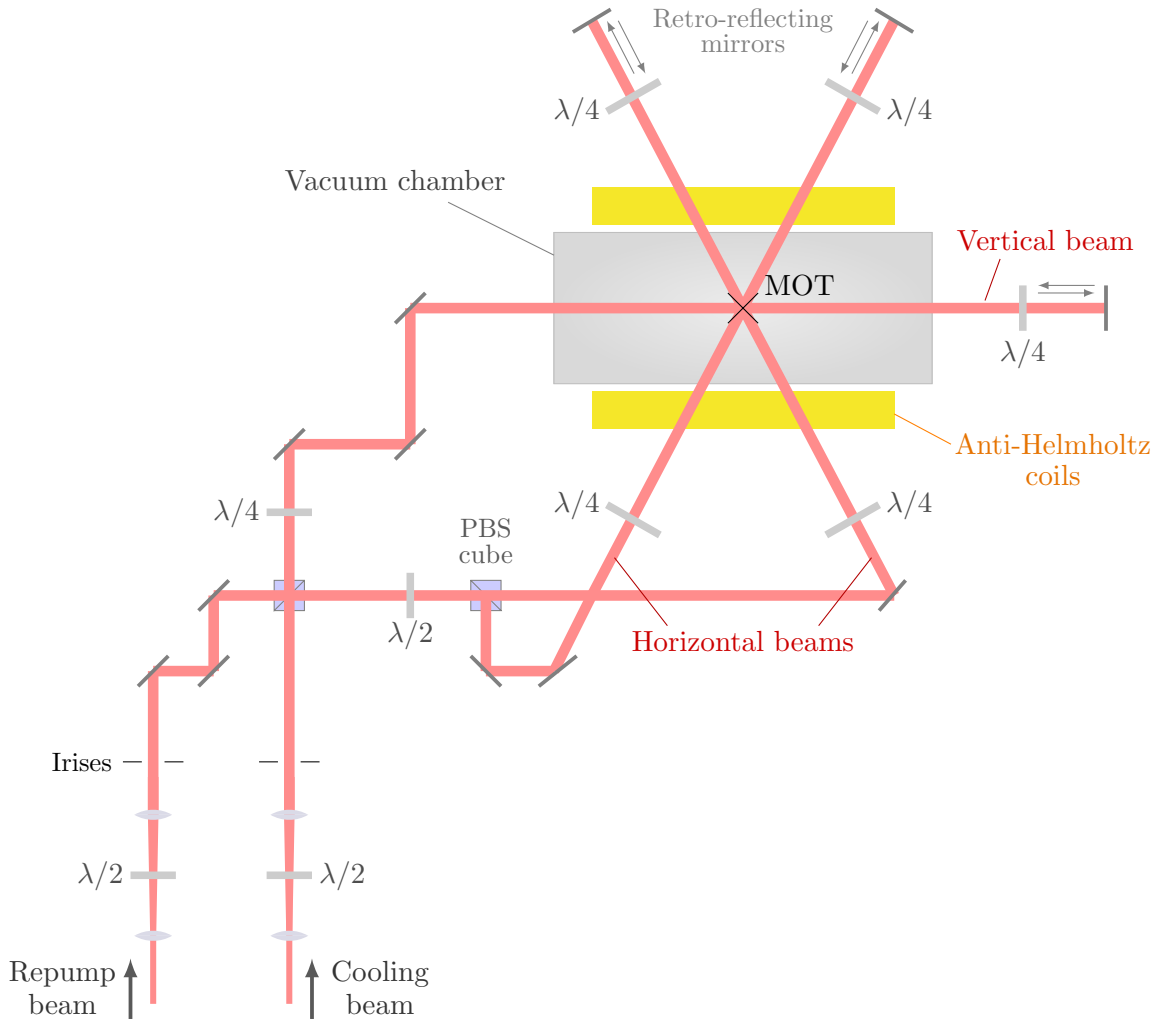

Figure 4.10: Schematic showing the laser beam path and layout of the optical elements for the implementation of the magneto-optical trap (MOT) inside the ultra-high vacuum (UHV) chamber. The cooling and repump beams are overlapped and divided into three beams of equal power using polarisation beam-splitting (PBS) cubes, then aligned to cross at the MOT position. After exiting the chamber the beams are retro-reflected to obtain the counter-propagating beams. In this diagram the path of the vertical beam is altered to allow a clear 2D representation.

Atom Number and Lifetime

There are various ways to determine the number of atoms comprising the MOT, N. This usually involves measuring the amount of fluorescent photons emitted by the atoms while they are irradiated by resonant light. One useful method is to measure a MOT loading curve, in which the trapping magnetic field is switched on and atoms are allowed to gather in the trap over time while measuring the time-dependent fluorescence signal. This allows the initial signal where there are no atoms in the trap to be used as a reference for background-correction, leaving only the signal acquired from atomic fluorescence. It also allows the lifetime of the MOT to be extracted.

The loading dynamics of the MOT are described by the rate equation given by equation 4.2. The loading time of the MOT $\tau = 1/\gamma$, also known as the lifetime, is the time taken for $(1-1/e)N_{\text{eq}}$ atoms to be trapped starting from a background vapour of rubidium atoms by switching on the trapping magnetic field. This is a useful quantity to measure as it can be used in conjunction with the equilibrium number of atoms to obtain a measurement of the background pressure of the vacuum, in the form of pressure rise $(N_{\text{eq}} - \tau)$ curves [88]. It is important to ensure that this background pressure is low enough as to not limit the loading of atoms in the MOT by collisions with the background vapour.

N can be expressed in terms of N_{eq} and τ as

$$N(t) \;=\; N_{\text{eq}}\left(1 - e^{t/\tau}\right), \tag{4.3}$$

which is repeated here from section 4.2 for clarity. By fitting a curve based on this

equation to experimentally measured loading curves, N_{eq} and τ can be extracted, telling us the number of atoms and lifetime of the MOT.

To obtain a loading curve for our MOT, the fluorescence was collected using a Thorlabs DET100A/M silicon detector-based photodiode positioned just outside the vacuum chamber viewport window. A lens was mounted in front of the photodiode as close to the chamber window as practically possible to focus light onto the detector area, giving a solid angle of $\Omega = 0.074$ sr. The number of atoms in the MOT can be determined by considering the voltage returned by the photodiode for an incident power produced by N atoms. This gives

$$N = \frac{4\pi V}{\epsilon' P_0 \Omega} \tag{4.6}$$

where V is the voltage acquired from the photodiode, P_0 is the power emitted by a single rubidium atom while undergoing fluorescence driven by resonant light, Ω is the solid angle of the detection area for the photodiode and ϵ' is the effective responsivity of the photodiode. The power of the fluorescence emitted by one atom is derived by multiplying the power of one photon $\hbar\omega$ by the scattering rate given in equation 3.23, giving $P_0 = 4.8$ pW. For this calculation it is assumed that the detuning $\Delta = 0$ and $I \gg I_{\text{sat}}$ such that the scattering rate reduces to $\Gamma/2$. The effective responsivity is given by $\epsilon' = R_{\text{load}}\epsilon$ where R_{load} is the load resistance and ϵ is the true responsivity of the diode. This responsivity was measured to be $\epsilon = (0.45 \pm 0.03)$ by sending a beam of known power, greatly attenuated using optical density filters, onto the diode and measuring the resultant voltage acquired.

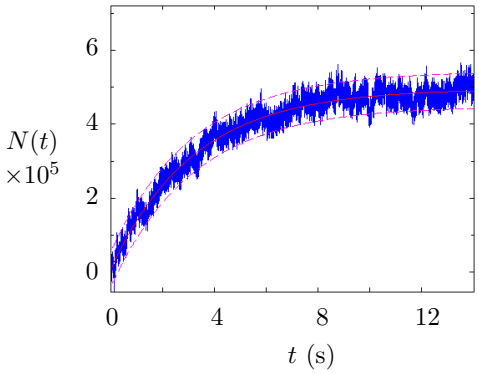

Figure 4.11: Typical measured loading curve of the magneto-optical trap for characterisation of the number of atoms N and MOT lifetime τ. The blue trace shows the raw measured voltage signal, which is background-corrected by subtracting the initial value at $t = 0$ s and translated into a number of atoms by multiplying by a constant scaling factor. The red line shows the exponential fit to the data, from which the equilibrium number of atoms reached $N_{\mathrm{eq}} = (4.9 \pm 0.5) \times 10^5$ and $1/e$ lifetime $\tau = (3.2 \pm 0.3)$ s are extracted.

Figure 4.11 shows a single loading curve measured by switching on the trapping magnetic field at $t = 0$. The acquired voltage signal $V(t)$ was background-corrected by subtracting the average signal acquired for 1 second before the start of loading, then converted to $N(t)$ using equation 4.6. A curve based on equation 4.3 was fitted to the data using MATLAB, from which values for the equilibrium number of atoms $N_{\mathrm{eq}} = (4.9 \pm 0.5) \times 10^5$ and lifetime $\tau = (3.2 \pm 0.3)$ s were obtained.

Density

The number density $\rho = N/V$ can be determined by simply taking a measurement of the number of atoms N and dividing by the spatial volume of the trap, V. In order to estimate the volume of the trap the size must be measured using a

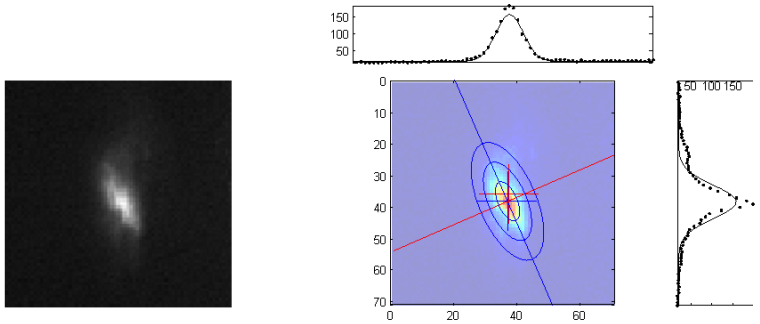

Figure 4.12: 2D Gaussian fitting to an average of 10 images of the MOT captured by the Marlin F033B camera. A 1 ms exposure time was used. The original greyscale averaged image is shown on the left. A 2D Gaussian function was fit to the image using MATLAB, shown on the right, giving standard deviations along the major and minor axes of $\sigma_1 = (0.51 \pm 0.04)$ mm and $\sigma_2 = (0.23 \pm 0.02)$ mm respectively.

camera. A Marlin F033B camera is used to capture an image of the MOT, after which the image is processed in MATLAB by fitting a 2D Gaussian function. The standard deviations of the Gaussian functions along the major and minor axes, σ_1 and σ_2 respectively, are obtained from the fitting. An image of the MOT after the fitting process is shown in Figure 4.12. The density can then be approximated as

$$\rho \approx \frac{N}{(2\pi)^{3/2}\sigma_{\text{av}}^3} \tag{4.7}$$

where $\sigma_{\text{av}} = \frac{\sigma_1 + \sigma_2}{2}$ is the average size in one dimension and assumed to be roughly equal in all three spatial dimensions of the MOT. Typical measured values of σ_{av} are around 0.4 mm, giving density values of around 5×10^8 cm^{-3}. In the case of the MOT size measured in Figure 4.12, the resulting density is calculated as $\rho = (6.2 \pm 0.6) \times 10^8$ cm^{-3}, assuming a number of atoms equal to that measured from the loading curve presented in Figure 4.11, $N = (4.9 \pm 0.5) \times 10^5$.

Temperature

The temperature of the atoms in the magneto-optical trap is an important physical property as it has a direct impact on the loading dynamics of a dipole trap. The measured temperature is also a good indicator of how well the MOT beams and fields are aligned and if there are any unwanted heating processes present. As shown in equation 3.30, atoms in the presence of laser light experience a spatially-dependent dipole potential proportional to the beam intensity [84]. For a focussed dipole trapping beam, this manifests as a trapping potential well with depth U_0, which contains atoms with a distribution of kinetic energies. The mean kinetic energy per atom is $3k_{\mathrm{B}}T/2$. The trap depth is usually quoted as a temperature in the form of U_0/k_{B}, and atoms can be efficiently loaded into a trap if their temperature is well below this trap depth. The trap depth of an optical dipole trap is typically on the order of mK, in contrast to the trap depth of the MOT which is in the range of K. As the MOT provides a reservoir of atoms to load the dipole trap from, it is important to ensure there are enough MOT atoms at a low enough temperature for efficient dipole trap loading. While the dipole trap depth can be controlled to a degree by adjusting the intensity or waist of the beam, it is appropriate to set a target of well below 1 mK, in the range $100 - 500$ μK, for the temperature of the MOT atoms as this would enable efficient loading of the dipole trap. Low MOT temperatures can be achieved by ensuring the trapping beams are well balanced and aligned and by optimising their detuning.

As with the number of atoms, there exist different methods for measuring the temperature of the atoms in the MOT. Two methods were attempted, the first

being the release-recapture method [94] and the second being the time of flight method [95]. Both of these involve interrupting the trapping allowing the atoms to expand thermally for a short time and deducing the temperature by relating the thermal velocity of the atoms to a Maxwell-Boltzmann distribution.

Release-recapture

The implementation of the release-recapture method uses a similar process as the loading curve used to measure the atom number and lifetime. First the trapping magnetic field is switched on and atoms are allowed to be trapped in the MOT until the equilibrium number of atoms has been reached, while the fluorescence signal from the atoms is recorded continuously using the Thorlabs DET100A/M photodiode. Following this the trapping magnetic field and cooling and repump beams are switched off simultaneously for a release time dt between 1 and 50 ms, during which no fluorescence is detected from the atoms and they are allowed to expand thermally in darkness. Both cooling and repump beams are switched off to ensure that no light forces are present which would interfere with the temperature measurement by altering the velocity of the atoms. After dt the field and beams are switched back on and the photodiode immediately captures fluorescence from all the atoms remaining in the MOT capture region as the MOT begins to load again. The experimental sequence is displayed in Figure 4.13. The recapture fraction r, being the fraction of atoms left in the capture region immediately after dt, can be deduced from the ratio between the fluorescence signal before and after dt. Using a suitable approximation for the size of the capture region, the temperature can be calculated by relating r to the thermal velocity distribution of the atoms. A typical signal trace from the

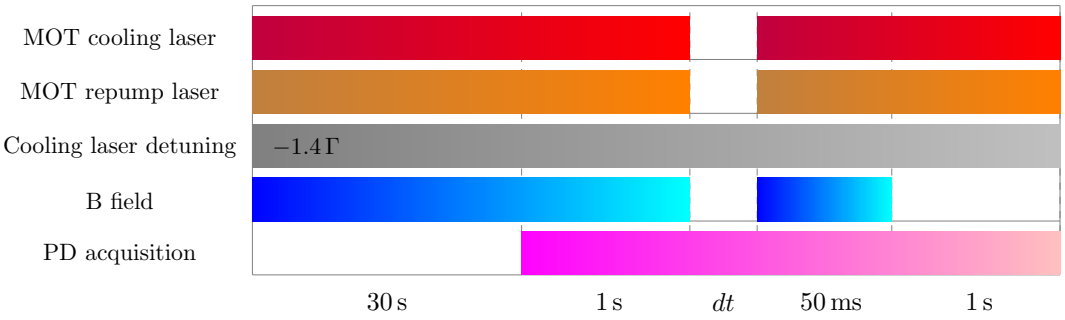

Figure 4.13: Diagram showing the experimental sequence for the measurement of the MOT temperature using the release-recapture (RR) method. First the MOT is loaded for 30 s at a laser detuning $\Delta = -1.4\,\Gamma$, cooling beam power $\sim 30\,I/I_{\mathrm{sat}}$, total repump beam power 3.5 mW and trapping field coil current 3.6 A. The signal from the photodiode is then acquired for 1 s to measure the fluorescence level of the initial fully-loaded MOT. The trapping beams and field are then switched off for a variable time dt, releasing the MOT atoms and allowing them to expand thermally in space. The trap is then switched back on to obtain the recapture fraction. The trapping field is then switched off to remove the MOT and measure the background level including stray light from the lasers.

photodiode used to obtain $r\,(dt)$ for a given dt is shown in Figure 4.14.

Calculation of the temperature using this method relies on the assumptions that the capture region formed by the overlapping MOT beams is spherical, and that the MOT is effectively a point source at the centre of this region, from which the atoms travel in a direct linear path to the edge of the capture region. In other words, the assumption is made that the MOT is much smaller than the capture region. The recapture fraction can be described by an integral over the velocity distribution [94],

$$r = \frac{4}{\pi^{1/2}} \int_0^{v_{\mathrm{c}}/v_{\mathrm{T}}} u^2 e^{-u^2}\, du, \tag{4.8}$$

where $v_{\mathrm{T}} = \sqrt{\frac{2k_{\mathrm{B}}T}{m_{\mathrm{Rb}}}}$ is the thermal velocity and v_{c} is the capture velocity, being the velocity required for an atom to reach the edge of the capture region starting from the centre of the cloud in the release time dt. Assuming that the recapture

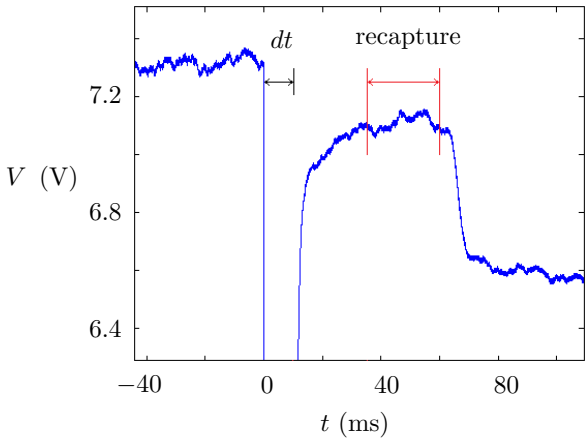

Figure 4.14: Acquired voltage from the photodiode during an experimental release-recapture sequence. The initial signal from the fully loaded MOT is acquired for 1 s before $t = 0$. The beams and trapping field are then switched off for a time dt; in this case, 10 ms. The beams and field are then switched back on for 50 ms, allowing the atoms remaining in the capture region to be recaptured. The recapture fraction r is then the ratio between the average signal over the range marked 'recapture' and the average signal from the MOT before dt, relative to the background level.

region is spherical and has a constant radius R_c, then $v_c = R_c/dt$. The solution to the integral in equation 4.8 is given by [94]

$$r\,(dt) \;=\; -\,\frac{2t_e e^{-t_e^2/dt^2}}{\sqrt{\pi}dt} \;+\; \mathrm{Erf}\,[t_e/dt] \tag{4.9}$$

where the 'escape time' $t_e = R_c/v_T$ is the time taken for an atom travelling at the thermal velocity v_T to travel the distance R_c to the edge of the capture region. During the experiment r was measured with varying dt and equation 4.9 was fitted to the data in MATLAB using t_e as the fitting parameter. The resulting value of the escape time obtained from fitting is given by $t_e = (6.8 \pm 0.5)$ ms. The average temperature of the atoms can then be extracted by substituting t_e into the equation for the thermal velocity v_T and rearranging, giving

$$T \;=\; \frac{m_{\mathrm{Rb}}}{2k_B}\left(\frac{R_c}{t_e}\right)^2. \tag{4.10}$$

The results of the release-recapture method are plotted in Figure 4.15, giving a measured temperature of $T = (370 \pm 110)$ μK. The escape time t_e was derived from a curve fitted to the data based on equation 4.9, following which the temperature was found using equation 4.10. To obtain this result the recapture radius was assumed to be equal to the MOT beam radius at the trap, (1.8 ± 0.5) mm. The uncertainty in the temperature has been carried forward through equation 4.10 using the uncertainties in the obtained fitting parameter t_e and the recapture radius.

It can be seen that the fitted curve is outside the range of the error bars for much of the data, particularly for data points near the beginning and end of the release

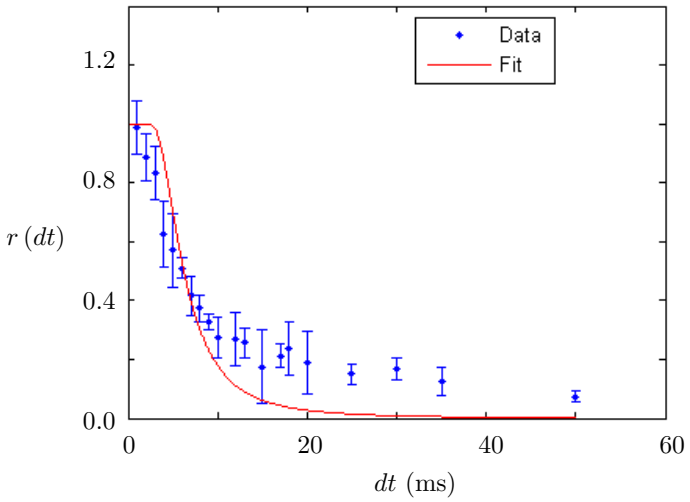

Figure 4.15: Experimental data for the release-recapture method for the measurement of MOT temperature, showing the recapture fraction $r\,(dt)$ in terms of the release time dt. The experimental data is represented by the blue data points along with error bars. A fit to the data based on equation 4.9 was obtained in MATLAB and is represented by the red curve. The resulting temperature obtained from this fit is $T = (370 \pm 110)$ μK.

stage. For the first few data points this can be explained by considering the fact that this model makes the assumption that the MOT atoms are all released from a point at the centre of the capture region, in other words, that the MOT is much smaller than the capture region. This results in the initial plateau in the fitted curve during which none of the atoms have reached the edge of the capture region yet. However, if the MOT is not much smaller than the capture region then we would expect to see a decrease in r earlier than predicted by the model, as the outermost MOT atoms are able to escape more quickly than the innermost ones. Indeed, as demonstrated in section 4.3.1, typical measurements of the MOT size by fitting a 2D Gaussian function give a FWHM of roughly 1 mm, which is a significant fraction of the recapture radius. For the final data points at $dt > 15$ ms, the recapture fraction remaining above zero in contrast to the fitted model can be explained by the fact that a small delay is included in the experimental sequence between switching the MOT back on and measuring the recapture fraction. This can allow the MOT to begin loading atoms from background vapour, resulting in a non-zero r even for large dt.

The recapture region R_c itself is a quantity of significant uncertainty, as it is assumed to be a spherical region centred on the MOT with a radius equal to that of the MOT beams, whereas the true capture region is likely to be more complicated than this, considering that the alignment of the beams and field may not be perfectly symmetrical. As the resulting temperature T from equation 4.10 scales with the square of R_c, this introduces a great uncertainty in T, as even a small change in R_c causes a large difference in temperature. It is also likely that the centre of the MOT is not located at the centre of the crossing point of

the beams, due to asymmetry of the alignment of the beams, so that the MOT atoms may be close to the edge of the capture region, causing atoms to escape from the capture region more quickly than expected. It can be seen that the initial decay in recapture fraction follows a shallower gradient than that of the fitted curve. This suggests that the actual temperature of the MOT atoms may be lower than measured, and that the result can be interpreted as an upper limit to the temperature of the atoms.

Time-of-flight: MOT

In order to compare and test the validity of the results obtained by the release-recapture method for MOT temperature, a second method was used to measure the temperature, the time-of-flight (TOF) method. This is a more commonly used method which involves the direct measurement of the size of the cloud as it expands while the trapping field is switched off. As the photodiode used for the release-recapture method only acquires a signal proportional to the incident light power on the detector, it provides no information about the spatial distribution of the MOT atoms, therefore the Marlin F033B camera is used to image the MOT atoms for the TOF measurement instead. The experimental sequence used is as follows: first the MOT is allowed to load from the background vapour for 10 seconds, which ensures that the equilibrium number of atoms is reached. Following this the cooling and repump beams are simultaneously switched off for a time dt, allowing the MOT atoms to expand thermally in darkness with no trapping or light forces present. Following this the beams are switched back on at the same time as the Marlin camera is triggered, capturing the fluorescence emitted by the atoms for a 1 ms exposure time. This sequence

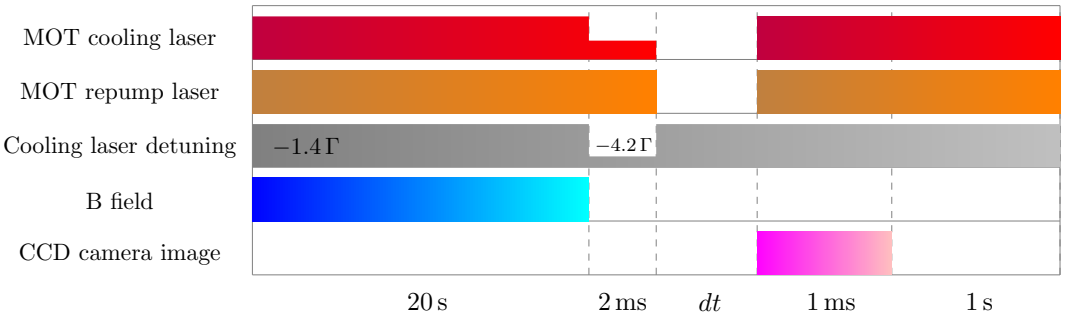

Figure 4.16: Diagram showing the experimental sequence for the measurement of the MOT temperature using the time-of-flight (TOF) method. First the MOT is loaded for 20 s at a laser detuning $\Delta = -1.4\,\Gamma$, cooling beam power $\sim 30\,I/I_{\mathrm{sat}}$, total repump beam power 3.5 mW and trapping field coil current 3.6 A. This is followed by a 2 ms molasses stage during which the trapping field is switched off, the cooling beam detuning is increased to $-4.2\,\Gamma$ and the cooling beam power is reduced to $\sim 10\,I/I_{\mathrm{sat}}$. The trapping beams and field are then switched off for a variable time dt, releasing the MOT atoms and allowing them to expand thermally in space. The laser light is then switched back on to image the atoms after expansion. The experiment was done both with and without the 2 ms molasses stage.

is displayed in Figure 4.16. The resulting image of the MOT acquired by the camera is processed by fitting a 2D Gaussian in exactly the same way as for the measurement of MOT size described in section 4.3.1. The standard deviations of the Gaussian functions along the major and minor axes, σ_1 and σ_2 respectively, are obtained from the fitting.

While expanding thermally, the atoms have a Maxwell-Boltzmann velocity distribution and therefore the width of the cloud in one dimension is described by [83]

$$\sigma^2(dt) = \sigma_0^2 + \frac{k_{\mathrm{B}}T}{m_{\mathrm{Rb}}}dt^2 \tag{4.11}$$

where $\sigma_0 \equiv \sigma(0)$ is the initial size of the MOT cloud at $dt = 0$. The time-of-flight measurement was done for the MOT, measuring the cloud size at $dt = 0, 1, 2, ..., 5$ ms. For each value of dt, an average image was obtained

from 10 TOF sequences, and the average width $\sigma_{\text{av}} = \frac{\sigma_1 + \sigma_2}{2}$ was obtained by 2D Gaussian fitting in MATLAB. The results are displayed in Figure 4.17 (a), showing a linear relationship between σ_{av}^2 and dt^2 as expected from equation 4.11. A linear fit to the data was produced using MATLAB and the temperature was derived from the resulting fit, giving $T = (500 \pm 63)$ μK. Here, the uncertainty has been carried forward from the variance in cloud size over the 10 runs of the experimental sequence per dt.

In contrast to the release-recapture results, there is good agreement between the experimental data and the theoretical model, with all data points within error of the fitted line. However, in this experiment the effect of the MOT beams on the atoms during the camera exposure has not been taken into account. As the beams are switched on for 1 ms during imaging, which is a significant duration compared to the dt values used, there would have been light forces acting on the atoms during this time. For the ideal case in which the beams are perfectly aligned and balanced in intensity, this would act to slow the atoms by molasses. However, as the beams are likely to be unbalanced, the radiation forces instead can cause the ejection of atoms from the trap, leading to a perceived expansion of the atom cloud. This could result in a larger cloud size measured for each dt, which may result in the measurement of a temperature higher than the actual temperature of the atoms. This may help to explain why the MOT temperature measured using the time-of-flight method is higher than that measured using the release-recapture method.

Time-of-flight: molasses

In order to try to reduce the temperature of the MOT atoms, the same TOF

measurement was done with a 2 ms molasses stage introduced after the initial MOT loading stage and before the time-of-flight stage. During the molasses the trapping magnetic field was switched off, the detuning of the MOT beams was increased from $-1.4\,\Gamma$ to $-4.2\,\Gamma$, and the power of the cooling beams was reduced from 2.1 mW to 0.7 mW. The same experimental procedure was carried out as for the MOT, for $dt = 0, 1, 2, ..., 8$ ms. The results are shown in Figure 4.17 (b), giving a molasses temperature of $T = (79 \pm 9)$ μK, showing a significant decrease in temperature compared to the MOT. This value is below the Doppler temperature limit of 146 μK for ^{87}Rb [69], confirming the presence of sub-Doppler cooling. Again there is good agreement between the theoretical model and the data. For both the MOT and molasses the 2D Gaussian fits to the averaged camera images with increasing dt shown below the plots show a roughly uniform thermal expansion in all directions, with the spatial distribution well approximated by the Gaussian fitting. A comparison of the results obtained by the release-recapture and time-of-flight methods is displayed in table 4.1.

The goodness of fit to the data for the release-recapture and time-of-flight method was tested by χ^2 analysis, concluding that the time-of-flight method had produced a better fit to the data. Due to achieving better agreement with the theoretical model, the results of the MOT temperature measurement obtained using the time-of-flight method are considered more reliable than those obtained by the release-recapture method. All measurements demonstrate a MOT temperature well below 1 mK, meeting the approximate target set to ensure the possibility of optical dipole trap loading using the MOT as a reservoir of atoms, as typical dipole trap depths are on the order of mK.

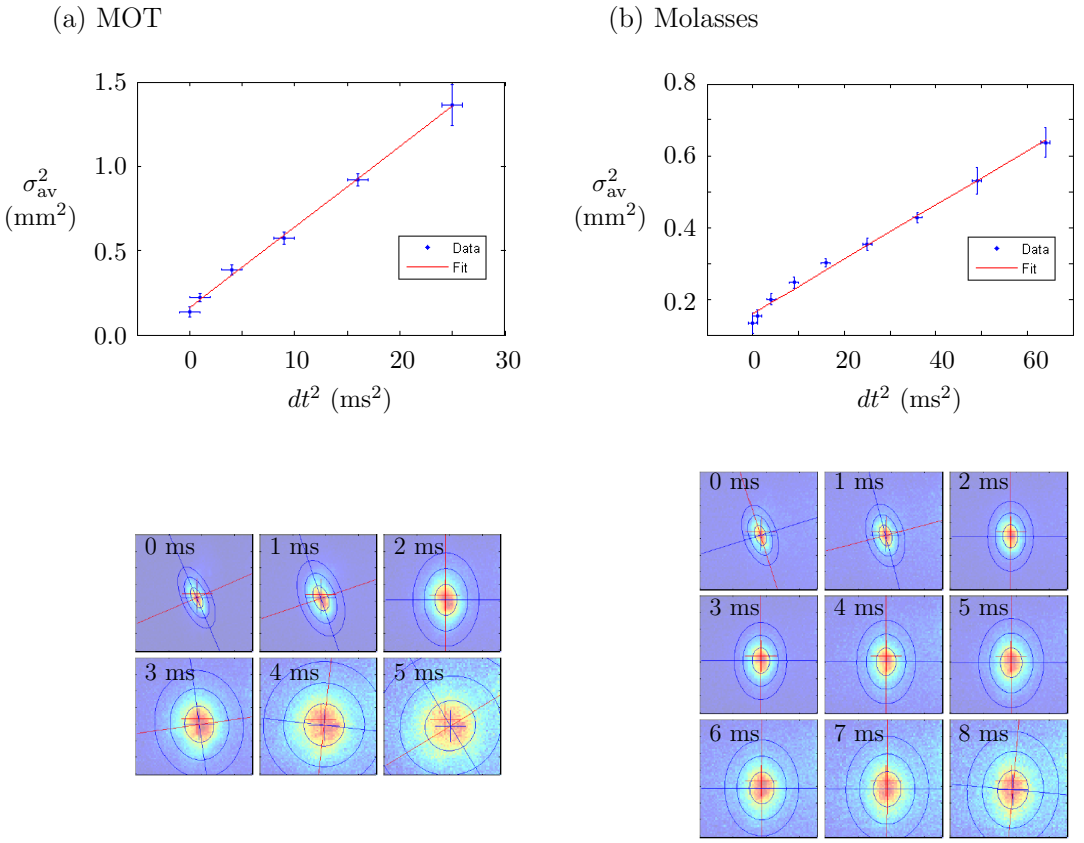

Figure 4.17: Experimental data for the time-of-flight (TOF) method for measurement of the MOT and molasses temperature, showing the size of the cloud derived from 2D Gaussian fitting, σ_{av}, as a function of the time of flight dt. Results for the MOT are shown in (a) and results for including a 2 ms molasses stage after MOT loading are shown in (b). The experimental data is represented by the blue data points along with error bars. Linear fitting to the data based on equation 4.11 was done in MATLAB and represented by the red lines, corresponding to a measurement of $T = (500 \pm 63)$ μK for the MOT and $T = (79 \pm 9)$ μK for the molasses. The 2D Gaussian-fitted images for each data point are displayed beneath each of the plots.

	MOT		Molasses
	RR	TOF	TOF
T (μK)	370	500	79
ϵ_T (μK)	110	63	9

Table 4.1: Summary of temperature measurement results for the release-recapture (RR) and time-of-flight (TOF) methods. The standard uncertainty is denoted by ϵ_T.

4.4 Summary

In this chapter, the experimental apparatus for magneto-optical trapping of rubidium atoms inside an ultra-high vacuum chamber has been presented. In section 4.1, the laser system used for trapping was introduced. Extended cavity diode lasers are used to drive the cooling and repump transitions for the cooling of rubidium atoms, which for ^{87}Rb are the $5^2S_{1/2}F = 2 \rightarrow 5^2P_{1/2}F = 3$ and $5^2S_{1/2}F = 1 \rightarrow 5^2P_{1/2}F = 2$ transitions respectively. The frequency locking system used to stabilise these lasers is done using saturated absorption spectroscopy, in which counter-propagating beams are used to remove Doppler broadening and produce sub-Doppler transition peaks, from which the error signal used for locking is derived.

A vacuum chamber operating at ultra-high vacuum (UHV) pressures in the range of $\lesssim 10^{-9}$ mbar is required for the implementation of atom traps such as the magneto-optical trap (MOT) and dipole trap, due to collisions with background vapour ejecting atoms from the trap. It has been discussed in section 4.2 how the original chamber in the laboratory was unsuitable for experiments due to a leak, and needed to be dismantled for repair. Improvements were made to the design of the chamber upon rebuilding, and the process for the cleaning and construction of the chamber has been described. The chamber was baked to increase the rate of outgassing, allowing pumping down to the final pressure. The rebuilding and baking of the chamber was successful, resulting in a final pressure of below 5×10^{-10} mbar, which is appropriate for our atom trapping experiments.

Experimental measurements were done to characterise the properties of the

magneto-optical trap obtained in the laboratory. The number of atoms and lifetime of the MOT were measured by observing loading curves of the emitted fluorescence on an infrared camera, giving $N_{\mathrm{eq}} = (4.9 \pm 0.5) \times 10^5$ atoms in the fully-loaded MOT with a lifetime of $\tau = (3.2 \pm 0.3)$ s. The size of the MOT was estimated from the camera images, giving a typical average radius of the atom cloud of $\sigma_{\mathrm{av}} \sim 0.4$ mm, resulting in an atom number density of $\rho = (6.2 \pm 0.6) \times 10^8$ cm^{-3}. The temperature of the MOT atoms was measured using the release-recapture and time-of-flight methods. The time-of-flight method was concluded to have produced the more accurate result, giving a temperature of $T = (500 \pm 63)$ μK for the MOT and $T = (79 \pm 9)$ μK for the molasses.

The main purpose of the MOT obtained in the laboratory is to provide a reservoir of cold atoms from which an optical dipole trap can be loaded. In the following chapter, the experimental set up and characterisation of a microscopic dipole trap is presented, with the aim of producing small numbers of trapped atoms capable of being implemented as an atomic qubit.

Chapter 5

Implementation of a Microscopic Dipole Trap

As described in section 3.3, dipole trapping is a powerful technique capable of creating small traps containing tiny numbers of atoms, and even single atoms may be trapped when set up with the correct trapping parameters [96–100]. The use of dipole traps is seen as a versatile and promising method for the preparation of atoms for applications in quantum information processing using neutral atoms, due to the high degree of control achievable over small ensembles of atoms which can be used as qubits [29, 37, 58, 74, 80]. Dipole trapping relies on a different physical process to the near-resonant laser cooling which is involved in the operation of the magneto-optical trap, using the dipole force to push atoms to the point of maximum intensity rather than radiation pressure. The dipole trap is typically implemented using a single intense far off-resonance laser, focussed to create an intensity gradient with a maximum intensity at a certain point in

space. This chapter includes the practical implementation of the trap in the laboratory and the experiments done to characterise the properties of the trap and the behaviour of the trapped atoms. The following section details how the trap is set up in the laboratory, as well as the imaging system used to acquire measurable fluorescence emitted by the trapped atoms.

5.1 Dipole Trap Laser and Imaging System

The dipole trapping beam is provided by a 852 nm laser diode housed in a home-built mount with an extended cavity, similar to the lasers used for the MOT cooling and repump beams. The laser has a maximum output power of 155 mW. The laser is temperature-stabilised using a Peltier cooler connected to an external Thorlabs TED200C PID controller. The dipole trap laser is tuned far from the 780 nm cooling transition, so no locking system is required for this laser, as even large frequency drifts are negligible compared to the detuning. The laser is directed into the vacuum chamber through an anti-reflection coated glass viewport by optical elements including infrared mirrors, a prism pair to correct the beam shape, and a pair of collimating lenses, and focussed strongly at the centre of the MOT position by a high numerical aperture (NA) lens. The same high-NA lens is used to collimate the infrared light emitted as fluorescence from the Rb atoms trapped in the dipole trap. This light is directed outside the chamber and used to image the trapped atoms on an Andor iStar intensified charge coupled device (ICCD) camera. The dipole trapping laser and imaging setup is shown in Figure 5.1.

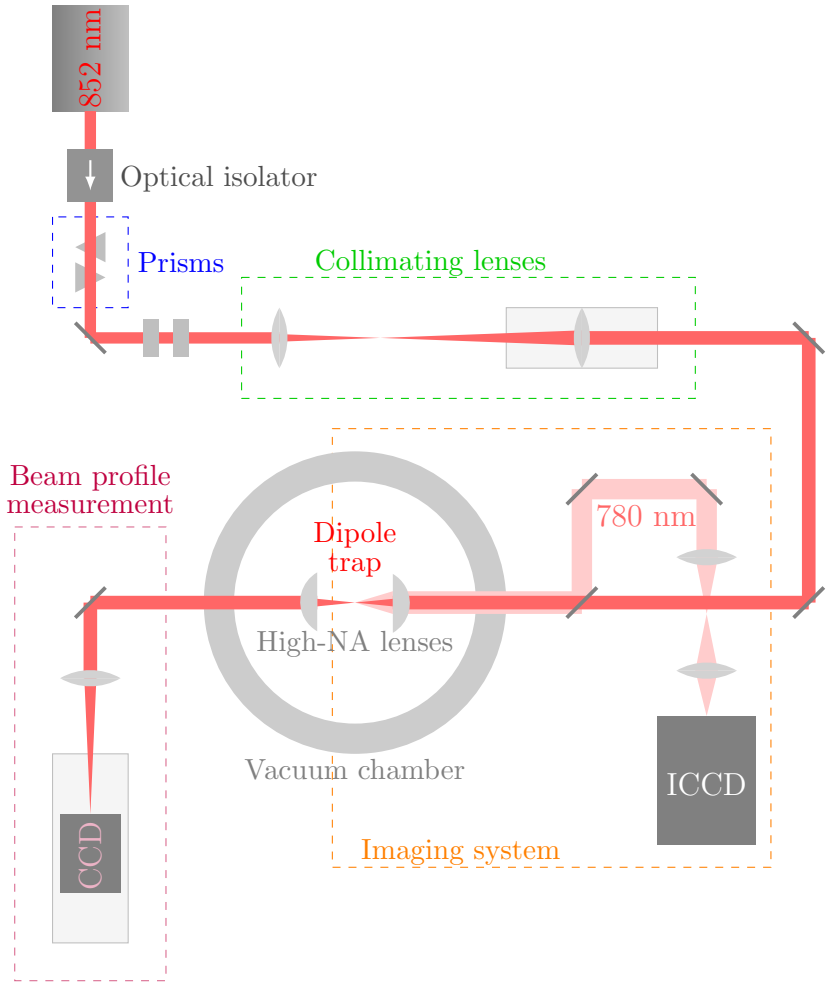

Figure 5.1: Schematic showing the experimental setup for dipole trap imaging. The 852 nm dipole trap laser passes through a shape-correcting prism pair and collimating lenses before being focussed using a high-NA lens to produce a dipole trap in the centre of the vacuum chamber. The 780 nm fluorescence from the trap is collected using the same lens and focussed onto the ICCD camera for imaging. The dipole trapping beam is focussed onto a CCD camera for reconstruction of the trap profile, giving an indirect measurement of the trap size, depth and induced light shift. See text for an in-depth description of the purpose and operation of each part of the system.

5.1.1 High-NA lenses

The lenses used for the focussing of the dipole beam and collection of the fluorescence from the trap were produced by LightPath Technologies and have a numerical aperture of 0.53 and back-focal length of 7.03 mm. Typically a lens will focus incident collimated light at different positions depending on the wavelength of the light due to chromatic aberration; these lenses were chosen for the ability to exhibit similar behaviour for both 852 nm and 780 nm light, corresponding to the input trapping beam and the collected fluorescence respectively. For a collimated input trapping beam, the lenses are capable of collecting very nearly collimated 780 nm fluorescence with a high Strehl ratio of 0.997 [101]. The lenses were coated with an indium tin oxide (ITO) coating which prevents stray electric charge from building up on the lens surfaces; this could otherwise be a problem in future experiments, for example involving Rydberg atoms, which are highly sensitive to external electric fields. The lenses are mounted inside the vacuum chamber in a mount specially designed and built in collaboration with Chris Hall at the Research Design & Engineering Facility workshop at the Open University. The mount was built out of low-outgassing stainless steel to ensure it is UHV-compatible and is designed to hold the lenses plane-parallel at an exact distance of $2f$ from each other, equidistant from the chamber centre, where f is the lens focal length. During the design of the mount, it was important to maximise the optical access to the central MOT position so that the three pairs of MOT beams could reach the trap position without being obstructed. This was also an important factor in the choice of lenses to use, as they needed a long enough focal length to allow space for the MOT beams to pass between the

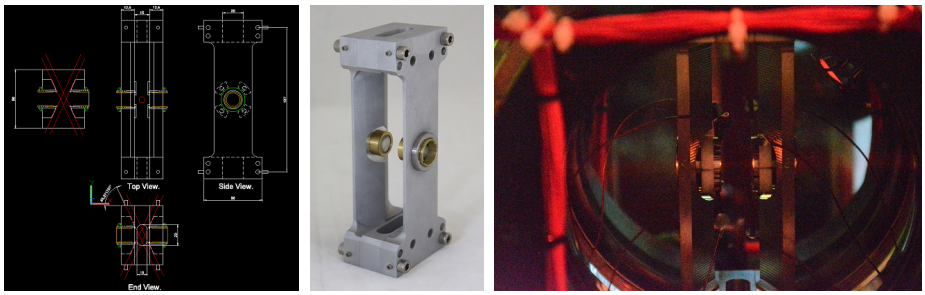

Figure 5.2: Custom-designed lens mount to hold the high-NA lenses used for dipole trapping of atoms and collection of emitted fluorescence for imaging. The left-hand image shows the design blueprint in AutoCAD software, the central image shows a prototype of the completed lens mount made from aluminium with the lenses mounted in screw-in holders, and the right-hand image shows the final completed stainless steel mount attached inside the vacuum chamber, with the dipole trapping beam visibly passing through the focussing lenses.

lenses, while still allowing a tightly focussed dipole trap to be produced. With the final design, a maximum angle of 49° is allowed between the two horizontal MOT beam pairs. The design of the lens mount is displayed in Figure 5.2, showing the design blueprint in AutoCAD software, a prototype mount made from aluminium and the final stainless steel mount attached inside the chamber with the dipole trap laser passing through the lenses.

5.1.2 Shape correction

The design and analysis of the optical system for the dipole trap was performed in [101] using the software Zemax. This software uses ray tracing to compute the evolution of the shape of a beam through optical elements, taking into account imperfections such as spherical aberrations. According to the results provided by this software, the position of the dipole trap is sensitive to the collimation of the input trapping beam, as a difference in collimation angle of 56 μrad is enough to

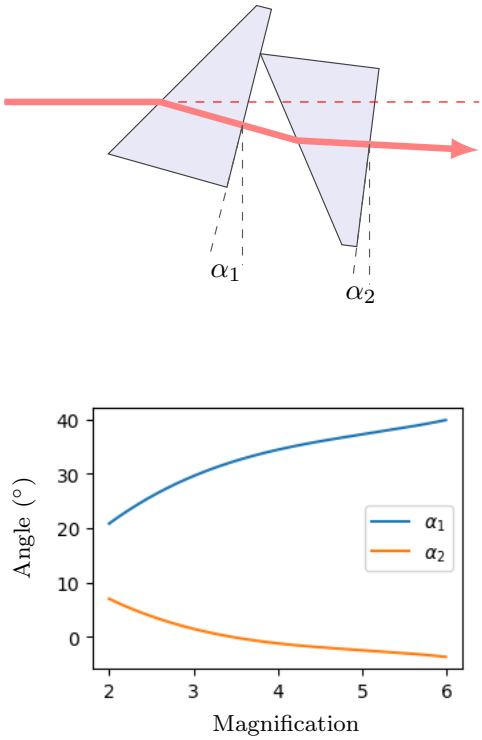

Figure 5.3: Prism pair setup for beam shape correction. The angles α_1, α_2 between the prisms are adjusted to achieve the appropriate magnification in one dimension.

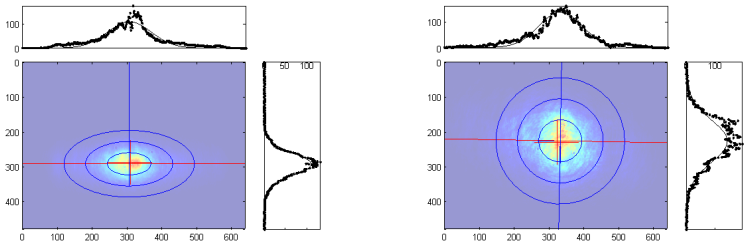

Figure 5.4: 2D Gaussian fitting to the profile of the dipole trap laser before (left image) and after (right image) the anamorphic prism pair. The standard deviations of the fitted Gaussian function in the horizontal and vertical directions for the beam before the prisms are $\sigma_H = (0.62 \pm 0.01)$ mm and $\sigma_V = (0.32 \pm 0.01)$ mm respectively, giving a ratio $\sigma_H/\sigma_V = 1.96 \pm 0.07$. For the resulting beam shape after the prisms, $\sigma_H = (0.61 \pm 0.01)$ mm and $\sigma_V = (0.60 \pm 0.01)$ mm, giving $\sigma_H/\sigma_V = 1.02 \pm 0.02$.

displace the trap along the imaging axis by 1 µm, which is comparable to the size of the trap. Similarly the size and shape of the input beam can strongly affect the intensity profile of the trap inside the chamber. The beam profile at the output of the laser is highly elliptical with a large divergence in the horizontal axis compared to near-collimation in the vertical axis, so the beam shape was first corrected roughly using a N-SF11 dense flint glass anamorphic prism pair with a refractive index of $n_{\text{prism}} = 1.76$ for a wavelength of 852 nm. An anamorphic prism pair is capable of converting an elliptical beam to circular by expanding or contracting the beam size in only one dimension. To obtain a circular beam profile, the angle of incidence for the beam entering the prism was set to the Brewster angle, being $\theta_{\text{B}} = \tan^{-1}(n_{\text{prism}}/n_{\text{air}}) = 60.4°$ for this wavelength, assuming $n_{\text{air}} = 1$. The angles α_1, α_2 shown in Figure 5.3 then had to be set to achieve the desired magnification in one dimension. The incoming beam shape was measured by imaging the beam on a Marlin F033B CCD camera with a neutral density filter attached to prevent oversaturation and damage to the CCD, and a 2D Gaussian profile was fit to the acquired image using MATLAB. The resulting standard deviations of the fitted Gaussian function in the horizontal and vertical directions were measured to be $\sigma_{\text{H}} = (0.62 \pm 0.01)$ mm and $\sigma_{\text{V}} = (0.32 \pm 0.01)$ mm respectively, resulting in a ratio $\sigma_{\text{H}}/\sigma_{\text{V}} = 1.96 \pm 0.07$. The prism angles were set to $\alpha_1 = 20.4°$, $\alpha_2 = 7.3°$ in order to magnify the beam in the vertical direction by approximately 2 times. The resulting beam shape after the prisms was measured to have $\sigma_{\text{H}} = (0.61 \pm 0.01)$ mm and $\sigma_{\text{V}} = (0.60 \pm 0.01)$ mm, giving a ratio $\sigma_{\text{H}}/\sigma_{\text{V}} = 1.02 \pm 0.02$. The Gaussian fits to the beam shape before and after the prism pair are displayed in Figure 5.4.

5.1.3 Collimation

Following the correction of the shape of the beam, the laser was collimated using a pair of lenses as shown in Figure 5.1. For a diverging beam incident on a plano-convex lens with focal length f_1, the beam will be focussed at a position $f_1 + df$ from the lens, where df is dependent on the incoming divergence. The beam can then be collimated by placing a second lens with focal length f_2 at a position $f_2 + df$ from the beam focus, equating to $f_1 + f_2 + 2df$ from the first lens. The choice of focal lengths f_1 and f_2 can be exploited to change the diameter of the beam, as the case where $f_1 < f_2$ results in an expansion of the beam size and $f_1 > f_2$ results in a contraction. This setup is represented diagrammatically in Figure 5.5 (a).

The first lens with focal length $f_1 = 300$ mm was fixed in place and used to focus the incoming beam. In order to measure the focus position and determine df, the beam size was measured with the Marlin CCD camera using the same method as during the prism pair beam shape correction described above, obtaining an average size $\bar{\sigma} = (\sigma_H + \sigma_V)/2$ at a range of positions x around f_1. The results are displayed in Figure 5.5 (b), showing the beam focus at a position 307 mm from the first lens, giving $df = 7$ mm. In addition, a curve was fit to the tail end of the beam size after the focus point, shown in Figure 5.5 (c), to extrapolate the beam size-position relation and determine the best focal length f_2 for the second lens. It was planned to focus the trapping beam inside the chamber down to a 2 µm waist, which corresponds to an input beam size $\sigma_H = \sigma_V = 0.68$ mm as calculated by the Zemax software using a ray tracing method. Collimating the beam at this size would require $f_2 = 220$ mm. Due to the unavailability of a lens

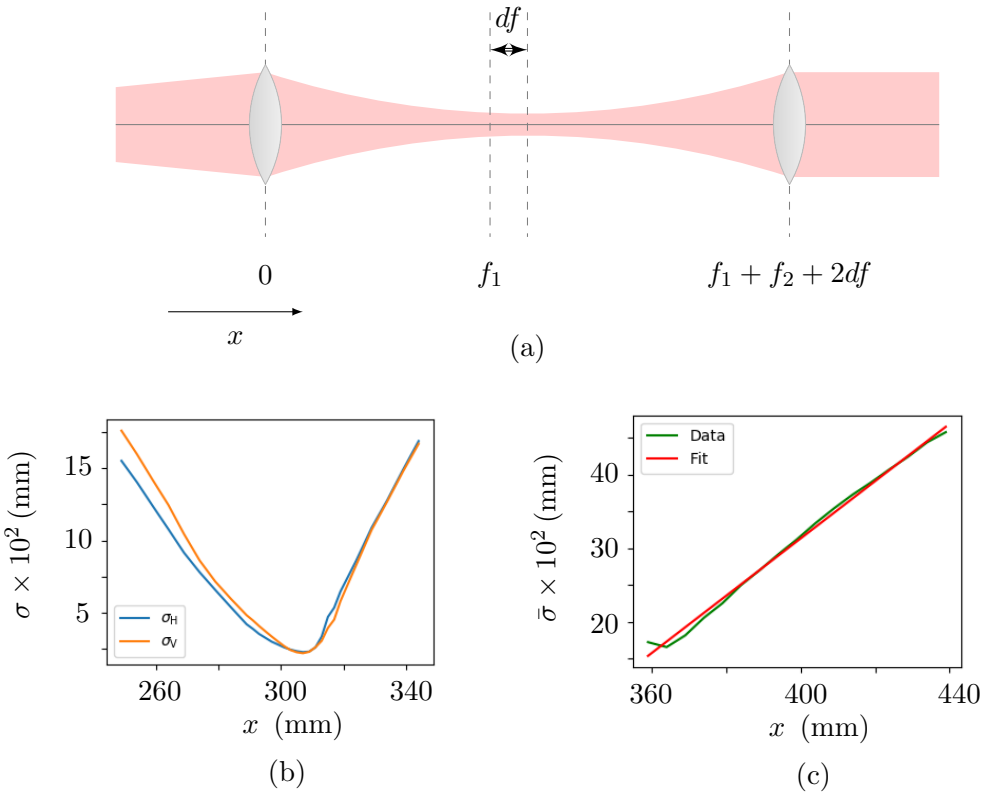

Figure 5.5: Collimation of the dipole trap beam. In (a), a schematic of the lens placement for collimation is shown. For a pair of lenses with focal lengths f_1 and f_2, the second lens is placed at a distance $f_1 + f_2 + 2df$ from the first lens, where df is the separation between the focal point of the first lens and the actual focus of the incoming beam. In (b), the measurement of the beam size σ in the horizontal (H) and vertical (V) directions with distance from the first lens is displayed, showing $df = 7$ mm from $f_1 = 300$ mm. In (c), a curve was fit to the tail end of the average beam size to determine what focal length f_2 to use for the final collimated beam size of $\sigma_H = \sigma_V = 0.68$ mm, resulting in $f_2 = 200$ mm being chosen.

with this focal length, $f_2 = 200$ mm was used instead, so a trapping beam waist of slightly less than 2 μm was expected. A measurement of the final trapping beam waist obtained is presented in section 5.2.1.

5.1.4 Imaging system

The system for imaging the atoms in the dipole trap by their emitted fluorescence takes advantage of the high-NA lens for focussing the trapping beam by collecting and collimating the fluorescence using the same lens. As described in section 5.1.1, this lens was specifically chosen to have similar properties at both the wavelengths of the 852 nm trapping beam and 780 nm fluorescence in order to make this operation feasible. As the fluorescence is emitted uniformly in all directions, the solid angle of (0.14 ± 0.01) sr of the high-NA lens leads to a collection efficiency of 14%. The dipole trap imaging system can be seen in Figure 5.1 within the area marked 'Imaging system', showing the collection of the 780 nm fluorescence from the trapped atoms inside the vacuum chamber onto the ICCD camera. After being collimated by the lens the fluorescence is overlapped with the trapping beam, propagating in the opposite direction. Outside the chamber it is separated from the trapping beam using a dichroic mirror which reflects 780 nm light and transmits 852 nm. The light is focussed using a large aspheric lens with focal length 150 mm. A second aspheric lens with focal length 40 mm is placed beyond the focal point of the first lens, to focus the light onto the ICCD camera. The purpose of the first lens is to provide a focal plane in which a pinhole could be placed to remove stray light from the imaging path, however a pinhole was not used for the measurements described in this work.

The design, setup and testing of the optical system for imaging is described in detail in [101] and remains largely unchanged. It is designed to give a magnification $M = 14.32$ of the trap image on the ICCD, this being the optimal magnification for focussing light from 1 μm in the object space (the typical size of a dipole-trapped atom cloud) onto a single 2×2 binned pixel of the ICCD, corresponding to an area of 26 μm × 26 μm, to maximise the signal-to-noise ratio. In this work the average cloud diameter is found to be slightly larger than 1 μm and displaced along the imaging axis from the intended position, but the imaging system is still appropriate for imaging of the trap and operates well, focussing the trap fluorescence onto just a few pixels and allowing sharp images of small numbers of trapped atoms to be obtained. For the calculation of the number of trapped atoms, which is important for the characterisation of many of the physical properties of the trap, it is necessary to estimate the losses induced by the imaging system and obtain a conversion factor which can be used to translate acquired pixel counts into the number of atoms.

To translate the pixel counts of the image into the number of atoms, the imaging system must be calibrated by measuring the counts obtained for a known light power incident on the ICCD camera. For the purpose of this measurement, a weak 780 nm beam was directed through the vacuum chamber in the opposite direction to the dipole trap laser towards the ICCD camera so that the light loss associated with the optical elements along the beam path could be measured. This beam was used as it has a frequency close to that of the fluorescence emitted by the dipole trapped atoms, so it can be used to simulate the measured fluorescence. The loss factor due to the chamber and imaging optics was measured to be

$L_{\text{path}} = (0.5502 \pm 0.0004)$, and the loss due to the 780 nm filter attached to the front of the ICCD was measured to be $L_{\text{filter}} = (0.475 \pm 0.007)$. The beam was imaged using the ICCD camera with an incident power of (28.9 ± 0.4) pW and an exposure time of 0.3 s. A single image was acquired and subsequently background corrected by taking a background image with the laser switched off. During this process the ICCD was deliberately displaced so the beam was dispersed and out of focus, to avoid over-saturating any pixels. The resulting total number of pixel counts acquired on the camera was $(1.27 \pm 0.02) \times 10^6$, corresponding to a translation factor from power to pixel counts of $TF_{\text{p}\to\text{c}} = (1.46 \pm 0.03) \times 10^6\,\text{counts}\,\text{s}^{-1}\,\text{pW}^{-1}$.

The power emitted by a single atom by stimulated emission is calculated as the energy of one photon $E = hc/\lambda$ multiplied by the scattering rate, which is given by $R = \Gamma/2$ assuming the driving radiation is close to resonance and of a high enough power that $I/I_{\text{sat}} \gg 1$ [49]. This gives the power of one emitted photon as $P_{\text{photon}} \sim 4.8$ pW. The losses associated with the solid angle of the collecting lens and optical elements along the imaging path reduce this to (0.26 ± 0.03) pW per atom incident on the ICCD. Combining this with $TF_{\text{p}\to\text{c}}$, we obtain the full translation factor from number of atoms to pixel counts, $TF_{\text{n}\to\text{c}} = (3.8 \pm 0.4) \times 10^5\,\text{counts}\,\text{s}^{-1}\,\text{atom}^{-1}$. This allows the number of atoms to be deduced from an ICCD camera image, given by

$$N_{\text{DT}} = \frac{C \cdot r}{TF_{\text{n}\to\text{c}} \cdot g \cdot t_{\text{e}}} \tag{5.1}$$

where C is either the total sum of pixel counts in the image or volume of pixel counts under a 2D Gaussian fit to the image of the trap, r is a correction factor

for the Stark shift, g is the intensifier gain and t_e is the camera exposure time in seconds. The number of atoms can be obtained with an uncertainty of around 10%. The main source of this uncertainty is from the translation factor $TF_{n\to c}$.

5.1.5 ICCD camera focus

The fluorescence signal collected from the trapped atoms is typically very low due to the small number of atoms, and if this signal is distributed over more than a few pixels of the ICCD due to poor focussing it can become undetectable. In order to ensure that the ICCD camera was positioned at the correct point at which the collected fluorescence from the dipole trap was maximally focussed on the detector, measurements of the size of the dipole trap image were taken at various positions of the camera along the imaging axis. The optimal position for the camera is taken as that which achieves the smallest and sharpest image of the trap.

In this chapter, both the size of the dipole-trapping beam and trapped atom cloud at the beam focus position are discussed, which are distinct sizes but both measured by 2D Gaussian fitting to camera images. The trapping beam size will be denoted by the standard deviation of the Gaussian fit σ and beam waist $w = 2\sigma$, and the atom cloud size will be denoted by σ_T and diameter $w_T = 2\sigma_T$. In both cases, the fitting to the image is done to obtain the size along two perpendicular axes in the imaging plane, which may either be the major and minor axes, denoted by σ_1, σ_2 for the beam and σ_{T1}, σ_{T2} for the atom cloud, or the horizontal and vertical axes, denoted by σ_H, σ_V and σ_{TH}, σ_{TV}. This is demonstrated in Figure 5.6.

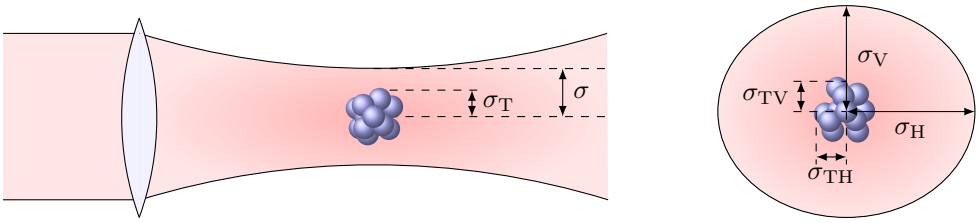

Figure 5.6: Diagram of the dipole trap consisting of a cloud of atoms confined at the focus of the trapping beam, showing the naming convention used for the measured sizes of the beam waist and atom cloud. The values of σ and σ_T represent the standard deviation of a 2D Gaussian profile fit to acquired camera images of the beam and atom cloud respectively.

The ICCD camera is typically mounted on a mechanical mount capable of 10 μm-resolution adjustment in the x and z axes, where the z axis is the imaging axis and the x axis is horizontal and perpendicular to the z axis. This mount only allows a 2 cm range of adjustment along the z axis, so the focus position was first obtained roughly using a Marlin F033B CCD camera before placing the ICCD camera in the vicinity of the focus point and performing a more precise measurement of the optimal position. Images of the trap were obtained for 31 different positions of the ICCD camera along the z axis, taken in 0.5 mm increments of the micrometer scale adjustment from 0.0 to 15.0 mm. At each position, 200 images of the dipole trapped atoms in the MOT were captured and averaged, and background-corrected by subtracting an average of 200 images of the MOT background. A 2D Gaussian fit of the resulting averaged image was done in MATLAB, and the standard deviations σ_{T1}, σ_{T2} of the Gaussian fit along the major and minor axes respectively were extracted as a measure of the size of the atom cloud.

The results of the measurement are shown in Figure 5.7, showing the averaged standard deviation $\bar{\sigma}_T = (\sigma_{T1} + \sigma_{T2})/2$ and amplitude in pixel counts as a

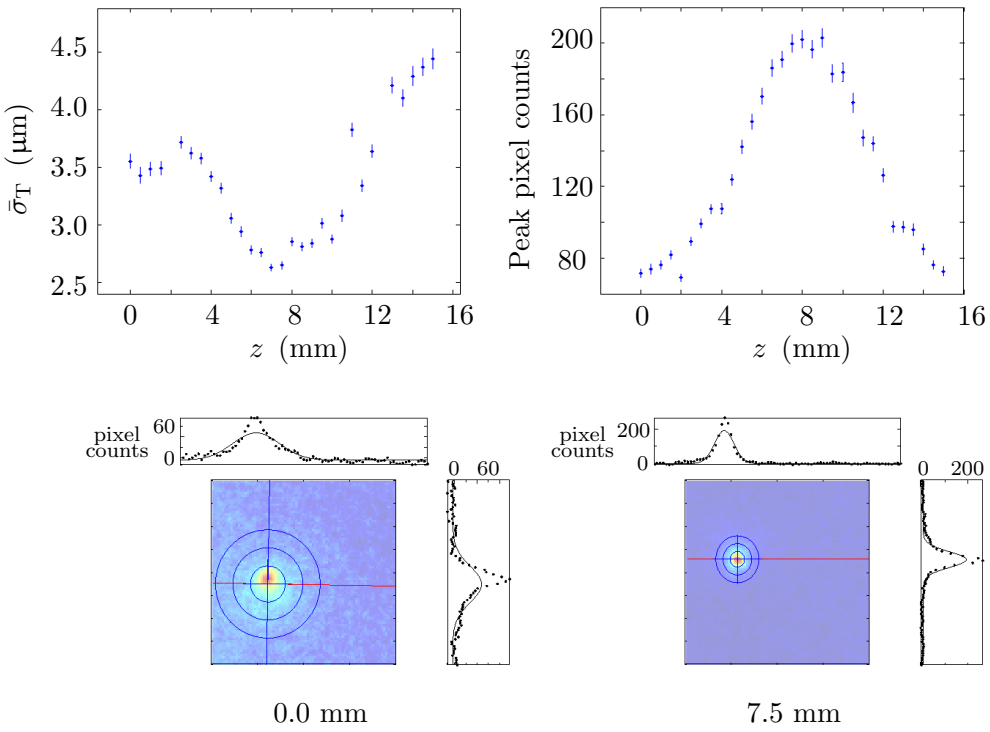

Figure 5.7: Size and amplitude of the dipole trap imaged on the ICCD camera with position z along the imaging axis, to determine the optimal camera position. The zero point $z = 0$ mm is arbitrary and simply represents the end of the micrometer-scale adjustable mount. The size $\bar{\sigma}_T$ is the average of the horizontal and vertical standard deviations resulting from a 2D Gaussian fit to the image of the trap. The fitted images at positions 0.0 mm and 7.5 mm are shown beneath the plots.

function of the camera position. It can be seen that the maximum counts detected from the trap and minimum size occurred at a slightly separated position, so the position of the ICCD camera was set to 7.5 mm as a compromise. The resulting size of the trapped atom cloud at this position was measured to be $\bar{\sigma}_{\mathrm{T}} = (1.6 \pm 0.7)$ µm using the Marlin CCD camera and $\bar{\sigma}_{\mathrm{T}} = (2.6 \pm 1.7)$ µm using the ICCD camera, where the uncertainty for both values arises from the resolution limit imposed by the pixel size. The larger uncertainty measured with the ICCD is due to a difference in resolution between the two camera models, as the Marlin CCD camera has a pixel size of 9.9 µm and the ICCD camera has a pixel size of 14 µm and minimum resolution limited by the intensifier of 25 µm. Therefore the blurring caused by the intensifier results in the image being spread over more pixels in the ICCD image. The sizes measured by both the Marlin and ICCD cameras are larger than the expected value, as the trapping beam was prepared for an estimated beam waist $w = 2\sigma$ at the trap position of 2 µm to produce a trapped atom cloud diameter of $2\sigma_{\mathrm{T}} \sim 1$ µm for typical temperatures. This would correspond to a cloud size of $\sigma_{\mathrm{T}} \sim 0.5$ µm, which is outside the uncertainty of the atom cloud size measured by the cameras. The size of the trap is measured and discussed further in section 5.2.1.

5.1.6 ICCD trigger timing

Experiments involving imaging of the fluorescence from the dipole-trapped atoms can require operation on very short time scales. Measurements for the characterisation of trap properties such as temperature involve recording snapshots of the fluorescence while the atoms are expanding freely in space, so

camera exposure times on the order of tens of μs are required. The intensifier gain supplied by the ICCD is designed to allow an appreciable signal to be acquired with such small amounts of light reaching the detector in these situations. On these timescales, the delay introduced electronically between sending a signal to trigger the camera and the beginning of imaging becomes significant, so the trigger delay was measured.

The camera sends a monitor output for the 'arm' and 'fire' pulses during triggering. The arm signal indicates the time at which a trigger has been received, at which point the signal falls from 5 V to 0 V for the duration of exposure and readout to indicate when the camera is ready to accept another external trigger. The fire signal indicates when exposure has started. The time delay Δt_1 between sending the initial trigger signal and the arm pulse and the delay Δt_2 between the initial trigger and the fire pulse were measured every 12 s for four minutes at each of the different readout rate settings of the ICCD, being 50 kHz, 1 MHz, 3 MHz, and 5 MHz. The value of Δt_2 is assumed to be the total delay between sending the trigger to the camera and the beginning of image acquisition. The results are displayed in Figure 5.8 for 50 kHz, showing two of the obtained oscilloscope scans during the measurement on the left hand side of the figure, corresponding to the minimum and maximum total delays Δt_2 respectively. The right side of the figure displays the entire range of results, showing Δt_1 (represented by the blue line) oscillating between 0 μs and $\sim$ 30 μs throughout the duration of the measurement. The delay between the arm and fire pulses $\Delta t_2 - \Delta t_1$ (green line) is constant at $\sim$ 60 μs, leading to a total trigger delay time Δt_2 (purple line) oscillating between $\sim$ 60 μs and $\sim$ 90 μs. Therefore for experiments involving

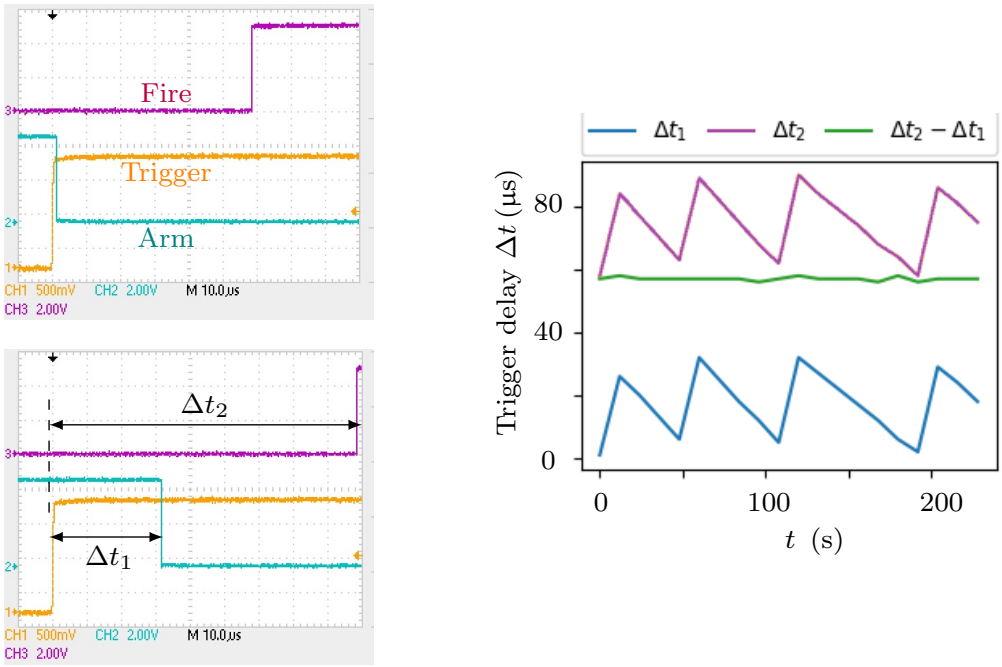

Figure 5.8: Measured trigger delay of the ICCD camera. On the left, oscilloscope scans displaying the timing of the trigger (yellow), arm (turquoise) and fire (purple) pulses are shown for two cases with a varying delay between the trigger and arm pulse. The right-hand plot shows the results of repeated measurements of the trigger delay every 12 s for 4 minutes, with Δt_1 the separation between the trigger and arm pulses and Δt_2 the total trigger delay, being the separation between the trigger and fire pulses.

imaging the dipole trap on small timescales[1], a constant delay stage of 90 µs was included between sending the trigger to the ICCD and beginning the imaging flash to ensure that the camera exposure had started. The exposure time of the camera was set to 30 µs longer than the imaging flash time for these experiments, to account for the 30 µs uncertainty in the total trigger delay time.

In the following section, measurements taken to characterise the properties of the dipole trap and confined atom cloud in the trap are described, along with a

[1]Namely the measurement of atom number and light shift in section 5.2.2 and the measurement of temperature in section 5.2.3.

presentation and discussion of the results obtained. Measured properties of the trap include the size, number of atoms, light shift induced by the trapping beam, temperature and lifetime of the atoms.

5.2 Characterisation of the Dipole Trap

As with the MOT, it is of high importance that the physical characteristics of the dipole trap are investigated, as an understanding of the trap properties will inform future experimental procedures involving the trapped atoms. In particular, for applications in quantum computational protocols which exploit the Rydberg blockade to implement quantum logic gates, it is important to ensure the size of a single trap can be contained within a single blockade radius. Knowledge of the number of atoms in the trap is also critical as this affects the rate of Rabi oscillations resulting from coupling to the radiation field [74], which affects the duration of laser pulses used to transfer population into different states, for example using STIRAP [77, 102, 103]. It is also important to achieve a trap lifetime long enough to prevent atom loss during the experimental timescales of such an implementation, which also depends on obtaining a trap depth appropriate for storing enough atoms at a given temperature. Furthermore, different regimes of the number density of atoms in the trap can introduce varying collisional dynamics which affect the lifetime of the trap. These are just some of the reasons why the trap properties must be known for the application of quantum information using atoms. This section details the experimental measurements carried out for the characterisation of the trap properties, including the size and

density of the trap, the number of trapped atoms achievable, the trap depth, the temperature of the atoms, and the lifetime of the trap in the absence of loading from the MOT.

5.2.1 Size

Knowledge of the size of the dipole trap is vital when considering applications that rely on Rydberg interactions, such as DQC1 and similar atom-based quantum information processing protocols. This is because the size of the trap must be small enough for the atoms to be contained within one Rydberg blockade radius, allowing them to be prepared in a single excited collective Rydberg state. This is also a requirement for a separate nearby trap to be blockaded by the first trap, provided the second trap is also small enough and in close proximity to the first trap, which is required for the quantum gate described in section 2.4.6 to operate. In section 2.4.4 it was shown how the blockade radius may be calculated for a certain highly excited state given the transition linewidth, using equation 2.15. Examples of blockade radii for $n = 42 - 60$ give results in the range of $3 - 8$ μm [59, 63, 65]. In section 6.1.3 the blockade radius is calculated as $R_b \sim 4.4$ μm based on the linewidth of the Autler-Townes splitting feature observed while probing Rydberg states using a two-photon transition in the laboratory, assuming an achievable excited state with $n \sim 60$. This sets a target for the diameter of the dipole trapped cloud of atoms of $\lesssim 1$ μm, allowing one to two traps close together to be within a single blockade radius. This is achievable with a trapping beam waist of $\lesssim 2$ μm, as the confined atoms occupy a smaller volume within the trap depending on their temperature.

The size of the trapping potential can be estimated by measuring the shape of the profile of the beam itself, by focussing the beam after it exits the vacuum chamber and imaging the beam shape in the vicinity of the focus point. This can be used along with knowledge of the beam power and temperature of the atoms to predict the size of the trapped atom cloud. Alternatively, the size can be measured more directly by simply imaging the fluorescence from the trapped atoms with a camera.

Measurement of the beam profile was done by focussing the dipole laser exiting the chamber onto a Marlin CCD camera using a 250 mm-focal length plano-convex lens. A neutral density filter was fitted to the front of the camera to reduce the incident beam power and prevent the CCD from being oversaturated and damaged. One image was captured for each camera position for a range of 32 positions from 85 mm to 295 mm away from the lens. For each image the size of the beam was obtained from 2D Gaussian fitting done in MATLAB, giving the horizontal and vertical standard deviations of the fitted Gaussian distribution, σ_{H} and σ_{V}, as well as the amplitude of the distribution in pixel counts, as required for an estimation of the peak intensity at the trap position. From this data the 3D profile of the trapping beam at the trap position inside the chamber was reconstructed by extrapolating the geometric light path back through the chamber and high-NA lenses. The resulting beam size and amplitude are displayed in Figure 5.9 (a) in terms of the distance along the optical axis[2] away from the focal point of the focussing lenses. It can be seen from the results that the foci of the beam in the horizontal and vertical planes are not in the

[2]The optical axis is the horizontal axis in the direction of the propagation of the dipole trapping beam, orthogonal to σ_{H} and σ_{V}.

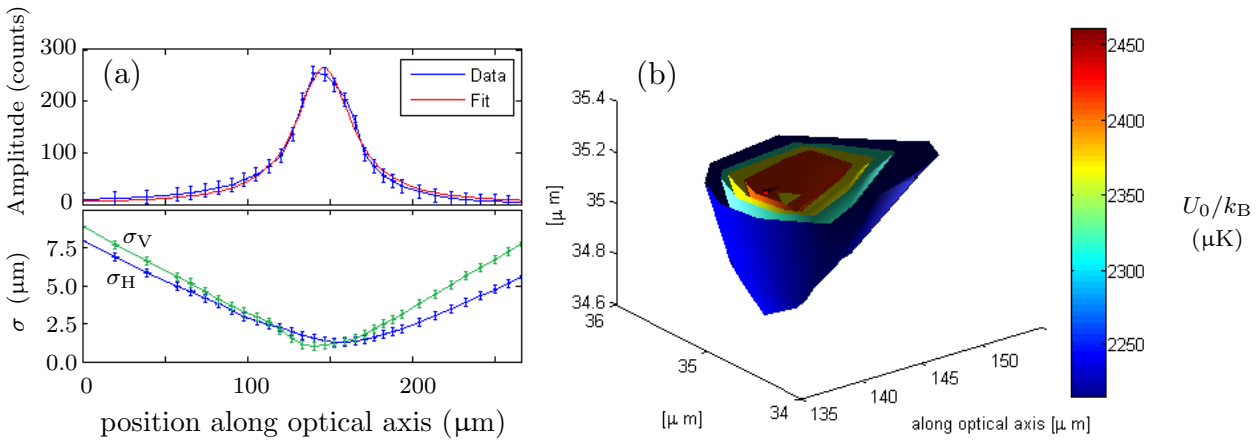

Figure 5.9: Reconstruction of the 3D profile of the dipole trapping beam at the trap position. The plot in (a) shows the vertical and horizontal standard deviations σ_H, σ_V of the beam from 2D Gaussian fitting, and amplitude in pixel counts along the imaging axis. The amplitude is fit to with a Lorentzian function. The zero position is arbitrarily located at the first data point. In (b), a 3D representation of the spatially-dependent trap depth is shown.

same place, being separated by roughly 20 μm, which means that the collimation angle of the incoming beam is slightly different in the horizontal and vertical planes. However this was not deemed to be a serious issue requiring resetting of the prisms and collimating lenses. The beam waists in the horizontal and vertical directions were found to be $w_H = (3.02 \pm 0.02)$ μm and $w_V = (2.07 \pm 0.01)$ μm respectively, where $w_{H,V} = 2\sigma_{H,V}$. The uncertainty on the beam waists is derived from the root-mean-square error on the Gaussian fitting to the acquired images of the beam. The discrepancy between w_H and w_V also suggests that the collimation is uneven between the two axes. In section 5.1 it was explained that the size of the beam entering the chamber was chosen to produce a trap waist of 2 μm, small enough to operate as a microscopic trap for experiments in which a Rydberg blockade may extend over the entire trap diameter. The resulting w_H is larger than this by 1 μm, due to an imperfect setup of the

geometric parameters of the incoming beam, however this is not too large an increase in size and the production of a microscopic trapping volume was generally successful. A Lorentzian fit to the amplitude in pixel counts shown in Figure 5.9 (a) gives a HWHM of (20.6 ± 0.8) μm, representing the Rayleigh length of the beam. The theoretical Rayleigh length corresponding to the trap waist is $z_{\mathrm{R}} = \pi w^2/\lambda = (24 \pm 2)$ μm, where $w = (w_{\mathrm{H}} + w_{\mathrm{V}})/2$ is the average beam waist. The discrepancy between the theoretical Rayleigh length and that obtained from fitting is due to imperfections in the beam profile including differences in the focal point, collimation and waist between the two dimensions, so that the profile does not completely represent a perfect Gaussian beam.

Theoretical values for the size of the trapped cloud of atoms itself, as well as the trap depth U_0 and light shift induced by the beam Δ_{LS} may be calculated with knowledge of the 3D trap profile, laser power and the temperature of the trapped atoms. For a Gaussian trapping laser beam focussed by a lens, the intensity profile $I(r, z)$ in terms of the radial and axial coordinates r and z respectively is given by equation 3.32. Near the beam waist at the lens focus position, this is approximately cylindrically symmetrical in the axial direction [78]. At the beam waist $w_0 \equiv w(z = 0)$, this gives

$$I(r, 0) = I_0 \exp\left(-\frac{2r^2}{w_0^2}\right) \tag{5.2}$$

where the peak intensity $I_0 = 2P/\pi w_0^2$. As seen in equation 3.30, the dipole trapping potential $U_{\mathrm{dip}}(r, z)$ is proportional to the beam intensity profile.

Therefore the potential at the trap waist may be described by

$$U_{\mathrm{dip}}\left(r,0\right) \;=\; U_0 \exp\left(-\frac{2r^2}{w_0^2}\right) \tag{5.3}$$

where U_0 is the trap depth, given by [78]

$$U_0 \;=\; \frac{\hbar\Gamma^2 I_0}{8I_{\mathrm{sat}}}\left(\frac{1}{3\Delta_{1/2}}+\frac{2}{3\Delta_{3/2}}\right) \tag{5.4}$$

where $\Delta_{1/2}$ is the detuning of the dipole trapping beam from the $5^2\mathrm{S}_{1/2} \rightarrow 5^2\mathrm{P}_{1/2}$ transition frequency and $\Delta_{3/2}$ is the detuning from the $5^2\mathrm{S}_{1/2} \rightarrow 5^2\mathrm{P}_{3/2}$ transition frequency, being the D_1 and D_2 lines arising from the fine-structure splitting of the excited state. As the dipole trapping beam wavelength is 852 nm, it is far detuned from both the D_1 and D_2 lines, which correspond to approximately 795 nm and 780 nm respectively. Therefore the weighted average of hyperfine states can be used to simplify this calculation. This equation is used to obtain the trap depth following the measurement of the beam intensity profile done in this section.

The thermal density distribution of atoms confined in the trapping potential is determined by the Boltzmann distribution, and takes the form

$$\rho(r) \;=\; \rho_0 \exp\left(-\frac{U_{\mathrm{dip}}\left(r\right)}{k_{\mathrm{B}}T}\right) \tag{5.5}$$

where ρ_0 is the peak number density. As the trapping potential is approximately harmonic near the trap centre [84,101], this density distribution can be described by

$$\rho(r) \;=\; \rho_0 \exp\left(-\frac{x^2}{2\sigma_{\mathrm{T}x}^2}-\frac{y^2}{2\sigma_{\mathrm{T}y}^2}-\frac{z^2}{2\sigma_{\mathrm{T}z}^2}\right) \tag{5.6}$$

with $\sigma_{\mathrm{T}i}$ representing the standard deviation of the Gaussian density distribution of atoms in the trap in the $i = x, y, z$ axes. Relating this spatial distribution to the thermal distribution in equation 5.5 and trapping potential given in equation 5.3, along with knowledge of the trap depth and temperature of the atoms from a separate measurement, the size of the atom cloud $\sigma_{\mathrm{T}i}$ can be determined.

Assuming the atoms in the dipole trap are at a temperature of $T = (494 \pm 25)$ μK as measured directly in section 5.2.3, and using the known maximum beam power at the trap position of 80 mW, the size of the atom cloud in the horizontal and vertical planes is calculated to be $\sigma_{\mathrm{TH}} = (0.70 \pm 0.04)$ μm and $\sigma_{\mathrm{TV}} = (0.48 \pm 0.03)$ μm respectively, with a Lorentzian HWHM in the direction of the optical axis of $\sigma_{\mathrm{TL}} = (7.0 \pm 0.3)$ μm. The uncertainty on the atom cloud size is propagated forward from the uncertainty on the temperature of the atoms and the trap depth. The trap depth

$$\frac{U_0}{k_{\mathrm{B}}} = (2.46 \pm 0.03) \text{ mK} \tag{5.7}$$

and the corresponding light shift

$$\Delta_{\mathrm{LS}} = (51.2 \pm 0.6) \times 2\pi \text{ MHz}. \tag{5.8}$$

The light shift is relatively large, being around $8.4\,\Gamma$, due to the high power and small trapping volume leading to high intensity. The trapped atom cloud radii σ_{TH}, σ_{TV} measured in this section are found to be well within the calculated Rydberg blockade radius of ~ 4.4 μm which was set as the target upper limit for the size, in order to ensure that the trap can be contained within a single blockade

radius. However, the size along the imaging axis of $\sigma_{\mathrm{TL}} = (7.0 \pm 0.3)$ μm exceeds this blockade radius. The size of the atom cloud in this dimension could be reduced further by decreasing the temperature of the atoms or the trap depth, or by adjusting the dipole trap laser system to achieve a tighter focus. Therefore the set up of the dipole trapping laser system, including adjustment of the input trapping beam to obtain this size, is considered partially successful and the trap is close to fulfilling the size requirements for implementation as an atomic qubit.

The size of the dipole-trapped atom cloud can also be measured directly by imaging the fluorescence from the trap on a camera and fitting to the image, as demonstrated in section 5.1.5 and shown in Figure 5.7. These images display the size of the cloud in the plane of the imaging axis, plane-parallel to the high-NA trapping lens. Here, the cloud size was measured as $\bar{\sigma}_{\mathrm{T}} = (1.6 \pm 0.7)$ μm using the Marlin CCD camera corresponding to approximately two pixels, and (2.6 ± 1.7) μm using the ICCD camera with a larger uncertainty due to the minimum resolution limit set by the intensifier. The large uncertainties on these values arise from the acquired image of the trap being close to the pixel size or resolution limit. The atom cloud size measured by both the Marlin CCD camera and ICCD camera is larger than the predicted size of $\bar{\sigma}_{\mathrm{T}} = (\sigma_{\mathrm{TH}} + \sigma_{\mathrm{TV}})/2 = (0.59 \pm 0.04)$ μm, being outside error, which can be attributed to a combination of the resolution limit of the camera, the point spread function associated with the optical path, the displacement of the trap from the high-NA lens focal point and uncertainty in the focus position of the camera. For this reason the values of σ_{TH} and σ_{TV} predicted from the measured trapping beam profile are taken as the most reliable result for the trap size.

It is useful to obtain a measure of the volume of the dipole trap, which can be used with the measured number of atoms in the trap to determine the atom number density. This quantity is important when considering dynamic effects such as collisional losses in the trap, which affects the trap lifetime and is discussed in further detail in section 5.2.4. The estimated volume of the trapped atoms is calculated as

$$V = (2\pi)^{\frac{3}{2}} \sigma_{\mathrm{TH}} \sigma_{\mathrm{TV}} \sigma_{\mathrm{TL}}, \tag{5.9}$$

which results in a volume of $V = (38 \pm 4)\ \mu\mathrm{m}^3$ for the trap size predicted in this section. Following this, the peak density ρ_0 of a trap containing N atoms is given by $\rho_0 = N/V$.

5.2.2 Atom number and Stark shift

In section 4.3.1 it was demonstrated how the number of atoms in the MOT could be measured by acquiring the fluorescence emitted by the MOT using a photodiode. In the case of the dipole trap, the fluorescence signal is likely to be far too small to be resolved from other light sources using a photodiode. This can be solved by using a highly sensitive photon-multiplying device such as an avalanche photodiode (APD), provided the external light such as fluorescence from the MOT atoms or from the lasers is properly removed, for example by focussing the light from the dipole trap through a pinhole or optic fibre [78, 104]. Alternatively the number of atoms can be measured using a sensitive camera image of the trap, and either fitting to the 2D Gaussian profile of the trap and extracting the volume and amplitude, or simply integrating the pixel counts in

the image. The number of trapped atoms can be derived from the acquired pixel counts using equation 5.1, obtained from the calibration of the ICCD camera in section 5.1.4.

For the fluorescence imaging of the dipole trap, the cooling beams for the MOT are tuned near to resonance and used as probe beams. Because a high intensity beam is used for dipole trapping, there is likely to be a significant Stark shift in the energy levels of the trapped atoms, causing a subsequent relative detuning of the probe beams from resonance. This effect can be avoided by simply removing the dipole beam and imaging the atoms before they have time to escape the imaging area. However it is useful to measure the Stark shift induced by the trapping beam for different beam powers as it is related to the trap depth, an important physical property of the trap, and the results can be compared to the theoretical prediction from section 5.2.1 to test the validity of the prediction.

As the light shift causes a relative detuning between the probe beam frequency and the resonant transition frequency of the atoms, the number of photons emitted by the atoms as fluorescence is decreased, being proportional to the scattering rate $R_{\mathrm{LS}}(\Delta_{\mathrm{LS}})$ in equation 3.1 with Δ_{LS} being the light shift. One method for measuring the light shift experimentally is to compare the fluorescence signal obtained by imaging the trapped atoms both in the presence and absence of the light shift. In the latter case, $\Delta = 0$ and the scattering rate reduces to $R = \Gamma/2$ assuming the probe beam is of high intensity compared to the saturation intensity. Assuming the ratio between the total fluorescence signal without and with light shift $r = R/R_{\mathrm{LS}}$, where R_{LS} is the scattering rate in the

presence of the light shift, and rearranging, we get

$$\Delta_{\mathrm{LS}} = \frac{\Gamma}{2}\sqrt{(r-1)\cdot(I/I_{\mathrm{sat}})}. \tag{5.10}$$

This r is the correction factor that appears in equation 5.1, allowing the number of atoms to be obtained for a known light shift Δ_{LS}.

The experimental sequence for the measurement of the atom number and light shift in the dipole trap is as follows: first the MOT is loaded for 5 seconds with a cooling beam detuning of $-2\,\Gamma$ and power of $\sim 30\,I/I_{\mathrm{sat}}$. The total repump beam power is 3.5 mW and the trapping B field is driven by a coil current of 3.6 A, producing a field gradient of $\sim$ 15 $\mathrm{G\,cm^{-1}}$. The dipole trap is loaded with a dipole trap laser power of 80 mW. Following this the MOT lasers and trapping field are switched off for 20 ms to remove the background MOT atoms. During this stage the cooling/probe beam detuning is ramped linearly to $-0.2\,\Gamma$ and the dipole trapping beam power is simultaneously ramped to a variable final power P_{f}. The ICCD camera is then triggered 90 µs before the trap is imaged with a 50 µs flash of the MOT beams, obtaining an image of the trap with a light shift induced by the P_{f}-power dipole beam. The ICCD camera is triggered 90 µs before the start of the imaging flash to account for the trigger delay which has an upper bound of 90 µs as measured in section 5.1.6. This process is then repeated but with the dipole beam switched off at the beginning of the 50 µs imaging flash, obtaining an image of the trap without light shift. Finally there is a 2 s waiting stage with all lasers switched off to allow time for the readout and re-arming of the ICCD camera trigger, and to ensure no more atoms are trapped, before a background image is captured including any noise and stray light. For

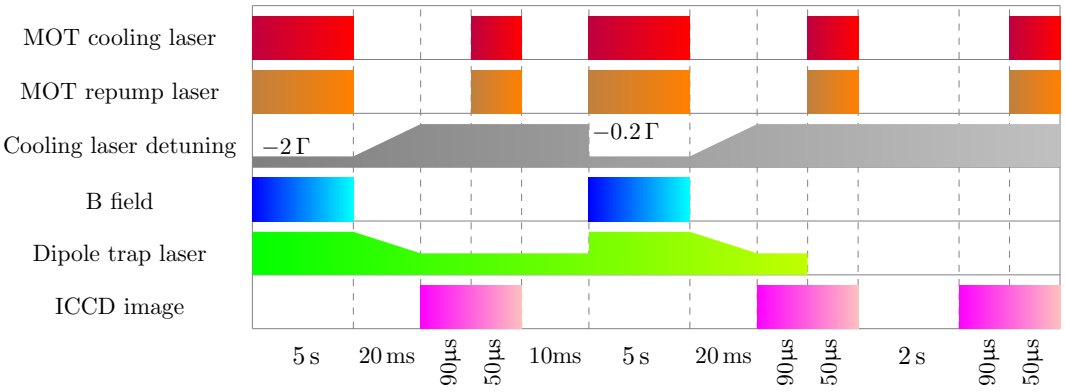

Figure 5.10: Diagram showing the experimental sequence for the measurement of the number of atoms in the dipole trap and the light shift induced by the trapping beam. First the MOT is loaded for 5 s at a laser detuning $\Delta = -2\,\Gamma$, cooling beam power $\sim 30\,I/I_{\mathrm{sat}}$, total repump beam power 3.5 mW, trapping field coil current 3.6 A and dipole trap laser power 80 mW. The trap is switched off for 20 ms allowing time for the MOT atoms to be removed from the imaging area, during which the cooling beam detuning is ramped to $-0.2\,\Gamma$ and the dipole beam is ramped to a variable final power P_{f}. The ICCD camera is triggered for 90 µs to account for the trigger delay before using a 50 µs flash of the MOT lasers to image the dipole trap. A second image is taken with the dipole beam switched off at the beginning of the imaging flash to remove the light shift. A final third image is taken without loading the MOT or dipole trap to obtain a background image for correction. The camera exposure time is 50 µs.

this experimental sequence the dipole trap is loaded with a full power beam then ramped to the final power in order to ensure that a measurable number of atoms is initially loaded, as during preliminary testing it was found that attempting to load the trap with a low power beam resulted in a barely detectable amount of fluorescence from the trapped atoms. This is attributed to a relaxation of the trap depth caused by the lower power trapping beam, allowing fewer atoms to be trapped. The ramping time is 20 ms, and the ramping also occurs for the background image with no trap loaded for consistency. The experimental sequence is displayed in Figure 5.10.

The measurement of the number of atoms and the light shift was carried out for

a range of 11 different dipole beam powers P_{f} from 30 mW to 80 mW. The ICCD camera was set up with an exposure time of 80 µs to record the 50 µs imaging flash while allowing for a 30 µs uncertainty in the camera trigger delay. A gain factor of 20 was applied using the intensifier to boost the acquired fluorescence signal. For each beam power P_{f} the dipole trap image was formed from the average of 200 images, corrected by an averaged background image. For each P_{f} the ratio r between the acquired fluorescence with and without light shift was obtained, from which the light shift Δ_{LS} and number of atoms N_{DT} were calculated using equations 5.10 and 5.1 respectively. The results are displayed in Figure 5.11, showing the expected correlation between the induced light shift and beam power. All the data for beam powers below 65 mW show a higher value of light shift than expected, being outside error of the theoretical prediction. This suggests the presence of some source of systematic error in the experimental method, leading to larger-than-expected values of the correction factor r. However the measured light shift of $(48 \pm 5) \times 2\pi$ MHz at the full power of 80 mW is reliable, agreeing well with the theoretical value of $\Delta_{\mathrm{LS}} = (51.2 \pm 0.6) \times 2\pi$ MHz, and is used in the calculation of the number of atoms imaged in the full power beam during the characterisation of the dipole trap lifetime in section 5.2.4.

The average number of atoms measured for the different beam powers is displayed in Figure 5.11 (b), showing that typically between 29 and 42 atoms are trapped. The data is taken from only the images of the released trap after the beam had been switched off, so no light shift is present. As with the results for the measurement of the induced light shift, each data point is obtained from the average of 200 images of the dipole-trapped atom cloud. The large fluctuation in

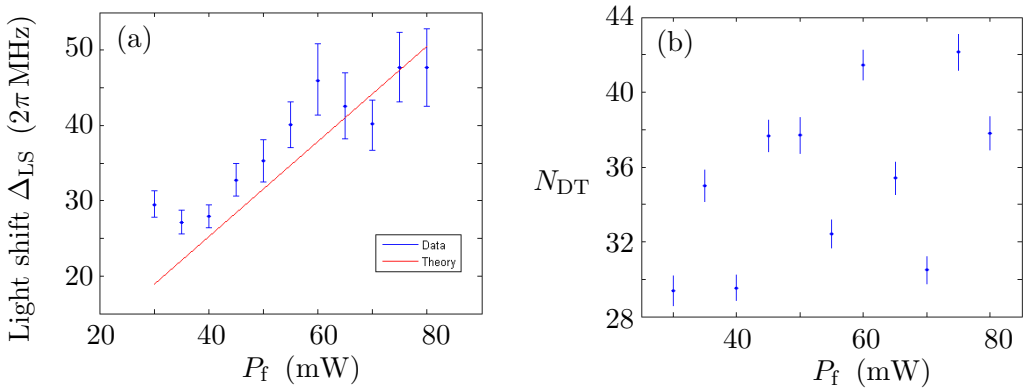

Figure 5.11: Results of the dipole trap light shift and number of atoms measurement. In (a), the light shift induced by the trapping beam is shown for a range of beam powers P_f. The blue points represent experimental data and the red line shows the theoretical prediction derived from the measured trapping beam profile. In (b), the experimentally measured number of atoms in the dipole trap N_{DT} is displayed for various beam powers.

atom number between beam powers is due to the data being taken out of order throughout the day, during which the background rubidium vapour was gradually increasing from the continuous running of the dispenser, leading to a greater number of atoms being loaded in both the MOT and dipole trap. It is expected that the atom number should increase with higher beam power as the trap depth becomes deeper, allowing a larger part of the atomic velocity distribution to be trapped. However, due to the fluctuation caused by differing levels of background rubidium vapour, the relationship between atom number and beam power cannot be accurately extracted. This method could be improved to obtain a better measurement of this relationship by implementing an experimental sequence which alternates between beam powers for each repetition of the sequence, instead of acquiring all the data for each different beam power in turn. This would reduce the dependence of the results on the time of day at which they were taken. The number of atoms trapped is reasonable and within expectations for a trap of

this size, as microscopic traps have been shown to typically trap $\sim 1 - 100$ atoms [105–108].

5.2.3 Temperature

In section 4.3.1, it was demonstrated that the temperature of the atoms in the MOT could be measured using the well known time-of-flight (TOF) method, in which the atoms are released from the trap and allowed to escape at their thermal velocity. Imaging of the fluorescence emitted by the atoms can be used to obtain a measure of the size of the expanding atom cloud with time, which can be related to the Maxwell-Boltzmann velocity distribution of the atoms from which their temperature can be extracted. The same principle can be applied to measure the temperature of the dipole-trapped atoms, by switching off the trapping beam and observing the subsequent thermal expansion of the atoms. Whereas the Marlin CCD camera was used to obtain images of the MOT from which the size could be extracted by 2-dimensional Gaussian fitting, in the case of the dipole trap the dipole trap imaging system and Andor ICCD camera are used instead, to accommodate the fact that the dipole trap is much smaller than the MOT and emits a far weaker fluorescence signal. The width of the cloud of dipole-trapped atoms after being released is again described by equation 4.11, although the size of the cloud $\sigma(dt)$ and time-of-flight dt are typically on the order of μm and μs respectively, rather than mm and ms as for the MOT.

The experimental sequence for the temperature measurement of the dipole trap is as follows: first the MOT is loaded for 10 seconds with a cooling beam detuning of $-1.4\,\Gamma$ and power of $\sim 30\,I/I_{\mathrm{sat}}$. The total repump beam power is 3.5 mW and

the trapping B field is driven by a coil current of 3.6 A. The dipole trap is loaded with a laser power of 80 mW. The MOT beams and field are then switched off for 20 ms to remove the MOT atoms from the imaging area so that they do not obscure or interfere with the dipole trap image, during which the cooling beam detuning is ramped linearly from $-1.4\,\Gamma$ to $0\,\Gamma$. The ICCD camera is then triggered 90 µs $- dt$ before switching off the dipole trapping beam and allowing the trapped atoms to expand in space for a time dt. The trap is then imaged with a 50 µs flash of the MOT beams. The timing of the ICCD trigger is deliberately set up to ensure that it is always 90 µs before the start of the imaging flash, to account for the trigger delay which has an upper bound of 90 µs as measured in section 5.1.6. Following this is a 2-second waiting stage to allow time for the camera readout to finish and for the trigger to re-arm, as well as ensuring no atoms are left in the imaging area. The imaging is then repeated to obtain a background image including noise and any scattered light from the beams. The experimental sequence for the dipole trap time-of-flight measurement is displayed in Figure 5.12.

The time-of-flight measurement was carried out using a range of 13 dt values from 0 to 80 µs. The ICCD camera was set up with an exposure time of 80 µs to record the 50 µs imaging flash while allowing for a 30 µs uncertainty in the camera trigger delay. A gain factor of 20 was applied using the intensifier to boost the acquired fluorescence signal. The results are displayed in Figure 5.13, showing a linear relationship between σ_{av}^2 and dt^2 as expected according to equation 4.11. Due to the relatively large imaging time of 50 µs in comparison to the range of dt values, data points were plotted with a 25 µs offset along the x-axis, as the size of

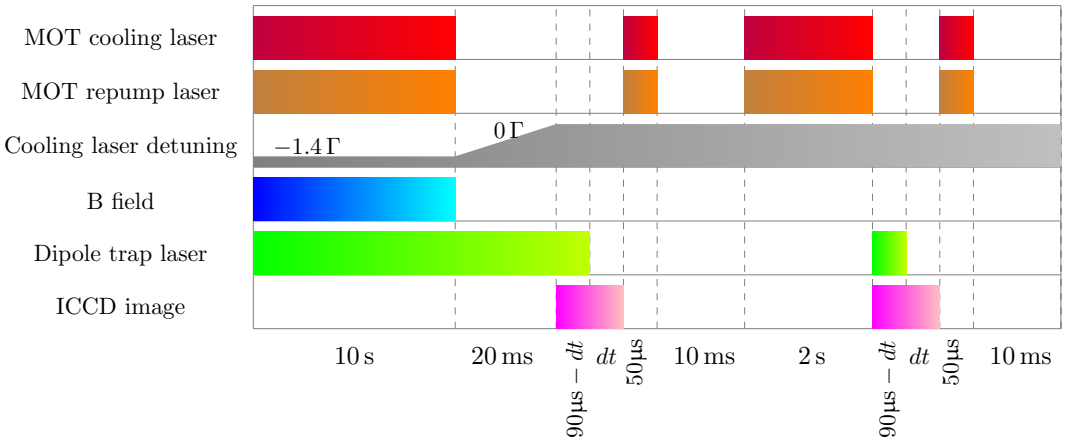

Figure 5.12: Diagram showing the experimental sequence for the measurement of the dipole trap temperature using the time-of-flight (TOF) method. First the MOT is loaded for 10 s at a laser detuning $\Delta = -1.4\,\Gamma$, cooling beam power $\sim 30\,I/I_{\mathrm{sat}}$, total repump beam power 3.5 mW, trapping field coil current 3.6 A and dipole trap laser power 80 mW. The trap is switched off for 20 ms allowing time for the MOT atoms to be removed from the imaging area. The ICCD camera is triggered 90 µs $-$ dt before switching off the dipole laser to account for the trigger delay before exposure begins. The dipole trapped atoms are allowed to disperse for a time dt before fluorescence imaging using a 50 µs flash of the MOT lasers. A second image is taken without loading the MOT or dipole trap to obtain a background image for correction. The camera exposure time is 50 µs.

the cloud measured at time dt actually represents the average cloud size between dt and dt + 50 µs and should therefore be plotted at dt + 25 µs. Linear fitting of the model given in equation 4.11 to the data was done in MATLAB and the temperature of the atoms was derived from the gradient of the resulting fit, giving $T = (494 \pm 25)$ µK. The 2D Gaussian fits to averaged ICCD images for each dt value displayed beneath the plot show a roughly isotropic thermal expansion of the atom cloud. For these images the spatial distribution of the atoms is well approximated by the Gaussian fitting. The temperature value obtained is very close to the measured temperature of the MOT atoms in section 4.3.1, $T_{\mathrm{MOT}} = (500 \pm 63)$ µK, being within error. This is in contrast to the expected temperature for atoms in the dipole trap, which is assumed to be lower than that for the MOT due to the much shallower dipole trap depth of $\sim$ 2.5 mK compared to typical MOT trap depths in the range of $\sim$ 1 K. However, as the MOT and dipole trap temperature measurements were taken some time apart, the MOT atoms may have been at a significantly different temperature from that presented in section 4.3.1 at the time of the dipole trap temperature measurement. This is likely to be caused by the general day-to-day alignment of the MOT beams, which is done to optimise and tune the MOT for different applications, leading to a variation in characteristic properties such as temperature over time. Therefore, the two temperature measurements cannot be compared in this instance. An improvement to the method for potential measurements in the future would be to perform a measurement of the temperature of both the MOT and dipole trap simultaneously for comparison. Also, the method may be improved by using a shorter camera exposure time for the imaging of the atoms while compensating for the decreased fluorescence signal acquired by increasing the intensifier gain. This

is due to the fact that the exposure time used was significantly large compared to the time separation between the data points.

As the first data point represents an average size of the atom cloud as it expands during the 50 µs-long imaging flash, it is not an accurate measurement of the size of the cloud at $dt = 0$ µs at the point when the dipole trapping beam is instantaneously switched off. The linear fit can be extrapolated to find the y-axis intercept, which gives an initial size of $\sigma_0 = (4.7 \pm 1.7)$ µm. This is larger than the apparent value of $\sim (2.6 \pm 1.7)$ µm measured by the ICCD in section 5.2.1, in which the atom cloud was imaged during continuous operation of the trapping beam. The cause of this is not clear; one possible reason may be an underestimation of the ICCD camera trigger delay, which would lead to the camera exposure at $dt = 0$ µs beginning after the atom cloud had already begun expanding, causing an offset in the x-axis of Figure 5.13 and an overestimate of the y-axis offset. The measurement of trigger delay in section 5.1.6 relied on the electronic monitor output signals for the trigger, arm and fire pulses being a reliable measurement of the trigger delay, so this explanation would require additional delays introduced elsewhere in the signal chain. Another explanation may be a delay in the switching-on of the imaging beams, which again would result in fluorescence being collected from trap only after it had begun expanding, although the AOMs used for the switching of the beams are assumed to operate on very fast timescales, with rise times on the order of tens of nanoseconds. Assuming the trap is initially at the apparent size of ~ 2.6 µm measured on the ICCD camera in section 5.2.1, a delay of 18 µs would be required for the trap to reach the size of 4.7 µm corresponding to $dt = 0$ µs in the TOF measurement,

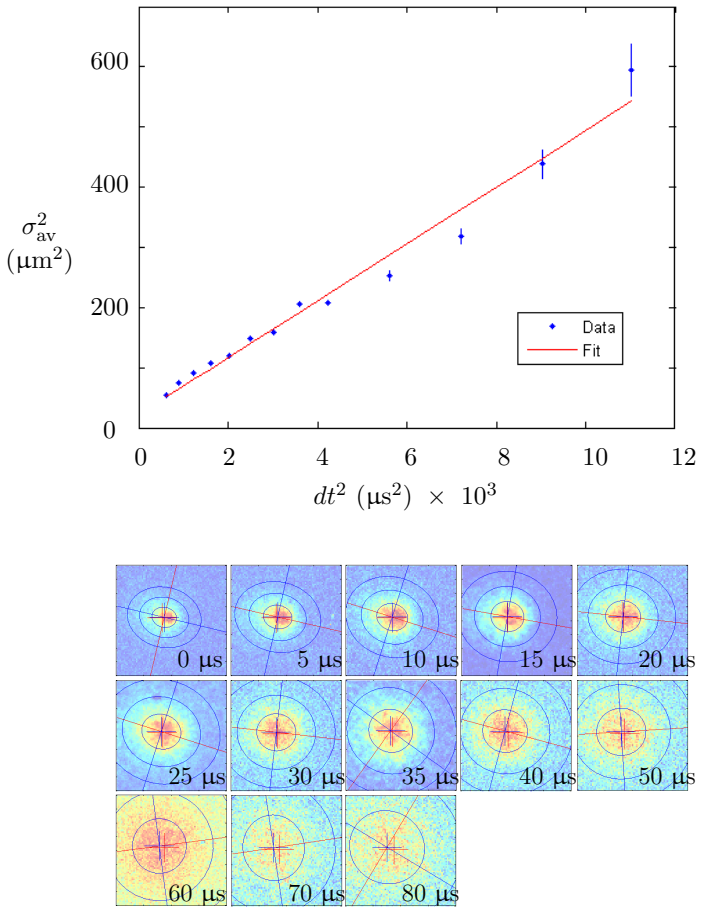

Figure 5.13: Experimental data for the time-of-flight (TOF) method for measurement of the dipole trap temperature, showing the size of the cloud derived from 2D Gaussian fitting, σ_{av}, as a function of the time of flight dt. The experimental data is represented by the blue data points along with error bars. Linear fitting to the data based on equation 4.11 was done in MATLAB and represented by the red line, corresponding to a measurement of $T = (494 \pm 25)$ µK for the dipole-trapped atoms. The 2D Gaussian-fitted images for each data point are displayed beneath the plot.

being significantly greater than the assumed delay introduced by the AOMs. This discrepancy does not affect the reliability of the temperature measurement, as the temperature may still be derived from the rate of expansion of the atoms with time, regardless of the initial size.

5.2.4 Lifetime

The lifetime of the dipole trap is an important property which describes the rate at which atoms are lost from the trap in the absence of loading. After the removal of the background MOT reservoir, atoms are no longer being loaded and it is important to understand what is happening to the number of atoms in the dipole trap with time. The depopulation of the trap is a complex process which can include several different loss mechanisms depending on the parameters of the trap, and characterisation of the trap lifetime can give insight into how to tune these parameters to optimise the trap for a given application.

The evolution of the number of atoms in the dipole trap over time can be described by the same rate equation that governs the loading and losses of atoms in the MOT, given by equation 4.1, with an additional term β added to characterise two-body losses caused by collisions between the trapped atoms rather than with the background vapour. These two-body collisional losses could be ignored in the case of the MOT due to its relatively lower density compared to the dipole trap. Therefore the number of atoms $N(t)$ contained in the dipole trap at time t can be described by the following rate equation [109–114],

$$\frac{dN(t)}{dt} = R - \gamma N - \beta N(N - 1), \tag{5.11}$$

where R is the loading rate of atoms into the trap from a background reservoir, γ is the loss rate of atoms by collisions with the background vapour, henceforth referred to as single-body losses, and β is the loss rate by two-body collisions between pairs of atoms within the trap. The $N(N-1)$ term stems from the fact that a single two-body collision results in a pair of atoms being ejected from the trap. All three loading and loss rate parameters R, γ, β have the units s^{-1}.

In the absence of a background reservoir of MOT atoms, the loading rate R can be equated to zero and the resulting rate equation is therefore

$$\frac{dN(t)}{dt} = -\gamma N - \beta N(N-1). \tag{5.12}$$

The solution to this equation is given by

$$N(t) = \frac{A(\gamma - \beta)}{e^{(\gamma - \beta)t} - A\beta}, \tag{5.13}$$

where A arises from the constant of integration and is related to the initial number of atoms in the trap, $N_0 \equiv N(0)$, by $N_0 = A(\gamma - \beta)/1 - A\beta$. The three parameters A, γ and β can be determined by performing a measurement of the number of atoms in the trap at various times t after removing the MOT background and fitting to the resultant data with equation 5.13.

Experimental Procedure and Results

For this experiment the number of atoms in the dipole trap $N(t)$ was measured by imaging the trap using the ICCD camera as described in section 5.2.2. The

number of atoms was measured for a range of 22 different delay times from 1 to 5000 ms after switching off the MOT trapping lasers and confining magnetic field in order to remove the background MOT atoms. For each t, 50 images of the trap were captured and used to create a single averaged image. An average of 50 background images was subtracted from this and the number of atoms was derived by evaluating the total sum of the pixel counts in the resulting image and using equation 5.1. A camera exposure time of 1 ms was used, with a gain factor of 20 applied using the intensifier. In this case the camera exposure time was long compared to the ICCD trigger delay of 30 μs so the camera was triggered at the same time as the start of the imaging flash. A background fluorescence from the MOT remained in the vicinity of the dipole trap until $t = 20$ ms, corresponding to the third data point, at which point no background signal was left.

The experimental sequence for the measurement of the dipole trap lifetime is as follows: first the MOT is loaded from background rubidium vapour for 5 seconds using a cooling beam detuning of $-2\,\Gamma$, following which the first camera image is taken, measuring the fluorescence signal from the loaded MOT. The dipole trapping beam is then switched on at 80 mW power and the dipole trap is loaded and held in the MOT for 2 s, allowing time for the ICCD camera readout and re-arming of the trigger. The second image is then taken, measuring the fully loaded dipole trap in the MOT. Following another 2 s delay for the camera readout, the MOT cooling and repump beams and trapping field are switched off simultaneously at $t = 0$ ms, removing the MOT. The dipole beam is kept on while the cooling beam detuning is ramped linearly to $-0.2\,\Gamma$. The cooling beam is ramped close to resonance in this way so that the number of atoms can be

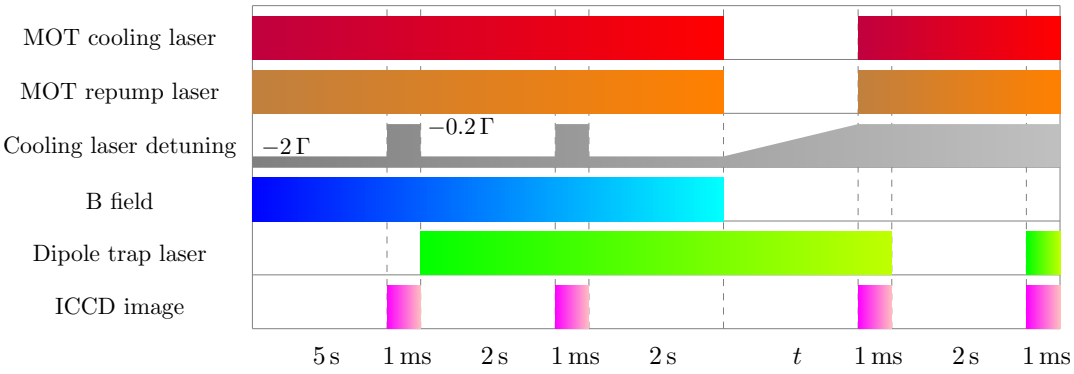

Figure 5.14: Diagram showing the experimental sequence for the measurement of the dipole trap lifetime. First the MOT is loaded for 5 s at a laser detuning of $\Delta = -2\,\Gamma$, cooling beam power of $\sim 30\,I/I_{\mathrm{sat}}$, total repump beam power of 3.5 mW and trapping field coil current of 3.6 A. The dipole trap laser is then switched on at 80 mW, the MOT is removed for a time t and the number of atoms remaining in the dipole trap after t is measured by ICCD camera imaging. The four images taken in the sequence in order are of the initial loaded MOT background, the fully loaded dipole trap in the MOT, the dipole trap remaining after t, and the background noise and stray light. The camera exposure time is 1 ms.

calculated using the correction factor for the light shift measured in section 5.2.2. After a time t the cooling and repump beams are switched back on at the same time as the camera is triggered to image the atoms remaining in the trap after t. The dipole trapping beam is then switched off to remove the atoms and a fourth image consisting of the background noise and scattered light is taken after another 2 s delay. The experimental sequence is displayed in Figure 5.14.

The results for the dipole trap lifetime measurement are displayed in Figure 5.15. There was too much fluctuation and noise in the MOT background to resolve and background-correct the dipole trap from the first two images of the sequence, so they could not be used for normalisation of the data by comparing each dipole trap image after t to the initial fully-loaded trap in the MOT. Therefore only the third and fourth images of the sequence were used, giving a background-corrected

average of 50 images of the dipole trap after time t. Similarly the first two data points, for $t = 1$ ms and 10 ms, contained background fluorescence from the MOT which was not easily removable as the MOT atoms had not yet had time to escape, so these two data points are ignored and only data from $t = 20$ to 5000 ms are plotted. The data was fit to using the model given by equation 5.13 and values of the fitting parameters were obtained from the fit, giving $A = 4.12 \pm 0.09$ s, single-body loss rate $\gamma = 0.28 \pm 0.04$ s^{-1} and two-body loss rate $\beta = 0.240 \pm 0.007$ s^{-1}. The initial number of atoms predicted by the model is $N_0 = 16$ and the lifetime of the trap incorporating both loss rates is $\tau = 1.94$ s. During the curve-fitting process the resulting values found for the fitting parameters were highly sensitive to the set starting values, diverging easily. To overcome this problem a large set of starting values for the initialisation of the parameters was looped over, obtaining those which returned the best fit to the data according to a χ^2 test. This process was repeated for another set of more closely spaced starting values in the vicinity of those obtained from the first loop, and the fitting parameters from this second cycle were chosen as the final results.

These results show good agreement between the experimental data and the theoretical model given by equation 5.13. In particular the contribution from two-body collisional losses is clear from the logarithmic-scale plot, in the form of the fast initial decay. The agreement is not so good at an atom number of ≈ 1 due to the fact that the model does not accurately describe the behaviour of the atoms in this regime. It can be seen that some of the data points within the region $t \sim 0.5 - 2$ s are outside error of the fitted curve and seem to follow a pattern alternating above and below this curve; this is due to the fact that the data points

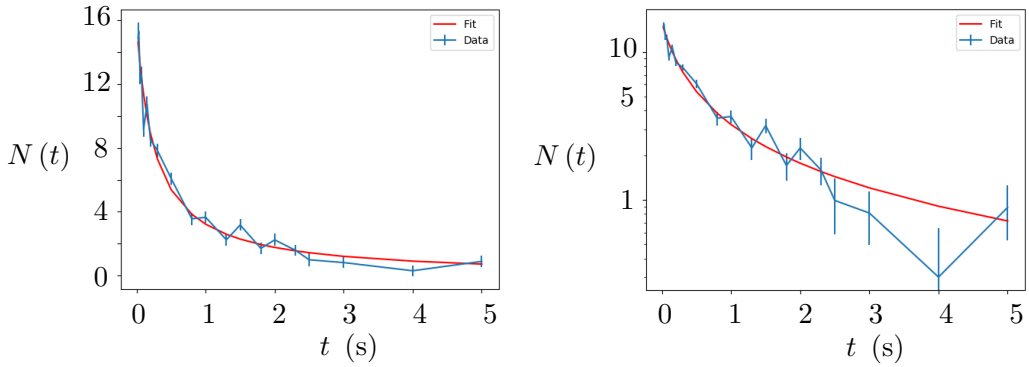

Figure 5.15: Dipole trap lifetime curve showing the number of atoms remaining in the trap $N(t)$ at time t after removing the MOT. The right-hand plot shows the same data plotted with a logarithmic-scale y axis. The experimentally measured data is shown by the blue data points and the red curve shows the fit to the data using the model given by equation 5.13 including single- and two-body collisional losses. The resultant single-body loss rate calculated from the fit is $\gamma = 0.28 \pm 0.04\ \mathrm{s}^{-1}$ and the two-body loss rate is $\beta = 0.240 \pm 0.007\ \mathrm{s}^{-1}$.

were acquired in a random order at different times throughout the day while continuously running current through the rubidium dispenser. Therefore the amount of background rubidium in the vacuum chamber was gradually increasing between data points, leading to increased loading of both the MOT and dipole trap, resulting in more atoms detected in the dipole trap at later times in the day. It was intended for this effect to be removed by normalising the data using a measurement of the initial number of atoms in the trap for each time t, but this was impossible due to the dipole trap being indistinguishable from the MOT background for these initial images. The data was taken out of order to remove systematic error in the decay rate due to this effect.

The single-body losses characterised by γ are driven by collisions between trapped atoms and fast-moving background vapour atoms or molecules, primarily between $Rb - H_2$ and $Rb - Rb$ [113]. This loss rate is independent of the number of

atoms in the dipole trap and is dependent on the background vapour pressure in the vacuum chamber. The scattering rates for these collisions have been calculated in [115], giving loss rates of $\gamma_{H_2}/n_{\mathrm{bg}} = 4.9 \times 10^{-9}\ \mathrm{cm^3\,s^{-1}}$ for $Rb - H_2$ and $\gamma_{Rb}/n_{\mathrm{bg}} = 6.3 \times 10^{-9}\ \mathrm{cm^3\,s^{-1}}$ for $Rb - Rb$ [113]. This is done by considering quantum-diffractive scattering[3] which is the main contribution to heating in shallow traps such as the dipole trap, and calculating the rate of collisions by including the background vapour density and the total scattering cross-section for van der Waals interactions, assuming an isotropic thermal Maxwellian distribution of atom velocities. Assuming the measured value of the one-body loss rate presented in this section is equal to the sum of these two rates, $\gamma = \gamma_{H_2} + \gamma_{Rb}$, and assuming the background vapour in the vacuum chamber obeys the ideal gas law[4], an estimate of the background vapour pressure p_{bg} can be evaluated, giving $p_{\mathrm{bg}}(\gamma) = 1.02 \times 10^{-9}$ mbar. This calculation also assumes the background vapour is at room temperature, $T_{\mathrm{bg}} = 300$ K. This background pressure measurement agrees with our expectation, being higher than the final pressure measured in the chamber after baking of $< 5 \times 10^{-10}$ mbar due to the addition of rubidium dispensed inside the chamber. A possible method for measuring the single-body losses independently of the two-body losses is to measure the loss rate in a dipole trap containing only a single atom, for which there are no two-body losses [112, 113], however this option is unavailable to us due to a lack of precise control over the number of atoms in our dipole trap.

[3] Quantum-diffractive scattering arises when the trap is shallow enough that only small scattering angles are required to eject atoms from the trap. Here, the small angle approximation used in the classical treatment of the scattering cross-section is not valid, so it is treated quantum mechanically [115].

[4] The ideal gas law is given by $pV = nRT$ where p is the pressure of the gas in Pa, V is the volume of the gas in $\mathrm{m^3}$, n is the number of atoms in mol, T is the temperature of the gas in K and R is the gas constant, given by $R = 8.314\ \mathrm{kg\,m^2\,s^{-2}\,K^{-1}\,mol^{-1}}$.

There are a number of different physical mechanisms which may contribute to the two-body loss rate β depending on the experimental conditions. In the absence of near-resonant light, the primary loss mechanism is hyperfine-changing collisions [111, 116–118]. Without near-resonant light driving transitions to an excited state, the trapped atoms populate the two ground-state hyperfine levels, $5^2S_{1/2}$ $F = 1$ and $F = 2$. A hyperfine-changing collision involves a pair of atoms, each in the $F = 1$ and $F = 2$ states respectively, causing a spin-flip and decay of the $F = 2$ atom down to the $F = 1$ state while the other atom remains in the $F = 1$ state. This results in the atom pair gaining energy equal to the ground-state hyperfine splitting of 6.83 GHz [43], being equivalent to hundreds of mK and therefore causing the atom pair to easily escape the typical dipole trap depths of ~ 1 mK. This is an inelastic collision in which there is an increase in the centre-of-mass kinetic energy of the atom pair [118].

If near-resonant light is present, transitions to the excited state $5^2P_{3/2}$ may occur, leading to further loss mechanisms known as light-assisted collisions [109–112, 119–121]. Neglecting the hyperfine structure, an atom pair initially in the state $5^2S_{1/2} - 5^2S_{1/2}$ may be excited to $5^2S_{1/2} - 5^2P_{3/2}$ if driven by near-resonant light. In this excited state the atom pair experiences a dipolar potential causing the atoms to accelerate towards each other until spontaneously decaying back to $5^2S_{1/2} - 5^2S_{1/2}$ by emitting a photon. The kinetic energy gain from the acceleration may cause the atom pair to escape the trap if it exceeds the trap depth. This condition is satisfied as long as the atoms manage to accelerate until they reach a critical radius of separation between each other. This process is known as radiative escape.

It is possible for the excited atom pair to transfer to the other fine level during the acceleration towards each other, ending up in the state $5^2S_{1/2} - 5^2P_{1/2}$, due to a crossing of the dipole potential curves for each of the states $5^2S_{1/2} - 5^2P_{3/2}$ and $5^2S_{1/2} - 5^2P_{1/2}$. Subsequent spontaneous decay back to the ground state can result in an increase in kinetic energy close to the fine-structure splitting energy separation, causing the atom pair to be ejected from the trap. This is known as a fine-changing collision. Other light-assisted two-body loss mechanisms include photoassociation, in which a ground-state atom pair may be excited to a bound molecular state and ejected from the trap upon de-excitation [122].

In this work, the dipole trap lifetime measurement was carried out without near-resonant light, so the expected mechanism for two-body loss occurring in this case is hyperfine-changing collisions. In comparison to the two-body loss parameter $\beta = (0.240 \pm 0.007)$ s^{-1} measured in this section, measurements by other groups of β due to hyperfine-changing collisions gave values of $(1.42 \pm 0.05) \times 10^{-6}$ s^{-1} [111] and 3×10^{-4} s^{-1} [109]. These values show a huge variation in loss rate as a result of significantly differing experimental parameters, primarily a much greater atom number density for the latter group.

Comparison with Previous Results

A measurement of the dipole trap lifetime was performed in [101] in the same laboratory and vacuum chamber using a previous incarnation of the dipole trap setup used in this work. In this case, the system was set up to produce a much larger trap with measured beam waists $w_H = (6.14 \pm 0.54)$ μm and $w_V = (7.01 \pm 0.54)$ μm in the horizontal and vertical directions respectively, with a

Rayleigh length along the imaging axis of $z_{\mathrm{R}} = (27.9 \pm 1.5)$ µm. This was done to allow tens of atoms to be trapped, producing an easily detectable amount of fluorescence. The resulting trapped atom cloud was detected successfully with estimated sizes $\sigma_{\mathrm{TH}} = (3.42 \pm 0.25)$ µm and $\sigma_{\mathrm{TV}} = (2.99 \pm 0.25)$ µm in the horizontal and vertical directions and $\sigma_{\mathrm{TL}} = (21.7 \pm 2.2)$ µm along the imaging axis. The trap depth was estimated as $U_0/k_{\mathrm{B}} = (662 \pm 109)$ µK and the corresponding light shift $\Delta_{\mathrm{LS}} = (13.8 \pm 2.3) \times 2\pi$ MHz. These values of the atom cloud size, trap depth and light shift were obtained by measurement of the trapping beam profile using a similar method to that described in section 5.2.1.

The results of the lifetime measurement with this larger trap are recreated from [101] in Figure 5.16 with permission from the author. Three different experimental sequences were tested; one similar to the method used in section 5.2.4, one with a 'cooling stage' inserted in the experimental sequence before $dt = 0$ ms in which the cooling beams are detuned and the trapping field is decreased to lower the temperature of the atoms, and one where the repump laser is left switched on throughout the measurement. The imaging flash time used was 5 ms, five times longer than for the measurement in this work. This causes a significant decrease in the atom number over the duration of the flash due to light-assisted collisions. The results show an initial rapid decay of the number of atoms in the trap between the first two data points for all three methods, falling to approximately 20% of the initial number. This feature is not described by a fit to the data using the model including one- and two-body losses given by equation 5.13, so the behaviour is not attributed to two-body collisional losses. As this data includes residual MOT background during the first 10 ms,

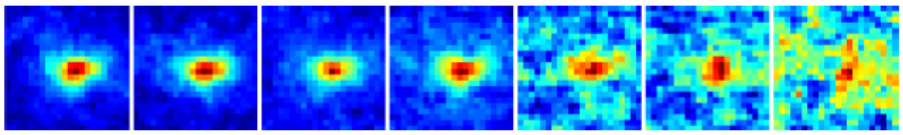

(a) Subsequent results for $dt = (5, 20, 50, 200, 1000, 2000 \text{ and } 3000)$ ms.

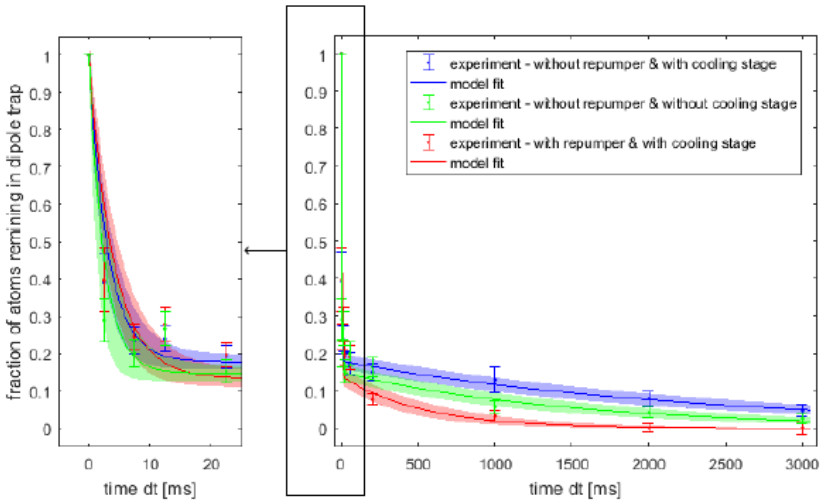

(b) Survival probability of atom in the trap in terms of holding time dt.

Figure 5.16: Dipole trap lifetime curve showing the number of atoms remaining in the trap $N(t)$ at time dt for a larger dipole trap of waist $w \approx 7$ µm. The atom number is normalised with respect to the initial number at $dt = 0$ ms. Three different cases are shown; first with a 'cooling stage' added in the sequence (blue), with no cooling stage (green) and with the cooling stage and leaving the repump beam on during the measurement (red). Taken from [101] with permission from the author.

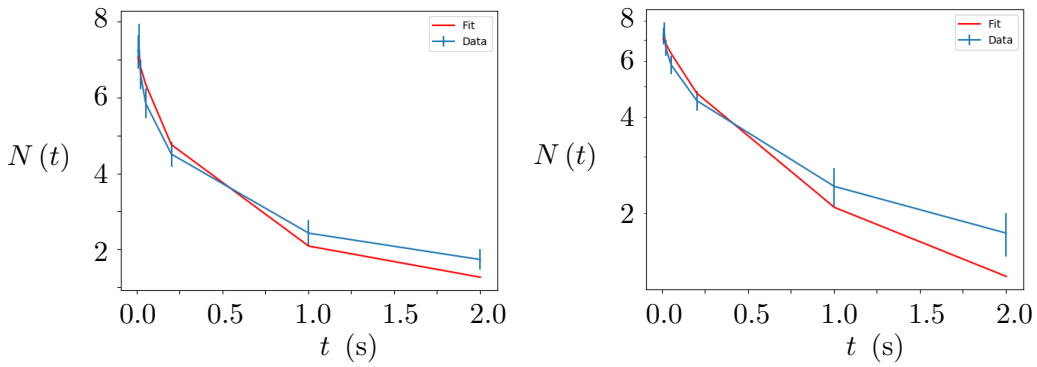

Figure 5.17: Dipole trap lifetime curve showing the number of atoms remaining in the trap $N(t)$ at time t for the larger trap used in [101]. The first and last data points have been removed as outliers. The right-hand plot shows the same data plotted with a logarithmic-scale y axis. The experimentally measured data is shown by the blue data points and the red curve shows the fitted model given by equation 5.13 using a fixed constant single-body loss rate $\gamma = 0.277 \pm 0.037\ \mathrm{s}^{-1}$. The two-body loss rate obtained from the fit is $\beta = 0.368 \pm 0.039\ \mathrm{s}^{-1}$.

the suggested mechanism for the fast decay is a locally increased background density at the dipole trap position due to the atoms in the MOT.

For comparison with the measurement in this work, the results from the measurement including the cooling stage and without repump beam are displayed in Figure 5.17 with the first and last data points omitted as outliers. The first data point is omitted due to the fast decay between the first two points described above, which is not produced by the model including one-body and two-body collisional losses. The last data point is omitted as it is an outlier which does not follow the model in equation 5.13. This may be because it is in the single-atom regime $N \lesssim 1$ where two-body losses cannot occur as at least 2 trapped atoms are required for a collision, whereas the model includes a contribution from two-body collisional losses for $0 < N < 1$. It proved more difficult to fit the model to this data due to fewer data points, with the fitting parameters diverging easily depending on

their set starting values. Therefore the single-body loss parameter γ was set to be constant and equal to that obtained in this work, $\gamma = 0.277\ \mathrm{s}^{-1}$. This is a reasonable assumption as this parameter depends only on the background vapour pressure, which should be similar between the two experiments, having been performed in the same vacuum chamber under similar conditions. The model shows a good fit to the data with a clear contribution from two-body collisional losses. The obtained values of the fitting parameters are $A = (2.82 \pm 0.27)$ s and $\beta = (0.368 \pm 0.039)\ \mathrm{s}^{-1}$. Interestingly, the two-body loss parameters β for the two dipole traps considered in this section are similar, whereas it is expected that the collisional loss rate for the trap in this work should be higher, in accordance with the higher atom number density as a result of the smaller trap volume. Using the estimation of the trap volume given in equation 5.9, the density of the trap in this work is $(4.2 \pm 0.4) \times 10^{11}\ \mathrm{cm}^{-3}$, a factor of 23.5 greater than the density of the larger trap, $(1.7 \pm 0.3) \times 10^{10}\ \mathrm{cm}^{-3}$. The two-body loss rate can be normalised with respect to the trap volume V in order to eliminate the density dependence, given by [112, 113]

$$\beta_{\mathrm{norm}} = 2\sqrt{2}V\beta. \tag{5.14}$$

The normalised two-body loss rates for the smaller and larger traps are $2.55 \times 10^{-11}\ \mathrm{cm}^3\,\mathrm{s}^{-1}$ and $3.68 \times 10^{-9}\ \mathrm{cm}^3\,\mathrm{s}^{-1}$, suggesting a two-body loss rate 150 times higher for the larger trap. There is no clear explanation for this discrepancy if following the assumption that the two-body collisional losses are hyperfine-changing collisions in the absence of near-resonant light, as these losses depend only on the physical characteristics of the trap and not the properties

	This work (small trap)	[101] (large trap)
Two-body loss rate β_{norm} ($\text{cm}^3\,\text{s}^{-1}$)	2.55×10^{-11}	3.68×10^{-9}
Volume V (μm^3)	38 ± 4	3490 ± 520
Number of atoms N	~ 16	~ 60
Density ρ (cm^{-3})	$(4.2 \pm 0.4) \times 10^{11}$	$(1.7 \pm 0.3) \times 10^{10}$
Trap depth U_0/k_{B} (mK)	2.46 ± 0.03	0.662 ± 0.109
Temperature T (μK)	494 ± 25	100 ± 20
Trap beam power P_{DT} (mW)	80	130
Light shift Δ_{LS} (2π MHz)	48 ± 5	13.8 ± 2.3
MOT beam detuning Δ_{M} (Γ)	-0.2	0
MOT beam intensity I_{M} ($\text{mW}\,\text{cm}^{-2}$)	$76.6 \approx 30s$	$76.6 \approx 30s$
Repump beam power P_{R} (mW)	3.5	2
Imaging flash time t_{f} (ms)	1	5

Table 5.1: Comparison of the physical properties of the dipole trap and experimental parameters used for the characterisation of the trap from this work (small trap) and from [101] (large trap).

of the near-resonant beams used for imaging. However this may be explained if there is a contribution from near-resonant light-assisted collisions, probably induced during the imaging flash of the MOT and repump lasers, as explained in the following.

The collisional dynamics of the atoms in the dipole trap in the presence of the MOT and repump beams is a complex process depending on a large number of often interdependent parameters, including the trap depth, trapping beam profile, temperature, and the intensity and detuning of the MOT and repump beams [109,111,112,116,118,120]. A comparison of the experimental parameters used for the two traps considered in this section is shown in Table 5.1. Despite the similar MOT beam detuning close to resonance for both traps, due to the higher intensity trapping beam for the small trap, there is a much greater induced light shift causing the effective detuning of the beams from the shifted resonance

frequency to be much larger than for the large trap. The light shift is equivalent to $8.6\,\Gamma$ for the small trap and $2.3\,\Gamma$ for the large trap. In [112] and [111], it was demonstrated experimentally that the two-body loss rate in the presence of near resonant light depends strongly on the detuning of the light from resonance. According to the measurement in [112], a difference in detuning equal to that of the traps considered in this section may increase the collisional loss rate of the larger trap by up to nearly two orders of magnitude. It is also shown in [111] that β depends on the trap depth, giving a higher loss rate for lower trap depths. This is consistent with the large trap having a trap depth approximately 4 times lower than the small trap. According to [118] the difference in atomic temperature should not make much difference to the collisional loss rate above $\sim$ 100 μK, perhaps even increasing the loss rate at lower temperatures, despite showing a discrepancy between their experimental data and theoretical models. Due to these dependences, the difference in effective MOT beam detuning, trap depth and atomic temperature between the two traps in this section may account for the factor of 150 increase in β_{norm} between the small and large traps, but only if the primary loss mechanism is driven by the MOT and repump beams which were used only during imaging. Therefore it is suggested that the trap lifetime has been measured in the presence of near-resonant light instead of the intended measurement in the absence of light.

For a future measurement of the trap lifetime excluding losses induced by near-resonant light, the method could be improved by decreasing the imaging flash time to reduce the effect of light-assisted collisions. However this would result in a decreased amount of fluorescence from the trap acquired by the

camera, reducing the signal-to-noise ratio. Similarly, tuning the beams used for imaging further from the effective light-shifted resonant frequency decreases the effect of two-body collisions, but also reduces the acquired signal, which is already very low for a dipole trap containing such a small number of atoms (~ 16). In [109], fluorescence imaging of the trap was also done using an ICCD camera, with an imaging time of 0.5 ms, but in this case up to 10^3 atoms were loaded in the dipole trap, which would greatly increase the detected amount of fluorescence. One possible solution to counteract the reduction in signal-to-noise caused by using a shorter imaging time would be to repeat the measurement for more repetitions of the experimental sequence, although this could easily lead to very long experiment times. Another option might be to change the imaging method of the trap, for example by using an avalanche photodiode (APD) to collect fluorescence, which is an extremely sensitive detection method capable of counting single photons. It has been demonstrated that single atoms in a dipole trap can be detected and spatially resolved by fluorescence imaging on an intensified CCD camera [96, 99, 123–125], so it may be possible to improve the current imaging system and fluorescence collection efficiency until it can be used for imaging the trap with much smaller imaging times. In [123], a single atom is imaged with an intensifier and CCD camera with an imaging time of just 2 µs, corresponding to the detection of a single photon. An image of the trap is then built up by repeating the experiment thousands of times and selecting only those images in which a photon was detected. A more accurate measurement of the trap lifetime utilising one of the suggested improved methods may give us a better understanding of the time-dependent evolution of the trap during future experiments and during the execution of potential applications in quantum

information protocols.

In conclusion, the comparison of the dipole trap lifetime results with those from a similar experiment using a previous larger version of the trap shows an unexpected difference in the normalised two-body loss parameter, which suggests that a significant factor in the two-body collisional losses is a result of light assisted collisions driven by the 780 nm light used for imaging the trap. Therefore the resulting measured lifetime is not an accurate measurement of the trap lifetime in the absence of near-resonant light as was intended. However, valuable information has been obtained regarding the method for the measurement of the trap lifetime; in particular, additional care must be taken to reduce the affect of the imaging beams on the collisional dynamics of the trapped atoms. The lifetime as a result of single- and two-body collisions with a contribution to light-assisted collisions in the presence of near-resonant light during the imaging flash was measured to be $\tau = 1.94$ s.

5.3 Summary

The dipole trap beam profile was carefully adjusted to produce a microscopic dipole trap small enough to operate within a single Rydberg blockade radius for potential applications in quantum information processing. As part of the redesign of the vacuum chamber, a stable mount for the beam-focussing lenses inside the chamber was produced, allowing a beam waist of $w_{\mathrm{H}} = (3.02 \pm 0.02)$ μm and $w_{\mathrm{V}} = (2.07 \pm 0.01)$ μm in the horizontal and vertical axes respectively. To achieve this, the input beam was adjusted to an appropriate size and collimation

using a prism pair and collimating lenses. An imaging system for measurements of the emitted fluorescence from the trap on an intensified CCD camera was implemented, with a magnification of the image from the trap position of $M = 14.32$. This was used to successfully image small numbers of $n < 50$ trapped atoms.

The physical properties and behaviour of the dipole trap have been characterised using various experimental methods, resulting in measurements of the size, 3D profile of the trapping beam, number of atoms and density of the trap, as well as the temperature of the atoms and light shift induced by the trapping beam. It was demonstrated by measuring the profile of the beam that a microscopic trap holding an atom cloud with diameter < 1.5 µm in the imaging plane orthogonal to the trapping beam propagation direction had successfully been implemented as intended, being significantly smaller than the calculated blockade radius of $R_\mathrm{b} \sim 4.4$ µm. However the trap size along the axis of beam propagation was found to be $\sigma_\mathrm{TL} = (7.0 \pm 0.3)$ µm, exceeding the blockade radius, so that the trap size in this dimension would have to be reduced in order to fully achieve the intended goal of containing the entire atom cloud within the blockade radius. This calculation of the beam size is taken as the most reliable result, as direct measurements with the CCD and ICCD cameras were limited by their resolution limit and had large uncertainties. A measurement of the atom number and light shift was done, resulting in a number of atoms typically varying between $\sim 29 - 42$ depending on the level of background rubidium vapour in the chamber. The induced light shift was measured for a series of different beam powers, giving $(48 \pm 5) \times 2\pi$ MHz at the full beam power of 80 mW in agreement with the theoretical prediction

from the beam profile measurement.

The temperature of the atoms in the dipole trap was measured using the time-of-flight (TOF) method, similarly to the measurement of the MOT temperature. This was done by capturing images of the atom cloud after switching off the trapping beam and allowing the atoms to expand thermally in space. The temperature is an important physical property of the atom cloud which affects the spatial distribution of the atoms in the trapping potential. The resulting measured temperature is $T = (494 \pm 25)$ μK with good agreement between the data and theoretical model. The initial size of the atom cloud during the TOF sequence at $dt = 0$ μs was found to be larger than expected, but without affecting the reliability of the previous measurement of the trap size which was reaffirmed by numerous other measurements.

An attempt was made to measure the lifetime of the dipole trap in order to characterise the behaviour of the number of atoms in the trap over time in the absence of the background reservoir provided by the MOT. This gives insight into the collisional dynamics in the trap and the behaviour of the atoms during the operation of potential applied quantum information processes. Weaknesses in the experimental method were revealed by the attempt at measuring the lifetime in the absence of near-resonant light, in which comparison with an older version of the trap suggested that in both cases there was too great a contribution from light-assisted collisional loss to give a reliable measurement of this lifetime. It is concluded that for a useful measurement, the procedure would have to be repeated with improvements to the method, such as reducing the imaging flash time. Overall, valuable insight into the behaviour of the trap has been gained

which will influence future work and experimental methods in the laboratory.

The overall conclusion to be drawn from the work presented in this chapter is that the goal of producing a microscopic dipole trap smaller than the Rydberg blockade radius has been partially achieved, as the atom cloud size exceeds the blockade radius in only one dimension, bringing us a step closer to the potential implementation of a blockade-induced quantum gate. In the following chapter, excitation to highly excited Rydberg states will be examined experimentally. These states may be used to induce the long-range interactions between ensembles of atoms required for quantum logic gates, and can allow the collective excitation of an atomic ensemble.

Chapter 6

Rydberg States for Long Range Interactions

In the previous chapter the experimental setup for a microscopic dipole trap containing small ensembles of atoms was presented, including the characterisation of the physical properties of the trap. In the context of the practical implementation of quantum information processing, which is the motivation for this work, the atoms collected in the dipole trap fulfil the requirements for a controllable qubit based on neutral atoms. Another vital requirement for quantum computation is the operation of quantum gates, which requires some form of interaction between neighbouring qubits. In section 2.4.6, a scheme enabling such interactions between dipole trapped qubits was described, based on exploiting the properties of highly excited Rydberg states and electromagnetically induced transparency. In this chapter, the first steps towards the experimental realisation of this scheme are described, including the development of the

two-photon transition laser system for the detection of Rydberg states.

As a first step towards the implementation of the two-photon transition to a Rydberg state in the dipole trap for potential applications in quantum information processing, with the intention of the eventual demonstration of a quantum logic operation, this two-photon excitation scheme was developed outside the vacuum chamber for convenience and so that the atom trapping experiments in the previous two chapters could be done in parallel. The experimental implementation of the two-photon excitation to probe Rydberg states is described in the following section, including the frequency stabilisation of the lasers and measurements of the detected Rydberg state frequencies.

6.1 Two-photon excitation laser system

As discussed in section 2.4.5, the EIT system requires both an infrared ($\sim$ 780 nm) laser and a blue ($\sim$ 480 nm) laser to establish the three-level atom scheme for EIT to occur. The red laser light is provided by an ECDL similar to those used for the cooling and repump transitions, and this laser is sent through a saturated absorption spectroscopy system for the initial tuning of the laser cavity to the vicinity of the probe beam transition. The blue laser used is a commercial model from Toptica, the TA/DL-SHG 110 laser which uses a 960 nm infrared diode laser passed through a frequency-doubling crystal to perform Second Harmonic Generation (SHG) in order to produce a 480 nm beam. The system also contains a tapered amplifier to give a high laser power of up to 300 mW. The experimental layout of the optics for the EIT lasers and their locking systems is shown in

Figure 6.1.

6.1.1 Frequency locking by modulation transfer spectroscopy

The main locking system used for the red laser is known as modulation transfer spectroscopy (MTS), and is a very robust locking technique [126]. This technique uses a counter-propagating pump and probe beam passed through a Rb vapour cell as in saturated absorption spectroscopy, although here the probe beam must have a higher power than the pump beam. Therefore it is convenient to use the same beams and Rb cell as in the saturated absorption set up, but with the pump and probe roles reversed to achieve the appropriate beam powers. The pump beam is phase modulated using an electro-optic modulator (EOM) to produce frequency sidebands at approximately 10 MHz either side of the carrier frequency[1].

Inside the Rb cell, the modulated pump beam interferes with the probe beam by four-wave mixing [127], adding sidebands to the probe beam. This occurs due to the non-linear interaction of the pump beam with the rubidium vapour medium near a resonance, causing the carrier and sidebands to undergo differing attenuation and dispersion, following which the modulation is transferred to the probe beam. The modulated probe beam is then sent into a fast photodiode, which can detect rf (radio frequency) heterodyne beat frequencies between the

[1]The EOM contains a lithium niobate crystal which has a refractive index that can be modified by an applied electric field. This allows frequency sidebands of adjustable separation from the carrier frequency to be produced.

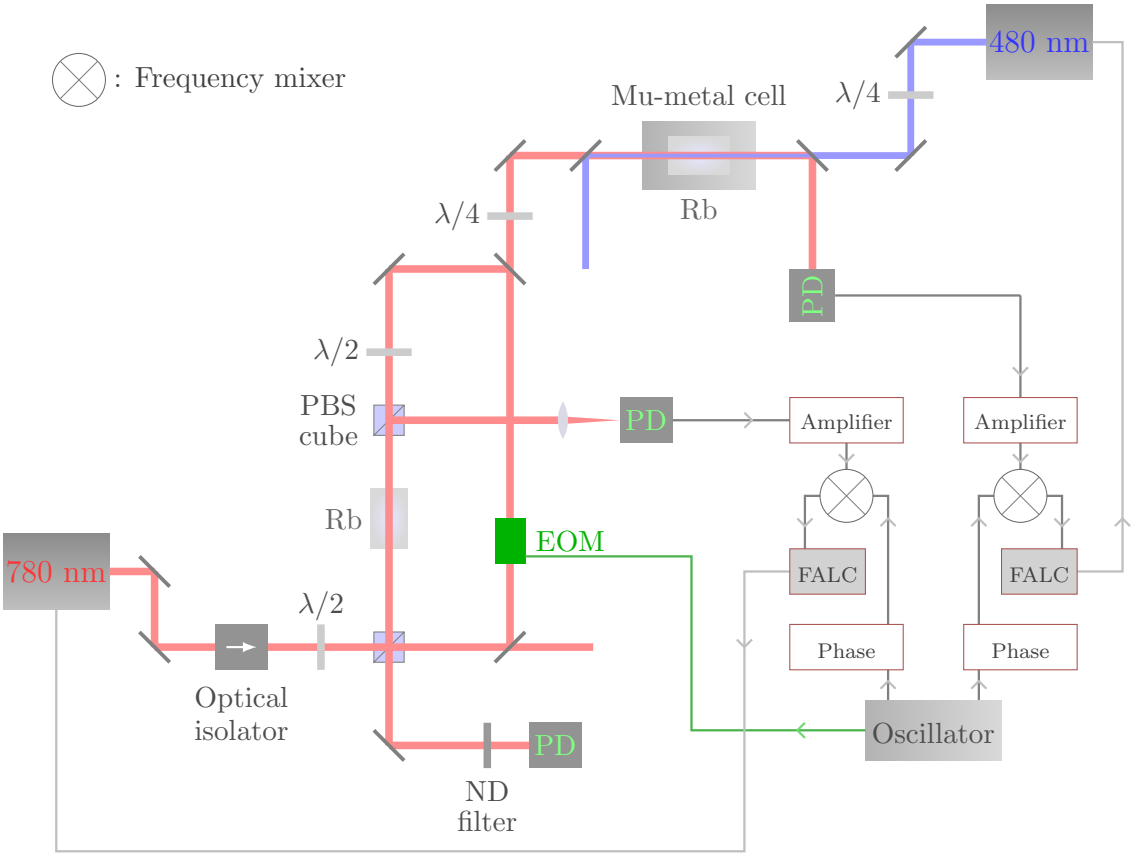

Figure 6.1: Schematic showing the experimental setup for two-photon excitation and frequency locking. The 780 nm red laser is phase modulated using the electro-optic modulator (EOM) to add frequency sidebands and subsequently frequency locked by modulation transfer spectroscopy (MTS), using a system of electronics with the final error signal produced by the fast analog linewidth controller (FALC). The saturated absorption spectrum is monitored by a photodiode (PD). The 480 nm blue laser is locked by MTS using the electromagnetically induced transparency (EIT) transmission peak obtained from two-photon excitation in the mu-metal cell.

sidebands and the carrier frequency. The absorptive and dispersive spectral features of the probe beam can be extracted from the amplitude and phase of the beat signal, when it is disturbed by resonance features such as sub-Doppler absorption peaks[2]. The signal from this photodiode is amplified and sent into a frequency mixer where it is combined with a phase-controlled reference signal from a function generator. The output is then sent into a commercial Toptica servo amplifier, the FALC 110 (Fast Analog Linewidth Controller), to obtain the final error signal. The FALC contains a low pass filter applied to the input signal, which together with the frequency mixer and phase shifter forms a phase sensitive detector at the modulation frequency of 10 MHz. The error signal output from the FALC module provides a dispersion lineshape which can be aligned to have a zero-crossing coinciding with the desired transition frequency.

Figure 6.2 (a) shows the raw error signal from the fast photodiode and the output of the frequency mixer, compared with the saturated absorption signal from a separate photodiode, all averaged four times. Figure 6.2 (b) displays the output error signal of the FALC, showing a well-defined zero-crossing for locking to the $5^2S_{1/2}$ $F = 3 \rightarrow 5^2P_{3/2}$ $F = 4$ transition of ^{85}Rb (the smallest leftmost peak of the saturated absorption spectrum), also averaged four times. The Fast Fourier Transform (FFT) of the raw signal from the fast photodiode is also shown, demonstrating a large peak at roughly 10 MHz, confirming the presence of the EOM-generated sidebands. This MTS locking scheme works as intended, providing stable locking to a transition for many hours at a time. This technique is more robust than the locking for the MOT lasers using the saturated absorption

[2]In contrast to saturated absorption spectroscopy, the signal from the crossover peaks is suppressed in MTS.

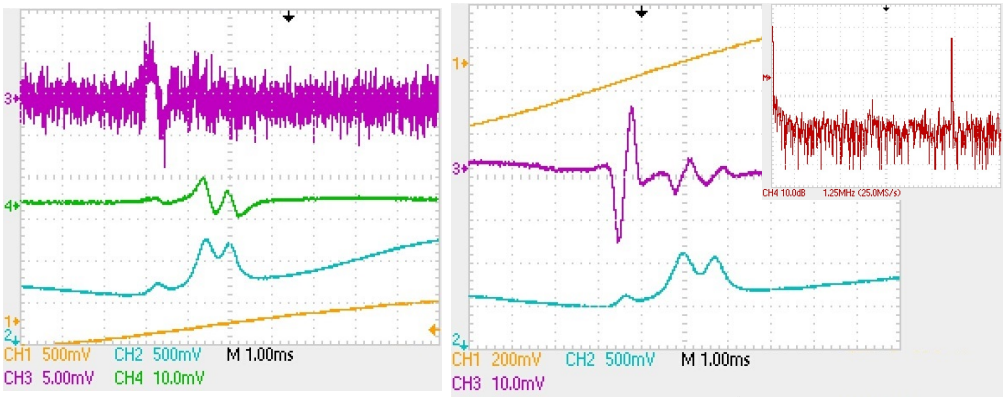

(a) (b)

Figure 6.2: Error signal obtained for the modulation transfer spectroscopy (MTS) locking scheme for the red laser to be used as the probe beam in the EIT system. In (a), the saturated absorption spectrum is shown by the blue scan, along with the raw signal from the fast photodiode detecting the modulated beam (green) and the frequency mixer output (purple). In (b), the final demodulated error signal from the output of the FALC 110 is shown (purple), with a well-defined zero crossing at the locking frequency. The inset shows the Fast Fourier Transform (FFT) of the modulated beam detected by the photodiode, showing a peak at about 10 MHz corresponding to the sideband frequency. All channels are averaged 4 times in both figures, except for the inset.

spectrum, being resistant to vibrational noise and impacts to the optics table.

The locking system used for the frequency stabilisation of the 480 nm blue laser is adapted from [128], and takes advantage of the EIT phenomenon to generate an error signal for locking from the EIT transmission feature itself. A 780 nm red laser beam is diverted by a beam splitter from the MTS locking system described earlier, and propagated through a magnetically shielded Rb vapour cell. This beam is frequency modulated by the EOM to obtain sidebands at about 10 MHz, and is frequency-locked to a given transition using the MTS scheme. The magnetic field shielding is provided by a high-permeability nickel-iron alloy known as mu-metal which encases the vapour cell. This is done to reduce stray

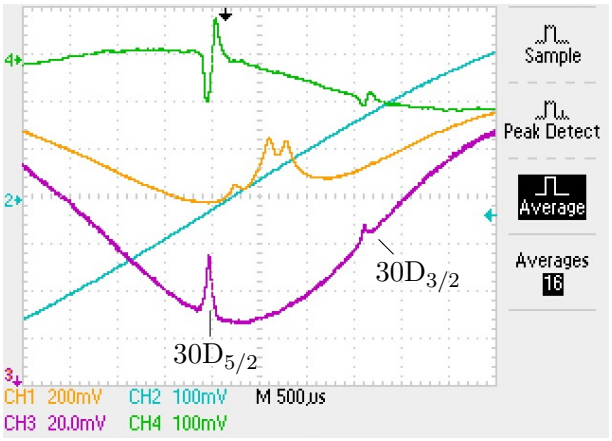

Figure 6.3: Absorption spectrum of the D_2 transition (yellow) from the ^{85}Rb $F = 3$ ground hyperfine level with the blue laser coupling the transition to the $30D_{5/2}$ and $30D_{3/2}$ Rydberg levels (purple). Narrow transmission peaks can be seen as a result of induced transparency. The corresponding error signal obtained from the transmission features and output from the FALC (Fast Analog Linewidth Controller) is shown (green). The blue trace shows the PZT scan over the frequency range. All spectra are averaged 16 times for clarity.

background magnetic fields from entering the cell, as the implemented scheme is sensitive to these fields. A counter-propagating high power ($\sim$ 200 mW) 480 nm beam from the blue laser is passed through the cell also, so that it overlaps with the red beam. The outgoing red beam is then diverted onto a fast photodiode using a dichroic mirror. The red light provides the probe beam and the blue light provides the coupling beam for EIT to occur. Now, the frequency of the blue laser can be scanned across an EIT resonance until the EIT transmission peak is observed from the fast photodiode. Due to the fact that the red and blue lasers are counter-propagating, the Doppler broadening of the peak is removed. An example of observed transmission peaks is displayed in Figure 6.3, showing transition resonances for the $30D_{5/2}$ and $30D_{3/2}$ states from the intermediate $5^2P_{3/2}$ state of ^{85}Rb.

The same modulation transfer technique used to lock the frequency of the red laser is used to obtain an error signal to lock the blue laser. The signal from the fast photodiode contains the heterodyne beat frequency between the probe sidebands and the carrier frequency. In this case, it is the EIT feature which distorts the beat signal to produce an error signal. The photodiode output is passed through an identical set of electronics as used for the red laser locking system, with the final dispersive error signal for locking the blue laser being output from another FALC 110 module. This experimental setup was used to achieve reliable and stable locking with both the red and blue lasers simultaneously. Locking was achieved for Rydberg states of both ^{85}Rb and ^{87}Rb, using the $5^2S_{1/2}$ $F = 3 \rightarrow 5^2P_{3/2}$ $F = 4$ red laser transition for ^{85}Rb and the $5^2S_{1/2}$ $F = 2 \rightarrow 5^2P_{3/2}$ $F = 3$ transition for ^{87}Rb, using the EIT transmission feature as an experimental signature of the coupling to the Rydberg state.

6.1.2 Measurement of wavelength

The wavelength of the blue laser was measured during locking to Rydberg states of ^{87}Rb using a Bristol 521 wavemeter, for comparison with the Rydberg level frequencies measured in [129] in order to identify the levels. Measurements were primarily focussed on ^{87}Rb for consistency with the atomic species used in the magneto-optical trap. The results are shown in Table 6.1 and displayed in Figure 6.4, showing good agreement between the measured wavelengths and those from [129], being mostly within the uncertainty limit of 0.005 nm introduced by the precision of the wavemeter. It is observed that the wavelengths measured in this work show a consistent tendency to be slightly larger than the compared

^{87}Rb Rydberg state	Blue wavelength from literature (nm)	Measured blue wavelength λ_b (nm) ($\pm$0.005)	Measured absolute frequency ω_0 ($\times 2\pi$ THz) ($\pm$0.01)
$27D_{5/2}$	482.917	482.917	1005.02
$29S_{1/2}$	482.852	482.860	1005.10
$28D_{5/2}$	482.630	482.630	1005.39
$30S_{1/2}$	482.573	482.577	1005.46
$29D_{5/2}$	482.375	482.379	1005.72
$31S_{1/2}$	482.324	482.329	1005.78
$30D_{5/2}$	482.147	482.150	1006.01
$32S_{1/2}$	482.100	482.104	1006.07

Table 6.1: Comparison of the measured blue laser wavelength for coupling to different Rydberg states with the values derived from literature [129–131] for ^{87}Rb. The measured absolute frequency ω_0 corresponds to the total transition from the ground state to the Rydberg state, assuming a red laser transition frequency $\omega_r = 384.22812 \times 2\pi$ THz [43] corresponding to $5^2S_{1/2}$ $F = 2 \rightarrow 5^2P_{3/2}$ $F = 3$.

values, which may be due to an offset in the measured wavelength from a potentially inaccurate calibration of the wavemeter. However the results are deemed consistent enough with the compared values to reliably identify the Rydberg levels observed. It is shown that frequency locking was achieved for states between $27D_{5/2}$ and $32S_{1/2}$.

The measured blue laser wavelengths correspond to a wavelength of the initial near-infrared extended cavity diode laser of $964 - 966$ nm before frequency doubling by second harmonic generation. It is possible to tune this wavelength coarsely as far as 960 nm by manual adjustment of the grating, with adjustments to the subsequent optics to retain the power and alignment of the output 480 nm beam. Using this wavelength it should be possible to lock to states with principal quantum numbers up to around $50 - 60$. Using equation 2.14, this would correspond to an increase in the Bohr atomic radius by a factor of ~ 4 from

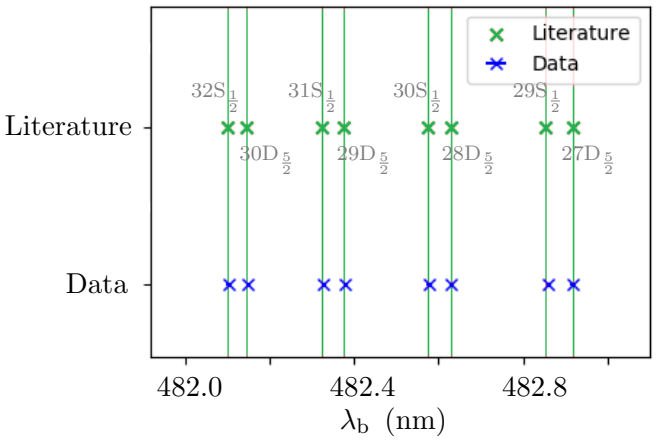

Figure 6.4: Comparison of measured Rydberg level frequencies with those from literature [129]. The wavelength measurements shown by the blue data points were obtained by measuring the output test beam of the initial $\sim$ 960 nm ECDL using a wavemeter. See Table 6.1 for the values of the plotted data points and the corresponding identified Rydberg levels. The error bars in the horizontal direction are too small to be seen.

approximately 1.3 nm to 5 nm, with an equally large increase in dipole moment, causing a significant extension in the blockade radius.

6.1.3 Investigation of the EIT feature and calculation of the Rydberg blockade radius

To investigate the EIT spectra obtained experimentally and measure the linewidth of the transmission feature, the background Doppler-broadened absorption feature was removed from the spectrum by fitting a Gaussian function as shown in Figure 6.5 (a). The lineshape of the transmission peak depends on several factors, including the detuning of the beams, the relative strengths of the probe and coupling beams and whether or not the vapour medium exhibits Doppler-broadened absorption [132]. For our experiments, the single-photon

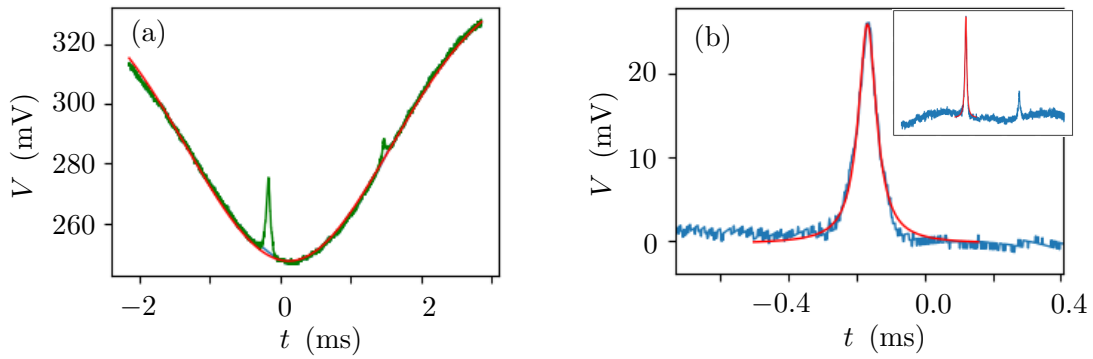

Figure 6.5: Analysis of the transparency peak from Autler-Townes splitting produced by a two-photon transition to the $30^2D_{5/2}$ Rydberg state. In (a) an inverted Gaussian function (red curve) is fitted to the background Doppler-broadened absorption feature for subtraction. In (b), the fitted Gaussian has been subtracted and a Lorentzian function (red curve) is fitted to the transparency feature, giving a linewidth of 22.3 $\times$ 2π MHz. The inset shows the full extent of the frequency scan.

resonance condition is fulfilled, meaning that both beams are on resonance with their respective transitions. In this case, the expected lineshape of the EIT peak is Lorentzian for non-Doppler broadened systems such as an ultra-cold sample of atoms in the MOT. However, for Doppler-broadened systems such as the room-temperature vapour cell used in this experiment, the peak is typically narrowed [133] and takes the form of a V- or U-shape in the strong probe and weak probe limits respectively [132]. Despite this, the peak observed in this experiment is still well approximated by a Lorentzian function, which may be due to the system being somewhere between the strong and weak probe limits. Therefore it is suitable to fit a Lorentzian function to the feature for the purpose of measuring the linewidth.

The resulting EIT transmission feature following the subtraction of the absorption is displayed in Figure 6.5 (b), with a Lorentzian fit to the larger $30^2D_{5/2}$ peak. The linewidth of the EIT feature is $\Delta_{\mathrm{EIT}} = 22.3 \times 2\pi$ MHz from the FWHM of

the fitted Lorentzian function. This is very large, far exceeding the contribution from the red and blue laser linewidths which are on the order of hundreds of kHz. Similarly, as the natural linewidth scales approximately as n^{-3} [134], the natural linewidth of the $30^2\mathrm{D}_{5/2}$ state is on the order of kHz and is far too small to account for this broadening. This suggests that there is significant power broadening of the transmission peak due to the high blue laser power. This high power was used because it was initially difficult to observe the transmission peak using a low power. A much deeper and clearer peak was observed upon increasing the blue laser power to the maximum available. Typical values of the linewidth used in calculations of the dipole blockade radius from [59, 63–65] are around $1 \times 2\pi$ MHz.

The EIT linewidth in a Doppler-broadened medium is described in [132], in which the linewidth in the weak-probe limit is given by

$$\Delta_{\mathrm{EIT}} \approx \frac{\Omega_{\mathrm{p}}^2 + \Omega_{\mathrm{c}}^2}{\widetilde{\Delta}}, \tag{6.1}$$

where Ω_{p} and Ω_{c} are the Rabi frequencies of the probe and coupling beams respectively, and $\widetilde{\Delta}$ is the effective inhomogeneous linewidth dependent on the velocity distribution of the atoms in the vapour medium. The probe beam intensity was estimated to be $\sim$ 4 mW, a factor of $\sim$ 2.4 greater than the saturation intensity of the ^{87}Rb D_2 transition, $I_{\mathrm{sat}} = 1.67\ \mathrm{mW\,cm^{-2}}$, leading to a Rabi frequency of $\Omega_{\mathrm{p}} = (6.6 = 0.8) \times 2\pi$ MHz. The Rabi frequency of the coupling beam can be calculated by $\Omega_{\mathrm{c}} = \frac{2\mu_n\sqrt{P}}{\hbar\sqrt{\pi w_0^2 c\epsilon_0}}$ where μ_n is the electric dipole moment for the transition from $5^2\mathrm{P}_{3/2}$ to the $n^2\mathrm{D}_{5/2}$ state, P is the power and w_0 is the waist of the beam [83, 135]. These dipole moments were

measured in [83]. Estimating the incident coupling beam power as 200 mW and beam waist as (0.15 ± 0.05) mm, the resulting coupling beam Rabi frequency is $\Omega_c = (37 \pm 13) \times 2\pi$ MHz. As $\Omega_c \gg \Omega_p$, it is appropriate to use the weak probe limit in the calculation of the EIT linewidth. Using equation 6.1, the theoretical EIT linewidth is given by $\Delta_{EIT} = (17 \pm 6) \times 2\pi$ MHz. This is in agreement with the experimentally measured width, and suggests that the large linewidth is a result of the high coupling beam Rabi frequency.

At high coupling beam powers, the transparency may be caused by an effect known as Autler-Townes splitting [136], which is similar but distinct to EIT. This is a type of a.c. Stark effect in which the oscillating electric field of the coupling radiation causes splitting of the eigenstates of the system into dressed states. This leads to the splitting of a single resonance with a corresponding absorption feature into a pair separated in frequency. The width of the transparency window is equal to the splitting between absorption peaks and increases with the effective Rabi frequency, $\sqrt{\Omega_p^2 + \Omega_c^2}$ [83]. The transition from EIT to the Autler-Townes regime occurs when the coupling beam Rabi frequency Ω_c exceeds the natural linewidth of the probe transition [137]. Due to the high power used for the blue laser, the radiation driving the coupling transition has a high Rabi frequency of $\Omega_c = (37 \pm 13) \times 2\pi$ MHz. This Rabi frequency exceeds the natural linewidth of the probe transition, $\Gamma = 6.0666 \times 2\pi$ MHz. Therefore it is suggested that the transparency feature observed in this section is a result of Autler-Townes splitting instead of EIT. However, this feature still indicates the presence of Rydberg levels and provides the means to probe these levels for the purposes of this work. It is expected that EIT can be achieved with this system by reducing the blue laser

power.

Despite the experimentally demonstrated transparency peak being a result of Autler-Townes splitting rather than EIT, a rough estimate of the Rydberg blockade radius induced by this system can be obtained by assuming that the peak is a power-broadened EIT feature. The equation for the blockade radius can be adapted from equation 2.15 as $R_\mathrm{b} = (C_6/\Delta_\mathrm{EIT})^{1/6}$. The C-dispersion coefficient for the 30S Rydberg state is calculated to be $C_6 = 30 \times 2\pi$ MHz μm^6 from [60], with similar values for the D states, which in conjunction with the power-broadened EIT linewidth results in a blockade radius of ~ 1 μm. This is slightly greater than the average radius 0.6 μm of the dipole-trapped cloud of atoms in the plane of the imaging axis found in section 5.2.1 but smaller than the trapping beam waist $\bar{w} = 2.5$ μm. Increasing the principal quantum number n to the region of $n \sim 60$ results in $C_6 = 160 \times 2\pi$ GHz μm^6, giving a blockade radius of ~ 4.4 μm with the same broadened linewidth. It is likely that decreasing the blue laser power will further increase the blockade radius due to a narrower linewidth, entering the EIT regime instead of Autler-Townes. Therefore it is expected that the developed setup should be capable of inducing a Rydberg blockade across the spatial extent of the microscopic dipole trap obtained in this work, in the plane of the imaging axis but not parallel to this axis, partially satisfying the requirement for an atomic qubit capable of collective excitation to a singular Rydberg state as required by the quantum gate operation proposed in section 2.4.6.

In order for the dipole interaction to be used to control the excitation of a second atomic qubit, the blockade radius must extend spatially from a Rydberg

excitation in one qubit over the second qubit. This would require a spatial separation between two distinct microscopic dipole traps on the order of a few μm to correspond to typical blockade radii in the $n \sim 60$ regime, which has been demonstrated elsewhere using incident trapping beams with slightly different entrance angles on a high-NA focussing lens [78].

6.2 Summary

In this chapter, the experimental realisation of the two-photon transition to Rydberg states has been demonstrated, with an effective frequency locking system based on modulation-transfer spectroscopy and exploiting the EIT feature. In section 6.1 the laser system for the implementation of this transition was described, including an explanation of the locking techniques used. Rydberg states were detected by the observation of a transparency feature, and the frequencies of these Rydberg levels were measured and found to agree with those measured and provided by another group. An estimate of the Rydberg blockade radius that could potentially be induced by the system was obtained in section 6.1.3, using the measured linewidth of $22.3 \times 2\pi$ MHz for the observed transparency feature. This was identified as Autler-Townes splitting rather than EIT due to the broad width of the feature, corresponding to a coupling Rabi frequency above threshold. This estimated blockade radius was found to be ~ 1 μm, increasing to ~ 4.4 μm assuming the possibility of reaching principal quantum numbers of $n \sim 60$.

The implementation of this excitation system in the laboratory is the first step

towards the demonstration of the Rydberg blockade effect in the microscopic dipole trap. This would lead to the creation of a dipole-trapped atomic qubit with the ability to act as a control qubit for nearby dipole traps, fulfilling part of the quantum logic gate described in section 2.4.6.

Chapter 7

Conclusions and Outlook

The body of work presented in this thesis details the development of experimental techniques for the cooling and trapping of neutral atoms in the laboratory. This work is motivated by the potential for the application of quantum computing using atoms as qubits. There has been significant interest in recent research towards the implementation of quantum computing, due to the potential for achieving enhanced computational efficiency for certain algorithms [1,2] compared to their best known classical analogues. The practical realisation of quantum computation would have commercial and technological applications in such fields as cybersecurity and communications. Numerous physical platforms have been proposed for the implementation of quantum bits of information, such as atoms, photons and superconducting circuits. Recent developments using neutral atoms have achieved increasingly large arrays of atomic qubits with high single-gate fidelities [14, 16, 17], and a gradual increase in two-qubit gate fidelities involving the entanglement of two atomic qubits [9, 10].

The goal undertaken for this research project was to develop and characterise a microscopic dipole trap containing small numbers of atoms as part of the larger objective of implementing a quantum logic gate based on Rydberg interactions. This logic gate is based on the proposal outlined in [67] and described in section 2.4.6. The production of this gate would facilitate the implementation of a quantum computational protocol such as DQC1, which would enable the calculation of the trace of an arbitrary unitary matrix with greater efficiency than the best possible classical algorithm [29, 55].

Early on during the project, problems with the vacuum chamber were identified which required the reconstruction of the chamber, as detailed in section 4.2. This meant that the project was initiated at a relatively undeveloped stage, spanning the design and construction of the vacuum chamber, adaptation of a previously existing laser system to obtain the magneto-optical trap (MOT) and characterise its properties (chapter 4), and the development of the laser system for the dipole trap and the characterisation of the dipole-trapped atom cloud (chapter 5). In addition, a separate laser system was developed to implement a two-photon transition for the probing of Rydberg states (chapter 6). In preparation for loading the dipole trap, a suitable MOT needed to be produced to act as a background reservoir of sufficiently cooled atoms. A system for imaging the MOT was established, along with the development of standard experimental procedures which allowed efficient collection and analysis of the data to retrieve the physical parameters of the atoms. It was found that the number of atoms loaded in the MOT was typically in the range of $N \sim 5 \times 10^5$, corresponding to atom number densities around $\rho \sim 5 \times 10^8$ cm^{-3}, with a lifetime of $\tau \sim 3$ s. Two methods for the

measurement of the MOT temperature were attempted, with the time-of-flight method accepted as the more reliable option, resulting in measured temperatures of $T = (500 \pm 63)$ μK for the MOT and $T = (79 \pm 9)$ μK for molasses. It was concluded that the characteristics of the MOT were suitable for loading a dipole trap.

The overarching aim of the project was to obtain a dipole trap which conformed to the size requirements for implementation as an atomic qubit for a Rydberg-based logic gate, as well as to develop experimental methods and programs for the characterisation of the properties of the trapped atoms. The size constraint imposed on the trap is that the trap must be able to be spatially contained within a Rydberg blockade radius. The blockade radius was determined in section 6.1 to be $R_{\mathrm{b}} \sim 4.4$ μm for principal quantum numbers in the range $n \sim 60$. Measurements of the size of the dipole-trapped atoms achieved in the laboratory in section 5.2.1 produced a result of $\bar{\sigma}_{\mathrm{T}} = (0.59 \pm 0.04)$ μm as the average atom cloud radius in the imaging plane, being well within the intended blockade radius. However, the atom cloud radius measured along the imaging axis in the direction of the propagation of the trapping beam was measured to be $\sigma_{\mathrm{TL}} = (7.0 \pm 0.3)$ μm, being in excess of the blockade radius, demonstrating that the goal had been partially achieved and that the size in this dimension would have to be reduced to fully achieve the goal of this work. Characterisation of the properties of the dipole trapped atom cloud is important as it informs future experimental procedures relating to the trap. The typical number of atoms in the dipole trap was measured to be in the range $N = 29 - 42$, with a light shift of $\Delta_{\mathrm{LS}} = (48 \pm 5) \times 2\pi$ MHz at the full trapping beam power of 80 mW, agreeing

with the theoretical prediction. The trap depth was predicted to be $U_0/k_B = (2.46 \pm 0.03)$ mK and the temperature of the trapped atoms was measured using the time-of-flight method as $T = (494 \pm 25)$ μK. An attempt was made to measure the lifetime of the dipole trap in the absence of near-resonant light, however analysis of the obtained experimental data and comparison with previous measurements revealed the presence of light-assisted collisions induced by the beams used to image the atom cloud by fluorescence. Valuable information was gained from this measurement which will allow improvements to the method in the future. The experimental methods and tools for the measurement of these properties and analysis of the collected data were developed during this time, allowing these measurements to be made much faster and more efficiently from now on.

The experimental realisation of a two-photon transition used to probe Rydberg states using the observation of the transparency feature from Autler-Townes splitting is detailed in chapter 6. It was shown that high-n states from $n = 27D_{5/2}$ to $32S_{1/2}$ were successfully detected, and that they could be accurately identified by comparison to literature. In the future, the laser system developed for this work may be used in conjunction with the trapped atoms in the vacuum chamber to investigate Rydberg-related phenomena, with the eventual goal of implementing a Rydberg-based logic gate between spatially separated dipole traps.

The work presented in this thesis has provided a major step towards the potential implementation of neutral atom-based DQC1 in our laboratory. In particular, significant groundwork has been laid with the establishment of the experimental

setup and the achievement of dipole-trapped atoms, along with the development of measurement techniques for the characterisation of the properties of the trapped atoms. As is the nature of experimental physics, no two experiments carried out in different laboratories can be exactly the same, due to differing environments. Therefore the contribution to knowledge provided by this thesis relates to the particular setup in our laboratory for which the acquisition and characterisation of a microscopic dipole trap smaller than the predicted Rydberg blockade radius has not been done before. The development of the experimental setup and the establishment of standard techniques for the measurement of the properties of the atoms in the MOT and dipole trap will greatly facilitate the work going forward in the laboratory towards the eventual implementation of quantum information processing, and will form a valuable basis for future experiments.

Future work

The groundwork established in this thesis can be built upon in future projects in order to approach the overarching goal of implementing the Rydberg-based quantum logic gate described in section 2.4.6, for the eventual demonstration of a quantum computational process such as DQC1. As the goal of obtaining a dipole trap entirely contained within the blockade radius was not fully completed due to the trapped atom cloud extending past this size in the imaging axis, reducing the size of the atom cloud could be the next step for the experimental setup. This could be done in a number of ways, such as reducing the temperature of the trapped atoms by loading from optical molasses instead of the MOT, causing the thermal density distribution of the atoms derived from the Boltzmann

distribution to occupy a smaller volume within the trap. The trap depth could also be reduced, for example by decreasing the intensity of the trapping beam. This would lead to increased evaporative cooling, so that the remaining cooler atoms similarly occupy a smaller volume. Alternatively the input trapping beam could be increased in diameter before hitting the focussing lens in order to produce a tighter trap at the focus point.

The dipole trap obtained in this work typically traps tens of atoms, so it may fulfil the role of the ensemble qubit for DQC1. As this protocol also requires a control qubit consisting of a single trapped atom, a dipole trap capable of single-atom trapping needs to be developed. The single-atom regime can be attained by reducing the trap size using the methods described above until in the collisional blockade regime [114]. Here, two-body collisional losses prevent more than one atom being loaded at any time.

At least one additional dipole trap will be required in close proximity to the existing trap, in order to provide the two spatially separated qubits for DQC1. Therefore an important part of future work will be the development of multiple microscopic traps. This can be done using multiple input trapping beams at slightly differing angles [78], or by the production of arbitrary trap geometries using a spatial light modulator (SLM) [45].

Another area of further development is the combination of the two-photon excitation system detailed in chapter 6 with the main dipole trapping system, to demonstrate EIT and Rydberg excitation within the dipole trapped ensemble qubit which is required for the proposed quantum logic gate. These are some of the main challenges which will need to be tackled in the future for the

implementation of DQC1 using neutral atoms.

Appendices

Appendix A

Sources of noise on the ICCD camera

As the ICCD camera is primarily designed for the acquisition of very small light signals, it is necessary to characterise the noise properties of the camera as it is important to maintain a good signal-to-noise ratio (SNR). Noise may be introduced either from external unwanted stray light being collected on the CCD during imaging, or from internal noise effects including readout noise, dark current and shot noise. The overhead room lights in the laboratory were found to have no detectable effect on the measured ICCD images. Stray light from the MOT lasers, however, have a small effect due to not being filtered out by the 780 nm filter in front of the detector. To remove the contribution from this stray laser light, images of the dipole trap were background-corrected.

Shot noise, also known as Poisson noise, results from the discrete nature of the photons acquired during imaging, which arrive at the detector randomly. The

fluctuation in photocurrent produced by this form of noise scales up with the square root of the average intensity of light acquired by the detector. This noise is reduced by either extending the imaging time or repeating the imaging many times and averaging the result. In the case of repeated measurements, the total signal acquired scales up linearly with the number of images and the shot noise scales with the square root of the number of images, leading to an increase in SNR proportional to the square root of the number of images.

Dark current is a form of noise which results from the thermal build up of electrons on the detector of a photoelectric device, instead of being produced by photon acquisition. This noise can build up steadily over time during a long readout of an image. Due to this being a thermal effect, it can be significantly reduced by cooling the detector. For measurements of the dipole trap described in this section, the ICCD camera is internally fan-cooled to $-20\,^{\circ}\mathrm{C}$, effectively removing the dark current noise. A characterisation of the dark noise on the ICCD is displayed in Figure A.1 (a), in which the full 1024×1024 detector area was recorded with no light falling on the detector at $20\,^{\circ}\mathrm{C}$ and at $-30\,^{\circ}\mathrm{C}$. The total time for the readout of the image was 23 s using a 50 kHz readout rate. The results show a gradual increase in pixel counts vertically for the $20\,^{\circ}\mathrm{C}$ case, as the pixels are read out from left to right then bottom to top. By the end of the readout 470 counts have been acquired from dark current. In contrast, the $-30\,^{\circ}\mathrm{C}$ measurement shows negligible increase in pixel counts during readout. The dark current is quoted in the manual as 0.2 $\mathrm{e^-\,pixel^{-1}\,s^{-1}}$ at $-30\,^{\circ}\mathrm{C}$.

The readout noise is introduced during the conversion of current from the photodetector into voltage by the on-chip amplifier during readout, before being

converted to a digital signal by the analogue-to-digital converter (ADC). Readout noise is typically referred to as a RMS number of electrons per pixel. The noise can be reduced by using a slower readout time, which is why the minimum readout rate of 50 kHz is used for all measurements of the dipole trap. The readout noise is quoted in the manual as 5 e^- for a 50 kHz readout rate. The readout noise can be characterised by measuring a mean-variance curve, in which the mean pixel count $\langle I \rangle$ of an image is compared to the standard deviation in pixel counts $\langle \sigma_I \rangle$, from which information about the noise properties of the camera can be derived. Background light was allowed to collect on a small 20 $\times$ 20 sub-image of the ICCD for varying exposure times, with a fan-cooled temperature of $-30\,^{\circ}$C and using a 50 kHz readout rate. A linear relationship is expected between $\log(\sigma_I)$ and $\log(\langle I \rangle)$. The results are shown in Figure A.1 (b) in analogue-to-digital units (ADU)[1], with longer exposure times corresponding to higher $\langle I \rangle$, showing several interesting features. Firstly, there is a positive constant offset in pixel counts of around 520 counts where the data begins. This offset is removed during imaging of the dipole trap in the background subtraction of the stray light. There is also a sharp non-linear decrease in variance at very low exposure times, shown in Figure A.1 (b) and (c) at low $\langle I \rangle$, which may be caused by quantisation noise. Finally the outliers at high exposure times are due to saturation of the pixels. The central linear portion of the data with the 520 pixel counts offset subtracted is fitted to using the model given by

$$\sigma_I = r + g\sqrt{\langle I \rangle} + fI, \tag{A.1}$$

[1]Analogue-to-digital units (ADU) refer to the digital value resulting from the ADC conversion from acquired voltage to a digital signal, equivalent to pixel counts in the image.

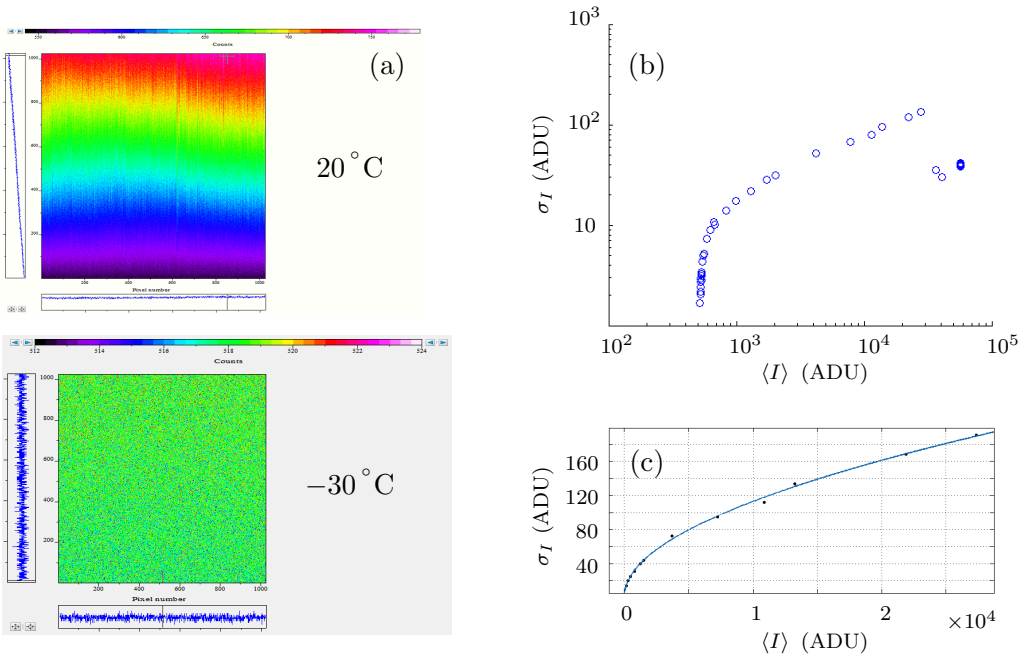

Figure A.1: Analysis of the dark and readout noise on the ICCD camera. In (a), The entire 1024×1024 detector area with no incident light was read out over 23 s at $20\,^{\circ}$C and $-30\,^{\circ}$C, showing an increase of $\sim$ 470 pixel counts vertically for $20\,^{\circ}$C as dark current is accumulated. In (b), the standard deviation in pixel counts σ_I is plotted against mean pixel counts $\langle I \rangle$ for images with varying exposure times. In (c), the central linear portion of this curve is fit to with equation A.1, giving readout noise $r = 1.276$, conversion gain $g = 1.083$ and fixed pattern noise $f = 3.38 \times 10^{-4}$ in ADU.

where r is the readout noise in ADU, g is the conversion gain from the number of electrons to ADU, and f is the fixed pattern noise in ADU which arises from random spatially-dependent variations in pixel counts across the CCD. The resulting fit is displayed in Figure A.1 (c), showing good fit to the model. The fitting parameters acquired from the fit are $r = 1.276$, $g = 1.083$ and $f = 0.000338$. The conversion gain is close to the expected value of 1, however the readout noise r appears to be small compared to the fluctuation in pixel counts observed in real time. This may be caused by residual effects of quantisation noise or an inaccurate assumption of the offset in pixel counts. The value obtained experimentally is smaller than the value quoted in the manual, which is $r = 5\,\mathrm{e}^-$ for a 50 kHZ readout rate. The readout noise is determined not to have a large negative impact on the signal-to-noise in images of a few or more atoms in the dipole trap.

In this section, an analysis of the noise on the ICCD camera was performed in order to identify the necessary measures that need to be taken to ensure a suitable SNR is obtained during measurements of the dipole trap characteristics. It is concluded that the camera should be operated at a low temperature to remove dark current noise; the final temperature used during dipole trap measurements was $-20\,^{\circ}\mathrm{C}$ as cooling to this temperature is much quicker than to the $-30\,^{\circ}\mathrm{C}$ used during testing. It is also concluded that images obtained during measurements should be background-corrected to remove the ~ 520 pixel count offset, and that the readout noise is not large enough to negatively affect measurements.

Bibliography

[1] Shor, P. W. *J.Sci.Statist.Comput.* **26**, 1484 (1997).

[2] Grover, L. K. *Phys.Rev.Lett.* **79**, 325–328 (1997).

[3] Datta, A., Shaji, A., and Caves, C. M. *Phys.Rev.Lett.* **100**, 050502 (2008).

[4] DiVincenzo, D. P. *Fortschr. Phys.* **48**, 771–783 (2000).

[5] Hagley, E., Maître, X., Nogues, G., Wunderlich, C., Brune, M., Raimond, J. M., and Haroche, S. *Phys.Rev.Lett.* **79**, 1 (1997).

[6] Wilk, T., Gaëtan, A., Evellin, C., Wolters, J., Miroshnychenko, Y., Grangier, P., and Browaeys, A. *Phys.Rev.Lett.* **104**, 010502 (2010).

[7] Isenhower, L., Urban, E., Zhang, X. L., Gill, A. T., Henage, T., Johnson, T. A., Walker, T. G., and Saffman, M. *Phys.Rev.Lett.* **104**, 010503 (2010).

[8] Nielsen, M. A. and Chuang, I. L. *Quantum Computation and Quantum Information.* Cambridge University Press, (2000).

[9] Jau, Y.-Y., Hankin, A. M., Keating, T., Deutsch, I. H., and Biedermann, G. W. *Nature* **12**, 71–74 (2016).

[10] Maller, K. M., Lichtman, M. T., Xia, T., Sun, Y., Piotrowicz, M. J., Carr, A. W., Isenhower, L., and Saffman, M. *Phys. Rev. A* **92**, 022336 (2015).

[11] Ebert, M., Kwon, M., Walker, T. G., and Saffman, M. *Phys. Rev. Lett.* **115**, 093601 (2015).

[12] Zeiher, J., Schauß, P., Hild, S., Bloch, T. M. I., and Gross, C. *Phys. Rev. X* **5**, 031015 (2015).

[13] Nogrette, F., Labuhn, H., Ravets, S., Barredo, D., Béguin, L., Vernier, A., Lahaye, T., and Browaeys, A. *Phys.Rev.X* **4**, 021034 (2014).

[14] Xia, T., Lichtman, M., Maller, K., Carr, A. W., Piotrowicz, M. J., Isenhower, L., and Saffman, M. *Phys. Rev. Lett.* **114**, 100503 (2015).

[15] Wang, Y., Kumar, A., Wu, T.-Y., and Weiss, D. S. *Science* **352**, 1562–1565 (2016).

[16] Endres, M., Bernien, H., Keesling, A., Levine, H., Anschuetz, E. R., Krajenbrink, A., Senko, C., Vuletic, V., Greiner, M., and Lukin, M. D. *arXiv:1607.03044* .

[17] Barredo, D., de Léséleuc, S., Lienhard, V., Lahaye, T., and Browaeys, A. *Science* **354**, 1021–1023 (2016).

[18] Treutlein, P., Hommelhoff, P., Steinmetz, T., Hänsch, T. W., and Reichel, J. *Phys. Rev. Lett.* **92**, 203005 (2004).

[19] Zeuner, J., Sharma, A. N., Tillmann, M., Heilmann, R., Gräfe, M., Moqanaki, A., Szameit, A., and Walther, P. *npj Quantum Information* **4**, 13 (2018).

[20] Lekitsch, B., Weidt, S., Fowler, A. G., Mølmer, K., Devitt, S. J., Wunderlich, C., and Hensinger, W. K. *Science Advances* **3**, 2 (2017).

[21] Hsu, J. https://spectrum.ieee.org/tech-talk/computing/hardware/intels-49qubit-chip-aims-for-quantum-supremacy. Accessed: 2018-04-24.

[22] Greene, T. https://thenextweb.com/artificial-intelligence/2018/03/06/google-reclaims-quantum-computer-crown-with-72-qubit-processor/#. Accessed: 2018-04-24.

[23] Galeon, D. https://futurism.com/ibm-announced-50-qubit-quantum-computer/. Accessed: 2018-04-24.

[24] Knill, E. and Laflamme, R. *Phys.Rev.Lett.* **81**, 5672–5675 (1998).

[25] Datta, A. and Shaji, A. *International Journal of Quantum Information* **9**, 1787–1805 (2011).

[26] Lanyon, B. P., Barbieri, M., Almeida, M. P., and White, A. G. *Phys.Rev.Lett.* **101**, 200501 (2008).

[27] Passante, G., Moussa, O., and Laflamme, R. *Phys.Rev.A* **85**, 032325 (2012).

[28] Passante, G., Moussa, O., Ryan, C. A., and Laflamme, R. *Phys.Rev.Lett.* **103**, 250501 (2009).

[29] Mansell, C. W. and Bergamini, S. *New Journal of Physics* **16**, 053045 (2014).

[30] Modi, K., Cable, H., Williamson, M., and Vedral, V. *Phys.Rev.X* **1**, 021022 (2011).

[31] Shor, P. W. and Jordan, S. P. *Quantum Information and Computation* **8**, 681 (2008).

[32] Ollivier, H. and Zurek, W. H. *Phys.Rev.Lett.* **88**, 017901 (2001).

[33] Lanyon, B. P., Weinhold, T. J., Langford, N. K., O'Brien, J. L., Resch, K. J., Gilchrist, A., and White, A. G. *Phys. Rev. Lett.* **100**, 060504 (2008).

[34] Buluta, I., Ashhab, S., and Nori, F. *Reports on Progress in Physics* **74**, 10 (2011).

[35] Langer, C., Ozeri, R., Jost, J. D., Chiaverini, J., DeMarco, B., Ben-Kish, A., Blakestad, R. B., Britton, J., Hume, D. B., Itano, W. M., Leibfried, D., Reichle, R., Rosenband, T., Schaetz, T., Schmidt, P. O., and Wineland, D. J. *Phys. Rev. Lett.* **95**, 060502 (2005).

[36] Cirac, J. I. and Zoller, P. *Phys. Rev. Lett.* **74**, 4091 (1995).

[37] Ladd, T. D., Jelezko, F., Laflamme, R., Nakamura, Y., Monroe, C., and O'Brien, J. L. *Nature* **464**, 45–53 (2010).

[38] Barends, R., Kelly, J., Megrant, A., Veitia, A., Sank, D., Jeffrey, E., White, T. C., Mutus, J., Fowler, A. G., Campbell, B., Chen, Y., Chiaro, B., Dunsworth, A., Neill, C., O'Malley, P., Roushan, P., Vainsencher, A., Wenner, J., Korotkov, A. N., Cleland, A. N., and Martinis, J. M. *Nature* **508**, 500–503 (2014).

[39] Vandersypen, L. M. K. and Chuang, I. L. *Rev. Mod. Phys.* **76**, 1037 (2005).

[40] Knill, E., Laflamme, R., and Milburn, G. J. *Nature* **409**, 46–52 (2001).

[41] Saffman, M. and Walker, T. G. *Reviews of Modern Physics* **82**, 2313–2363 (2010).

[42] Steck, D. A. Rubidium 85 D Line Data (Available online: http://steck.us/alkalidata/), (2010).

[43] Steck, D. A. Rubidium 87 D Line Data (Available online: http://steck.us/alkalidata/), (2010).

[44] Catanzaro, E. J., Murphy, T. J., Garner, E. L., and Shields, W. R. *Journal of Research of the National Bureau of Standards - A. Physics and Chemistry* **73A**, 511–516 (1969).

[45] Bergamini, S., Darquié, B., Jones, M., Jacubowiez, L., Browaeys, A., and Grangier, P. *J.Opt.Soc.Am.B* **21**, 1889–1894 (2004).

[46] Jessen, P. S. and Deutsch, I. H. *Adv. in At. Mol. and Opt. Phys* **37**, 95 (1996).

[47] Grynberg, G., Lounis, B., Verkerk, P., Courtois, J.-Y., and Salomon, C. *Phys. Rev. Lett.* **70**, 2249 (1993).

[48] van Oosten, D., van der Straten, P., and Stoof, H. T. C. *Phys. Rev. A.* **63**, 053601 (2001).

[49] Foot, C. J. *Atomic Physics.* Oxford University Press, (2005).

[50] Kowalczyk, A. U. *Manipulaton and Control of Ultra-Cold Rubidium Atoms.* PhD thesis, The Open University, (2012).

[51] Beterov, I. I., Ryabtsev, I. I., Tretyakov, D. B., and Entin, V. M. *Phys. Rev. A* **79**, 052504 (2009).

[52] Béguin, L., Vernier, A., Chicireanu, R., Lahaye, T., and Browaeys, A. *Phys.Rev.Lett.* **110**, 263201 (2013).

[53] Ravets, S., Labuhn, H., Barredo, D., Béguin, L., Lahaye, T., and Browaeys, A. *Nature Physics* **10** (2014).

[54] Ravets, S., Labuhn, H., Barredo, D., Lahaye, T., and Browaeys, A. *Available online (arXiv:1504.00301)* (2015).

[55] Mansell, C. W. *Cold Atoms for Deterministic Quantum Computation with One Qubit.* PhD thesis, The Open University, (2014).

[56] Lukin, M. D., Fleischhauer, M., Cote, R., Duan, L. M., Jaksch, D., Cirac, J. I., and Zoller, P. *Phys.Rev.Lett.* **87**, 037901 (2001).

[57] Comparat, D. and Pillet, P. *J.Opt.Soc.Am.B* **27**, A208–A232 (2010).

[58] Beterov, I. I., Saffman, M., Zhukov, V. P., Tretyakov, D. B., Entin, V. M., Yakshina, E. A., Ryabtsev, I. I., Mansell, C. W., MacCormick, C., Bergamini, S., and Fedoruk, M. P. *Laser Physics* **24**, 074013 (2014).

[59] Pritchard, J. D. *Cooperative Optical Non-linearity in a blockaded Rydberg Ensemble*. PhD thesis, Durham University, (2011).

[60] Singer, K., Stanojevic, J., Weidemüller, M., and Côté, R. *J. Phys. B: At. Mol. Opt. Phys.* **38**, S295 (2005).

[61] Marinescu, M. *Phys. Rev. A* **56**, 4764 (1997).

[62] Pritchard, J. D., Weatherill, K. J., and Adams, C. S. *Annual Review of Cold Atoms and Molecules* **1**, 301–350 (2013).

[63] Maxwell, D., Szwer, D. J., Barato, D. P., Busche, H., Pritchard, J. D., Gauguet, A., Weatherill, K. J., Jones, M. P. A., and Adams, C. S. *Phys. Rev. Lett.* **110**, 103001 (2013).

[64] Paredes-Barato, D. and Adams, C. S. *Phys. Rev. Lett.* **112**, 040501 (2014).

[65] Pritchard, J. D., Gauguet, A., Weatherill, K. J., Jones, M. P. A., and Adams, C. S. *Phys. Rev. Lett.* **105**, 193603 (2010).

[66] Müller, M. M., Murphy, M., Montangero, S., Calarco, T., Grangier, P., and Browaeys, A. *Phys.Rev.A* **89**, 032334 (2014).

[67] Müller, M. M., Lesanovsky, I., Weimer, H., Büchler, H. P., and Zoller, P. *Phys.Rev.Lett.* **102**, 170502 (2009).

[68] Fleischhauer, M., Imamoglu, A., and Marangos, J. P. *Reviews of Modern Physics* **77**, 633–673 (2005).

[69] Steck, D. A. *Available online* (2010).

[70] Haas, M., Leung, V., Frese, D., Haubrich, D., John, S., Weber, C., Rauschenbeutel, A., and Meschede, D. *New Journal of Physics* **9**, 147 (2007).

[71] Camparo, J. C. and Frueholz, R. P. *Phys. Rev. A* **30**, 803 (1984).

[72] Camparo, J. C. and Frueholz, R. P. *Phys. Rev. A* **31**, 1440 (1985).

[73] Caillet, X. and Simon, C. *Eur.Phys.J.D* **42**, 341 (2005).

[74] Beterov, I. I., Saffman, M., Yakshina, E. A., Zhukov, V. P., Tretyakov, D. B., Entin, V. M., Ryabtsev, I. I., Mansell, C. W., MacCormick, C., Bergamini, S., and Fedoruk, M. P. *Phys. Rev. A* **88**, 010303 (2013).

[75] Vitanov, N. V., Halfmann, T., Shore, B. W., and Bergmann, K. *Annu.Rev.Phys.Chem.* **52**, 763–809 (2001).

[76] Kis, Z., Karpati, A., Shore, B. W., and Vitanov, N. V. *Phys.Rev.A* **70**, 053405 (2004).

[77] Kis, Z. and Renzoni, F. *Phys.Rev.A* **65**, 032318 (2002).

[78] Béguin, L. *Measurement of the van der Waals interaction between two Rydberg atoms.* PhD thesis, Institut d'Optique Graduate School, (2013).

[79] Barreiro, J. T., Schindler, P., Gühne, O., Monz, T., Chwalla, M., Roos, C. F., Hennrich, M., and Blatt, R. *Nature Physics* **6**, 943 (2010).

[80] Saffman, M. and Walker, T. G. *Phys.Rev.A* **72**, 022347 (2005).

[81] Dalibard, J. and Cohen-Tannoudji, C. *J.Opt.Soc.Am.B* **6**, 2023–2045 (1989).

[82] Ungar, P. J., Weiss, D. S., Riis, E., and Chu, S. *J.Opt.Soc.Am.B* **6**, 2058 (1989).

[83] Piotrowicz, M. J. *Ultracold Rydberg atoms.* PhD thesis, The Open University, (2010).

[84] Grimm, R., Weidemüller, M., and Ovchinnikov, Y. B. *Advances in Atomic, Molecular and Optical Physics* **42**, 95–170 (2000).

[85] Thorlabs Inc. Sanyo DL7140-201S Laser Diode Specifications, http://www.thorlabs.de/thorProduct.cfm?partNumber=DL7140-201S.

[86] Hooker, S. M. and Webb, C. E. *Laser Physics.* Oxford University Press, (2010).

[87] Torralbo-Campo, L., Bruce, G. D., Smirne, G., and Cassettari, D. *Sci.Rep.* **5**, 14729 (2015).

[88] Moore, R. W. G., Lee, L. A., Findlay, E. A., Torralbo-Campo, L., and Cassettari, D. *Available online (arXiv:1401.7949)* (2014).

[89] Arpornthip, T., Sackett, C. A., and Hughes, K. J. *Phys.Rev.A* **85**, 033420 (2012).

[90] Steane, A. M., Chowdhury, M., and Foot, C. J. *J.Opt.Soc.Am.B* **9**, 2142–2158 (1992).

[91] Bjorkholm, J. E. *Phys.Rev.A* **38**, 1599 (1988).

[92] Harris, N. S. *Modern Vacuum Practice*. London : McGraw-Hill, (1989).

[93] Arnold, A. S., Wilson, J. S., and Boshier, M. G. *Rev.Sci.Inst.* **69**, 1236 (1998).

[94] Russell, L., Kumar, R., Tiwari, V. B., and Chormaic, S. N. *Opt.Commun.* **309**, 313 (2013).

[95] Lett, P. D., Watts, R. N., Westbrook, C. I., Phillips, W. D., Gould, P. L., and Metcalf, H. J. *Phys. Rev. Lett.* **61**, 169 (1988).

[96] Schlosser, N., Reymond, G., Protsenko, I., and Grangier, P. *Nature* **411**, 1024–1027 (2001).

[97] Frese, D., Ueberholz, B., Kuhr, S., Alt, W., Schrader, D., Gomer, V., and Meschede, D. *Phys.Rev.Lett.* **85**, 3777 (2000).

[98] Weber, M., Volz, J., Saucke, K., Kurtsiefer, C., and Weinfurter, H. *Phys.Rev.A* **73**, 043406 (2006).

[99] Kuhr, S., Alt, W., Schrader, D., Müller, M., Gomer, V., and Meschede, D. *Science* **293**, 278 (2001).

[100] Alt, W., Schrader, D., Kuhr, S., Müller, M., Gomer, V., and Meschede, D. *Phys.Rev.A* **67**, 033403 (2003).

[101] Krzyzanowska, K. *Development of a Cold Atoms Platform for DQC1 Implementation*. PhD thesis, Open University, (2017).

[102] Møller, D., Madsen, L. B., and Møller, K. *Phys.Rev.Lett.* **100**, 170504 (2008).

[103] Petrosyan, D. and Møller, K. *Phys.Rev.A* **87**, 033416 (2013).

[104] Schlosser, N., Reymond, G., Protsenko, I., and Grangier, P. *Nature* **411**, 1024–1027 (2001).

[105] Yavuz, D. D., Kulatunga, P. B., Urban, E., Johnson, T. A., Proite, N., Henage, T., Walker, T. G., and Saffman, M. *Phys. Rev. Lett.* **96**, 063001 (2006).

[106] Reymond, G., Schlosser, N., Protsenko, I., and Grangier, P. *Phil. Trans. R. Soc. L* **361**, 1527–1536 (2003).

[107] Bourgain, R., Pellegrino, J., Fuhrmanek, A., Sortais, Y. R. P., and Browaeys, A. *Phys. Rev. A* **88**, 023428 (2013).

[108] Protsenko, I. E., Reymond, G., Schlosser, N., and Grangier, P. *Phys. Rev. A* **65**, 052301 (2002).

[109] Kulatunga, P., Blum, T., and Olek, D. (2010).

[110] Telles, G. D., Marcassa, L. G., Muniz, S. R., Miranda, S. G., Antunes, A., Westbrook, C., and Bagnato, V. S. *Phys.Rev.A* **59**, R23–R26 (1999).

[111] Kuppens, S. J. M., Corwin, K. L., Miller, K. W., Chupp, T. E., and Wieman, C. E. *Phys.Rev.A* **62**, 013406 (2000).

[112] Fuhrmanek, A., Bourgain, R., Sortais, Y. R. P., and Browaeys, A. *Phys.Rev.A* **85**, 062708 (2012).

[113] Fuhrmanek, A. *From single to many atoms in a microscopic optical dipole trap.* PhD thesis, University of Paris-Sud, (2011).

[114] Schlosser, N., Reymond, G., and Grangier, P. *Phys.Rev.Lett.* **89**, 023005 (2002).

[115] Bali, S., O'Hara, K. M., Gehm, M. E., Granade, S. R., and Thomas, J. E. *Phys.Rev.A* **60**, R29–R32 (1999).

[116] Gensemer, S. D., Sanchez-Villicana, V., Tan, K. Y. N., Grove, T. T., and Gould, P. L. *Phys.Rev.A* **56**, 4055 (1997).

[117] Santos, M. S., Nussenzveig, P., Antunes, A., Cardona, P. S. P., and Bagnato, V. S. *Phys.Rev.A* **60**, 3892 (1999).

[118] Gensemer, S. D., Gould, P. L., Leo, P. J., Tiesinga, E., and Williams, C. J. *Phys.Rev.A* **62**, 030702 (2000).

[119] Gorges, A. R., Bingham, N. S., DeAngelo, M. K., Hamilton, M. S., and Roberts, J. L. *Phys.Rev.A* **78**, 033420 (2008).

[120] Sompet, P., Carpentier, A. V., Fung, Y. H., McGovern, M., and Andersen, M. F. *Phys.Rev.A* **88**, 051401 (2013).

[121] Gallagher, A. and Pritchard, D. E. *Phys.Rev.Lett.* **63**, 957–960 (1989).

[122] Miller, J. D., Cline, R. A., and Heinzen, D. J. *Phys.Rev.Lett.* **71**, 2204–2207 (1993).

[123] Fuhrmanek, A., Lance, A. M., Tuchendler, C., Grangier, P., Sortais, Y. R. P., and Browaeys, A. *New Journal of Physics* **12**, 053028 (2010).

[124] Nelson, K. D., Li, X., and Weiss, D. S. *Nat. Phys.* **3**, 556 (2007).

[125] Sortais, Y. R. P., Marion, H., Tuchendler, C., Lance, A. M., Lamare, M., Fournet, P., Armellin, C., Mercier, R., and Messin, G. *Phys. Rev. A* **75**, 013406 (2007).

[126] McCarron, D. J., King, S. A., and Cornish, S. L. *Meas.Sci.Technol.* **19**, 105601 (2008).

[127] Shirley, J. H. *Optics Letters* **7**, 537–539 (1982).

[128] Abel, R. P., Mohapatra, A. K., Bason, M. G., Pritchard, J. D., Weatherill, K. J., Raitzsch, U., and Adams, C. S. *Applied Physics Letters* **94**, 071107 (2009).

[129] Mack, M., Karlewski, F., Hattermann, H., Höckh, S., Jessen, F., Cano, D., and Fortágh, J. *Phys.Rev.A* **83**, 052515 (2011).

[130] Lorenzen, C.-J. and Niemax, K. *Phys. Scr.* **27**, 300–305 (1983).

[131] Sanguinetti, B., Majeed, H. O., Jones, M. L., and Varcoe, B. T. H. *J.Phys.B: At.Mol.Opt.Phys.* **42**, 165004 (2009).

[132] Pack, M. V., Camacho, R. M., and Howell, J. C. *Phys. Rev. A* **76**, 013801 (2007).

[133] Taichenachev, A. V., Tumaikin, A. M., and Yudin, V. I. *JETP Letters* **72**, 119–122 (2000).

[134] Gallagher, T. F. *Rydberg Atoms*. Cambridge University Press, (1994).

[135] Piotrowicz, M. J., MacCormick, C., Kowalczyk, A., Bergamini, S., Beterov, I. I., and Yakshina, E. A. *New Journal of Physics* **13**, 093012 (2011).

[136] Autler, S. H. and Townes, C. H. *Phys. Rev.* **100**, 703–722 (1955).

[137] Abi-Salloum, T. Y. *Phys. Rev. A* **81**, 053836 (2010).